MAGDALENA RUCKA
KRZYSZTOF WILDE

APPLICATION OF WAVELET ANALYSIS IN DAMAGE DETECTION AND LOCALIZATION

WYDAWNICTWO
POLITECHNIKI GDAŃSKIEJ

MAGDALENA RUCKA
KRZYSZTOF WILDE

APPLICATION OF WAVELET ANALYSIS IN DAMAGE DETECTION AND LOCALIZATION

GDAŃSK 2007

REDAKTOR PUBLIKACJI NAUKOWYCH
Janusz T. Cieśliński

RECENZENCI
Paweł Kłosowski
Zbigniew Zembaty

PROJEKT OKŁADKI
Katarzyna Olszonowicz

Wydano za zgodą
Rektora Politechniki Gdańskiej

Wydawnictwa PG można nabywać w Księgarni PG (Gmach Główny, I piętro)
i zamawiać faksem, pocztą elektroniczną lub listownie pod adresem:
Wydawnictwo Politechniki Gdańskiej
ul. G. Narutowicza 11/12, 80–952 Gdańsk, tel./fax 058 347 16 18
e-mail: wydaw@pg.gda.pl, www.pg.gda.pl/WydawnictwoPG

ISBN 978–83–7348–192–3

CONTENTS

LIST OF SYMBOLS AND ABBREVIATIONS

Symbols

a – depth of a defect
$a_j[k]$ – one-dimensional discrete approximation
$a_j[k,m]$ – two-dimensional discrete approximation
$Af(u,v,s)$ – angle of the wavelet transform vector
$\mathbf{A}(\omega)$ – accelerance
b – bias of neural network
B – width
B_1 – distance from a support to a defect along width
B_r – width of a defect
$\mathbf{B}(\mathrm{s})$ – system matrix
$\mathbf{C}$ – damping matrix
$\bar{\mathbf{C}}$ – modal damping matrix
$d_j[k]$ – one-dimensional discrete wavelet coefficient
$d_j^i\,[k,m]$ – two-dimensional discrete wavelet coefficient
D_1, D_2 – diameters
E – Young’s modulus (chapter 4)
E – error minimized by training algorithm (chapter 5)
f – frequency
f_a – pseudo-frequency of wavelet transform
f_c – centre frequency of a wavelet
$f(t)$ – one-dimensional time signal
$f(x)$ – one-dimensional space signal
$\mathbf{f}(t)$ – force vector
$f(x,y)$ – two-dimensional space signal
F – value of concentrated static load
$F(\omega)$ – Fourier transform of one-dimensional signal
g – high-pass filter
$g_{u,\zeta}(t)$ – window function
G_{FF} – autospectrum of the force
G_{FX} – cross spectrum between the response and the force
G_{XF} – cross spectrum between the force and the response
G_{XX} – autospectrum of the response
h – low-pass filter
H – height
H_1 – distance from a support to a defect along height
H_r – height of a defect
$H(\omega)$ – frequency response function
$H_1(\omega)$, $H_2(\omega)$ – estimators of frequency response function
$\mathbf{H}(\mathrm{s})$ – transfer function matrix
$\mathbf{H}(\omega)$ – frequency response function matrix (receptance)

i – imaginary unit
K – number of neurons in output layer
$\mathbf{K}$ – stiffness matrix
$\overline{\mathbf{K}}$ – modal stiffness matrix
L – length
L_1 – distance from a support to a defect along length
L_2 – distance from the free end of a beam to the load
L_r – length of a defect
$\mathbf{L}^2(\mathrm{R})$ – Hilbert space of measurable, square-integrable one-dimensional functions
$\mathbf{L}^2(\mathrm{R}^2)$ – Hilbert space of measurable, square-integrable two-dimensional functions
m – number of modes
mse – mean sum of squares of the network errors
$msereg$ – mean squared error with regularization performance function
msw – mean of the sum of squares of the network weights and biases
M – number of neurons in hidden layer
$Mf(u,v,s)$ – modulus wavelet transform of two-dimensional signal
$\mathbf{M}$ – mass matrix
$\overline{\mathbf{M}}$ – modal mass matrix
n – number of vanishing moments
n_d – number degree of freedom
net – net function
o – output of neural network
p – pole
P – number of patterns
$P_{\mathrm{V}_j} f$ – orthogonal projection of function $f(x)$ on space $\boldsymbol{V}_\mathrm{j}$
$P_{\mathrm{W}_j} f$ – orthogonal projection of function $f(x)$ on space $\boldsymbol{W}_\mathrm{j}$
$\mathbf{q}(t)$ – modal coordinate vector
R – number of neurons in input layer
$\mathbf{R}(\mathrm{s})$ – residue matrix
R – real numbers
s – scale parameter
s – Laplace variable (section 3.1.2)
$Sf(u,\zeta)$ – windowed Fourier transform of one-dimensional signal
t – time
t_k – scaling factor
t_r – threshold value
T – sampling period
u – translation parameter (position)
u_0 – beam displacement under dead load
u_F – beam displacement under concentrated static load
$\mathbf{u}$ – eigen vector
$\mathbf{U}$ – modal matrix
$\boldsymbol{V}_j$ – approximations space
w – weight of neural network
$Wf(u,s)$ – continuous wavelet transform of one-dimensional signal
$Wf(u,v,s)$ – continuous wavelet transform of two-dimensional signal

$\boldsymbol{W}_j$ – details space
x – space coordinate
$x(t)$ – displacement signal
$\mathbf{x}(t)$ – displacement vector
$X(\omega)$ – Fourier transform of displacement signal
y – space coordinate
z – input of neural network
Z – integers
γ – performance ratio
η – learning rate
$\theta(x)$ – one-dimensional smoothing function
$\theta(x,y)$ – two-dimensional smoothing function
ν – Poisson ratio
ξ – damping ratio
ρ – mass density
σ_t – time interval
σ_ω – frequency interval
$\phi(x)$ – scaling function
$\phi_{j,k}(x)$ – family of discrete scaling function
$\Psi(\omega)$ – Fourier transform of one-dimensional mother wavelet function
$\psi(x)$ – one-dimensional mother wavelet function
$\psi_{j,k}(x)$ – family of discrete wavelets
$\psi_{u,s}(x)$ – family of wavelets
$\psi^1(x,y)$ – two-dimensional horizontal wavelet function
$\psi^2(x,y)$ – two-dimensional vertical wavelet function
$\psi^3(x,y)$ – two-dimensional diagonal wavelet function
ω – circular frequency
ω_d – circular damped frequency
ω_n – circular natural frequency
$\boldsymbol{\Omega}$ – spectral matrix

Abbreviations

ANN – artificial neural network
CMYK – cyan, magenta, yellow, black space of colours
CWT – continuous wavelet transform
DWT – discrete wavelet transform
FEM – finite element method
FRF – frequency response function
FT – Fourier transform
GPS – Global Positioning System
NDT – non-destructive testing
RGB – red, green, blue space of colours
SHM – structural health monitoring
WFT – windowed Fourier transform
WT – wavelet transform

Chapter 1

INTRODUCTION

> *To, że matematycy znajdują szczęście w przestrzeniach Banacha, mogłoby być rzeczą dość zrozumiałą, ale dlaczego przestrzenie te pojawiają się tak często, ilekroć chcemy rozszyfrować strukturę rzeczywistego świata? Czy świat jest zbudowany według recept na szczęście matematyków?*
>
> *The fact that mathematicians find happiness in Banach spaces could be quite understandable, but why these spaces appear every time we want to decipher the structure of the real world? Is the world constructed in accordance to formulas for mathematicians' happiness?*
>
> Michał Heller
> *Szczęście w przestrzeniach Banacha, 1997*
> *Happiness in Banach spaces, 1997*

1.1. Damage detection in civil engineering structures

All structures raised by humans have a limited lifespan. They wear out and undergo self-destruction in the course of time. Fatigue, corrosion, dynamic phenomena, overloading and environmental conditions can cause their degradation. In recent years, structural damage detection and health monitoring have emerged as the subject of intensive investigation due to their practical importance. For structures like offshore platforms, dams, transmission towers, bridges, aircraft, etc. (Fig. 1.1) early detection of damage is essential since propagation of defects might lead to a catastrophic failure. Accurate detection of damage is also necessary in structural strengthening or reconstruction.

A damage detection system can have four levels of the defect identification accuracy proposed by Rytter in 1993 [99]:

- level 1: the presence of damage,
- level 2: the geometric location of damage,
- level 3: the quantification of the severity of damage,
- level 4: the prediction of the remaining service life of the structure.

The most common method of a non-destructive assessment of the structure integrity is a routine visual inspection, mandatory for important structures. For example, bridges have to be regularly checked by experienced engineers. Damage detection can be facilitated by non-destructive testing (NDT) based on radiography [37, 103], acoustic emission [77, 91], ultrasonic testing [128], magnetic fields methods [54, 120], eddy current methods [35], etc. Although such diagnostic methods can be effectively applied to damage detection in a few known *a priori* areas in a structure, however, they are impractical for a search of potential damage through all engineering object. Additionally, the mentioned NDT methods do not allow an on-line inspection but they are done at periodic maintenance check.

The further development in the NDT methods leads to so-called “structural health monitoring” (SHM). The structural health monitoring is a sub-discipline of the structural engineering which is focused on non-destructive techniques related to continuous, automatic and real time *in situ* monitoring of physical parameters to detect any changes in structures or their abnormal states. There are two major types of monitored parameters, i.e. the load effects (wind, earthquake, temperature, traffic movements, etc.) and the structural responses (displacements, accelerations, velocities, stresses, strains, etc.) [110]. A typical SHM system includes three major components: a sensor system (seismometers, anemometers, accelerometers, velocity and displacement gauges, Global Positioning Systems, thermometers, etc.), a data processing system (including data acquisition, transmission and storage) and a health evaluating system (including diagnostic algorithms and information management) [56].

The SHM techniques are applied to the structures of a special importance like wind turbines [32], offshore structures [75], aircraft [1, 34, 71] or bridges [57, 58, 79, 85]. SHM of bridges can be represented by the example of Commodore Barry Bridge in Philadelphia [3]. The continuous real-time monitor system has been functioning since 1998 on this cantilevered trough-truss bridge. The 145-channels system measures ambient temperatures and wind speed in three directions at several locations once a second. The displacement sensors are installed on the piers and at the various locations of the structure for measuring the movement history. The system also monitors live load images and the corresponding strains and acceleration responses. The integrated streams of data are transmitted from the bridge data server through Internet for the remote control of data acquisition, viewing, processing and archive [3].

Fig. 1.1. Engineering structures (photographed by M. Rucka)

The vibration-based methods and the wave propagation methods play a significant role in SHM strategies of damage detection. The wave propagation is an extension of the NDT wave testing from the local to global approach of sending waves. The passing of waves through material thickness is extended to methods based on the wave propagation along the structure [50, 82, 113]. Guided ultrasonic waves or guided acoustic Lamb waves are attractive due to their ability of inspecting large-structures with a small number of transducers [92, 106, 112]. Detection of Lamb waves can be also achieved by the use of the optical fibre sensors [56, 112].

The vibration-based methods make use of the vibration structure characteristics like the modal frequencies, modal damping and modal shapes, e.g. [89, 90, 127]. Damage in a structure alters values of the dynamic parameters. The presence of damage in structures results in reduction of stiffness and increase of damping. The reduction of stiffness causes a decrease in the natural frequencies of vibration and modification of the mode shapes. Therefore, the relatively simple vibration measurements of a structure and the information extraction of the natural frequencies, damping or mode shapes from the data make damage detection possible. The earlier works on damage detection by the measurements of the natural frequencies have been presented by Cawley and Adams [13]. The procedures of crack detection using the frequency measurements are given, for example, in references [45, 55] and [84]. The applicability of the natural frequency-based method is limited since even significant damage may cause very small changes in the natural frequencies, particularly in large structures, e.g. [25, 48]. Detection of defects and their location might be performed on the displacement mode shapes and their derivatives [2, 83, 123]. This method is proved to be effective in the case of vibration data obtained from numerical simulations. However, with the noisy experimental data, the success of the technique is significantly affected [69]. An improved identification method based on modal information has been presented by Kim and Stabbs [46]. An extensive review of previous research on the vibration-based methods is given in [22, 23, 26, 28] and [101].

Structural health monitoring can be supported by the artificial neural networks (ANN) to process the output data. The neural networks can play the major role in the recognition of sets of data that are related to damage or failure phenomena in the structures that are monitored [59]. There are two main reasons to apply ANN: extracting hidden information from noisy data and the possibility of automatic operation in real time.

1.2. Wavelet transform application in damage detection

The application of wavelet transforms to a wide variety of problems is so plentiful that they have emerged as the most promising techniques in the past decade. Wavelets help to analyse the variations of values at financial markets [108, 109]. The biologists use them for cell membrane recognition. The physicians can estimate electrocardiogram (ECG) parameters [104] and detect myocardial ischemic events using wavelets [88]. The Federal Bureau of Investigation (FBI) considers wavelet application for storage of 30 million sets of criminal fingerprints [107]. The computer scientists exploit them in image processing like edge recognition, image searching, animation control, image compression and even internet traffic description [65, 102]. Engineers use wavelet transforms for time phenomena study in transient processes in earthquake, wind, ocean and mechanical engineering [5, 33, 36] or dynamic silo flow [76]. The wavelet transform is also very useful in modal parameters identification [53], especially damping [105].

Recently, wavelets have been tested for structural health monitoring and damage detection [40, 47, 111]. The ability to monitor the structural parameters and detect damage at the earliest possible stage becomes an important issue throughout the aircraft, mechanical [86, 114] and civil engineering communities [68]. A crack in a structure introduces singularities to the mode shapes or the static deflection lines. These small defects cannot be identified directly from the structure response, but may be observed on the wavelet transforms since the local abnormalities in the signal cause variations of the wavelet coefficients in the neighbourhood of damage.

The literature on wavelet transforms in the one-dimensional case is very extensive. The applicability of various wavelets in cracks detection in beams has been studied by Douka *et al.* [24], Loutridis *et al.* [61], Quek *et al.* [87], Hong *et al.* [39], Wang and Deng [115], Chang and Chen [15] as well as Gentile and Messina [31, 69]. The frame structures treated by the one-dimensional signals have been analysed by Ovanesova and Suarez [80]. The previous studies have shown very good accuracy and effectiveness of the wavelet transform although most of the investigations were performed on the numerical data without the experimental verification. Gentile and Messina [31, 69], Chang and Chen [15] as well as Hong *et al.* [39] pointed out the importance of taking into account the effect of noise. In their study the theoretical mode shapes have been contaminated by a Gaussian noise. The wavelet analysis showed that the presence of noise can mask damage, particularly for fine scale values.

For a practical application of the wavelet damage detection techniques, research on experimental data is the most important. The applicability of the wavelet damage detection techniques depend on the measurement precision and the sampling distances. Pai and Young [81] used a scanning laser vibrometer for non-contact measurements of the beams velocities. The obtained noise level was estimated to have very small standard deviation going below 1% of the maximum reference value. Additionally, the device allowed the measurements of up to 400 equally spaced points. Hong *et al.* [39] and Douka *et al.* [24] showed that the effectiveness of the wavelets for damage localization is highly limited by the sampling distances. They used the dynamic mode shapes extracted from the acceleration measurements. One accelerometer was kept as a reference input, while the second one was moved along the beam. They performed the measurements in 39 points of the beam. For the wavelet analysis, the signal was oversampled to 390 points by a cubic spline interpolation. Rucka and Wilde [98] used the photogrammetric displacement measurement technique that allowed the high precision measurements of the beam static displacements in 81 points. Although current works show that only relatively large cracks can be detected, the search for structural damage by the wavelets is a promising and developing field of research. The mode shape measurements performed by Rucka and Wilde [96] in 48 points showed effectiveness of wavelet-based damage localization in beams.

Two-dimensional damage detection problems were addressed by Wang and Deng [115]. They analyzed a steel plate with an elliptical hole and subjected to uniform tensile loading. The static displacement field has been determined by an analytical formula and has been considered as an input for the wavelet transform. The location of the crack tip has been found by variation of the Haar wavelet coefficients. Douka *et al.* [25] studied vibrations of a rectangular plate with a crack running parallel to one side of the plate. The wavelet transform has been successfully applied to the analytically determined eignefunctions. The cracks of a relative depth from 10% to 50% have been considered. The proposed intensity factor allowed estimation of damage size. The works based on the numerically computed plate mode shapes were presented by Chang and Chen [16] and Rucka and Wilde [93]. The wavelet transforms of the two-dimensional plate problems [16, 25, 93] were addressed by the one-dimensional wavelet analysis since the signal lines at different locations have been treated separately.

Experimental research on plate damage detection has been presented by Rucka and Wilde [95, 118]. The experimental mode shapes of the cantilever plate have been determined by acceleration measurement in one point and impact excitation in 66 points. The relative depth of the introduced rectangular defect was about 19%. The location of damage was determined by Gaussian wavelet with 4 vanishing moments. However, the problem was approached by the one-dimensional wavelet formulation. The two-dimensional formulation of the wavelet transform for plate damage detection is presented by Rucka and Wilde in [97].

1.3. Aim and scope of study

The aim of the research is to verify the applicability of the wavelet analysis in damage identification. The effectiveness of the wavelet transform in damage detection is tested on the numerically and experimentally determined static or dynamic responses of a beam, plate and shell. The improvement of the wavelet-based damage detection method is obtained by the use of the artificial neural network systems.

The work consists of the following chapters:

Chapter 1 reviews the structural health monitoring methods and the wavelet transform application in damage detection.

The wavelet theory is introduced in **Chapter 2**. The definitions of the one-dimensional and two-dimensional wavelet transforms are given. The continuous and discrete wavelet transforms are considered. The examples of the real wavelet functions are given and the ability of wavelet transforms to detect the singularities in the response signals is presented.

Chapter 3 deals with the application of the wavelet theory to damage detection. The experimental procedures to estimate the mode shapes and static deflection lines are described. The wavelet selection is carried out and the best candidates for damage detection are presented. The insight of the differential action of the wavelet transform is discussed.

Chapter 4 examines the applicability of the wavelet transforms to damage detection on the experimental and numerical examples. The beam, plate and shell structures are considered. The location of the defects is searched by the analysis of the spatial variation of the transformed responses

In **Chapter 5** the application of the artificial neural networks to damage prediction based on the wavelet coefficients is shown. The backpropagation algorithm for training a supervised feedforward multilayer neural network is used. The neural network system is considered as the method for the improvement of the efficiency of the damage location technique.

Final conclusions, original elements of the study and the recommendations for the future work are presented in **Chapter 6**.

Chapter 2

WAVELET THEORY

2.1. Introduction to wavelet analysis

The aim of a signal processing is gaining as much information from the raw signal as it is possible. Among various response transform methods the most popular is the Fourier transform (FT). In 1808, French mathematician, Joseph Fourier showed that any periodic motion can be represented by a superposition of sinusoidal vibrations [8]. The Fourier transform, in essence, decomposes a function into sinusoids of different frequencies which can sum to the original waveform. This transform provides a frequency representation of the signal i.e., gives information which frequency components exist in the signal. The Fourier transform is an excellent tool for the analysis of the stationary signals in which frequencies components exist all time. However, for the nonstationary signals, where the time localization of spectral components is required, there is a need for transformations giving the time-frequency representation.

In 1946, Dennis Gabor adapted the Fourier transform to analyze only short segments of a signal. These small sections are assumed to be stationary and can be transformed separately using a window function, which is moved along the signal. Gabor's adaptation, called the windowed Fourier transform (WFT), maps a signal into a two-dimensional function of time and frequency. Disadvantage of the WFT is the fact that this transform uses the same window for the analysis of the entire signal. In 1975, researchers Jean Morlet and Alex Grossman for the first time used the term "wavelet". During studies of the windowed Fourier transform they discovered that keeping the window fixed was wrong idea. The wavelet transform (WT) uses a different window function for analyzing different frequency bands. Like the WFT, the wavelet transform can measure the time-frequency variation of spectral components, but it has a different time-frequency resolution.

The Fourier transform can be thought of as a continuous form of the Fourier series and it is defined as (e.g. [8, 63]):

$$F(\omega) = \int_{-\infty}^{+\infty} f(t) e^{-i\omega t} dt, \tag{2.1}$$

where $F(\omega)$ denotes the Fourier coefficients that are the amplitudes of each sinusoidal wave $e^{-i\omega t}$, ω is a circular frequency measured in units of radians per second and t is time. Relation between the circular frequency ω and the frequency f measured in cycles per second is $\omega = 2\pi f$. The Fourier coefficient $F(\omega)$ is obtained by multiplying the time signal $f(t)$ by the complex exponential $e^{-i\omega t}$ at certain frequency ω and integration over time. If the signal contains the frequency component ω, the product has large amplitude. Otherwise, the signal does not contain the frequency component ω and the product yields zero.

The windowed Fourier transform maps time domain signal into the two-dimensional function of time and frequency [43], as shown in Fig. 2.1:

$$Sf(u,\zeta)=\int_{-\infty}^{+\infty} f(t)g^{*}_{u,\zeta}(t)dt=\int_{-\infty}^{+\infty} f(t)g(t-u)e^{-i\zeta t}dt. \tag{2.2}$$

The window $g_{u,\zeta}(t)$ is allowed to be complex-valued, although in many applications it may be real. Hence $g^{*}_{u,\zeta}(t)$ denotes complex conjugated. The signal $f(t)$ is multiplied by the window function $g_{u,\zeta}(t)$ modulated at the frequency $\omega=\zeta$ and then subjected to the Fourier transform. The window is moved along the signal and on each position *u* the procedure is repeated until the end of the signal. The window $g_{u,\zeta}(t)$ is the same for all frequencies, i.e. its time interval σ_t and frequency interval σ_ω are fixed. This means that the WFT gives the same resolution across the time-frequency plane (see Fig. 2.1).

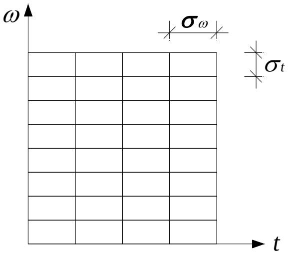

Fig. 2.1. WFT in the time-frequency plane

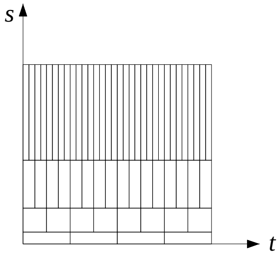

Fig. 2.2. CWT in the time-scale plan

The windowed Fourier transform provides accurate information about the signal simultaneously in the time domain and in the frequency domain. However, all functions, including window functions, obey the Heisenberg uncertainty principle, which states that the sharp localization in time and in frequency are mutually exclusive i.e., it is impossible to find out what spectral component exist at what instances of time. Only the time intervals in which certain band of frequencies exists can be known. The uncertainty principle states that the time spread of a function and its frequency spread cannot be simultaneously small. The uncertainty principle proves that the area of a rectangle having a time width σ_t and a frequency width σ_ω is at least [14, 63]:

$$\sigma_t\sigma_\omega \geq \frac{1}{2}\,. \tag{2.3}$$

Therefore the resolution in the time and frequency of the WFT depends on the size of the window in the time and frequency. There are two conflicting requirements in the time-frequency analysis. On the one hand good time resolution (narrow window) implies poor frequency resolution, on the other hand good frequency resolution (wide window function) gives poor time localization [14].

In the case of nonstationary signals, the ultimate solution is the wavelet transform which provides time-scale representation of the signal. The wavelets are the new way to see and represent a signal. They are alternatives to the Fourier transform rather than its replacement. But in contrast to the Fourier transform which during transformation to the frequency domain loses time information, wavelets have scale aspects and time aspects.

For a given signal $f(t)$, where the variable *t* is time, the continuous wavelet transform (CWT) is obtained by integration of the product of the signal function and the wavelet functions (e.g. [6, 8, 14, 20]):

$$Wf(u,s) = \frac{1}{\sqrt{s}} \int_{-\infty}^{+\infty} f(t)\psi^{*}\left(\frac{t-u}{s}\right)dt, \tag{2.4}$$

where $\psi^{*}(t)$ is the complex conjugate of the wavelet function and *s* denotes the scale parameter. $Wf(u,s)$ is called the wavelet coefficient for the wavelet $\psi_{u,s}(t)$.

The fact that wavelet analysis does not produce a time-frequency view of a signal is not weakness, but strength of the technique. The concept of the scale has similar meaning as a scale used in maps. High scales correspond with a global view whereas low scales correspond to a detailed view. In the wavelet technique, in contrast to the WFT (Fig. 2.1), a time-scale representation of a signal is characterized by variable-sized regions, as shown in Fig. 2.2. Wavelets allow using of short time intervals to obtain precise high frequency information and using longer time intervals for low frequency information. A width and height of the box change but the area is constant. Each box represents equal portion of the time-frequency plane with different proportions to time and frequency. The low scales (high frequencies) correspond to a good time resolution and poor frequency resolution. The high scales (low frequencies) correspond to a good frequency resolution and poor time resolution. The relationship between a scale and frequency cannot be given in a precise sense. It is better to speak about the pseudo-frequency corresponding to a scale computed as follows [72]:

$$f_a = \frac{f_c T}{s}, \tag{2.5}$$

where f_c denotes the centre frequency of a wavelet in Hz and *T* is a sampling period.

The Fourier transform as well as the WFT and the WT are defined over the space $\mathbf{L}^2(\mathrm{R})$ of square-integrable functions with a finite energy, i.e:

$$\int_{-\infty}^{+\infty} |f(t)|^2 \, dt < +\infty. \tag{2.6}$$

By working in the Hilbert space $\mathbf{L}^2(\mathrm{R})$ the access to all the facilities provided by the existence of an inner product is possible. The inner product of functions $f(t) \in \mathbf{L}^2(\mathrm{R})$ and $h(t) \in \mathbf{L}^2(\mathrm{R})$ is described by (e.g. [63, 119]):

$$\langle f,h \rangle = \int_{-\infty}^{+\infty} f(t)h^{*}(t)dt, \tag{2.7}$$

therefore three above mentioned transforms (FT, WFT, CWT) can be also written as inner products in $\mathbf{L}^2(\mathrm{R})$:

$$F(\omega) = \left\langle f, e^{-i\omega t} \right\rangle = \int_{-\infty}^{+\infty} f(t)e^{-i\omega t}dt, \tag{2.8}$$

$$Sf(u,\zeta) = \left\langle f, g_{u,\zeta} \right\rangle = \int_{-\infty}^{+\infty} f(t)g(t-u)e^{-i\zeta t}dt, \tag{2.9}$$

$$Wf(u,s) = \left\langle f, \psi_{u,s} \right\rangle = \frac{1}{\sqrt{s}} \int_{-\infty}^{+\infty} f(t)\psi^{*}\left(\frac{t-u}{s}\right)dt. \tag{2.10}$$

2.2. One-dimensional wavelet transform

2.2.1. Continuous wavelet transform

The wavelet is an oscillatory, real or complex-valued function $\psi(x) \in \mathbf{L}^2(\mathrm{R})$ of zero average value and finite length (compact support):

$$\int_{-\infty}^{+\infty} \psi(x)dx = 0. \tag{2.11}$$

The function $\psi(x)$ is called the mother wavelet and $\mathbf{L}^2(\mathrm{R})$ denotes the Hilbert space of measurable, square-integrable one-dimensional functions. From now on, apart from initial general definition, only real wavelets $\psi(x) \in \mathbf{L}^2(\mathrm{R})$ and space domain *x* will be considered. The real function $\psi(x)$ is said to be a wavelet if and only if its Fourier transform $\Psi(\omega)$ satisfies wavelet admissibility condition [63]:

$$\int_{0}^{+\infty} \frac{|\Psi(\omega)|^2}{\omega} d\omega < +\infty. \tag{2.12}$$

To guarantee that the integral (2.12) is finite, the Fourier transform of the wavelet function at $\omega = 0$ must be zero, i.e. $\Psi(0) = 0,$ which justifies, why wavelet functions must have a zero average value. The function $\psi(x)$ localized in both space and frequency domains is used to create a family of wavelets $\psi_{u,s}(x),$ formulated as:

$$\psi_{u,s}(x) = \frac{1}{\sqrt{s}} \psi\left(\frac{x-u}{s}\right), \tag{2.13}$$

where the real numbers *s* and *u* denote the scale and translation parameters, respectively. The family of wavelet functions is a dilated or stretched version of the mother wavelet $\psi(x)$.

For a given signal $f(x) \in \mathbf{L}^2(\mathrm{R}),$ where the variable *x* denotes space, the continuous wavelet transform (CWT) is the inner product of the signal function with the wavelet functions (e.g. [63, 70, 72, 107]):

$$Wf(u,s) = \left\langle f, \psi_{u,s} \right\rangle = \frac{1}{\sqrt{s}} \int_{-\infty}^{+\infty} f(x)\psi\left(\frac{x-u}{s}\right)dx. \tag{2.14}$$

$Wf(u,s)$ is called a wavelet coefficient for the wavelet $\psi_{u,s}(x)$ and it measures the variation of the signal in the vicinity of *u* which size is proportional to *s*. This correlation between the signal and the wavelet is in the sense of frequency content. If the signal contains a spectral component corresponding to the current value of *s*, the product of the wavelet with the signal gives relatively large values at the location, where this spectral component exists. The normalization factor $1/\sqrt{s}$ assures that the rescaled wavelets have equal energy $\|\psi_{u,s}\| = \|\psi\| = 1$ [107]. The integral form of the wavelet transform, given by Eq. (2.14), can be rewritten as a convolution product:

$$Wf(u,s) = \frac{1}{\sqrt{s}} \int_{-\infty}^{+\infty} f(x)\psi\left(\frac{-(u-x)}{s}\right)dx = \frac{1}{\sqrt{s}} f * \psi\left(\frac{-u}{s}\right) = f * \bar{\psi}_s(u), \tag{2.15}$$

where $\bar{\psi}_s(x)$ is described by the formula:

$$\bar{\psi}_s(x) = \frac{1}{\sqrt{s}}\psi\left(\frac{x}{s}\right). \tag{2.16}$$

The wavelet transform described by Eq. (2.15) implemented in any computer code guarantees shorter time of calculations than one described by Eq. (2.14).

2.2.1.1. Vanishing moments

Wavelets have scale and space aspects. Owing to this the space-scale view of signals, an important property of wavelets is their ability to react to subtle changes, breakdown points or discontinuities contained in a signal. In detection of singularities of signals the vanishing moments play an important role. A wavelet has *n* vanishing moments if the following equation is satisfied:

$$\int_{-\infty}^{+\infty} x^n \psi(x)dx = 0, \quad n = 0,1,2,...,k-1. \tag{2.17}$$

Hence the wavelet having *n* vanishing moments is orthogonal to polynomials up to degree *k*–1.

2.2.1.2. Detection of singularities

Mallat proved that for wavelets having *n* vanishing moments and a fast decay exists the function $\theta(x)$ with a fast decay defined as follows [65]:

$$\psi(x) = \frac{d^n\theta(x)}{dx^n}, \qquad \int_{-\infty}^{+\infty}\theta(x)dx \neq 0. \tag{2.18}$$

For $n = 1$ the function $\theta(x)$ is the integral of the wavelet function $\psi(x)$ over $(-\infty, x)$ for each value of *x*:

$$\theta(x) = \int_{-\infty}^{x}\psi(u)du = \int_{x}^{\infty}\psi(u)du. \tag{2.19}$$

Therefore a wavelet with *n* vanishing moments can be rewritten as the n^{th} order derivative of the function $\theta(x)$. The resulting wavelet transform can be expressed as a multiscale differential operator:

$$\begin{aligned} Wf(u,s) &= \frac{s^n}{\sqrt{s}}\int_{-\infty}^{+\infty} f(x)\frac{d^n}{dx^n}\theta\left(\frac{x-u}{s}\right)dx = \frac{s^n}{\sqrt{s}}\frac{d^n}{dx^n}\int_{-\infty}^{+\infty} f(x)\theta\left(\frac{-(u-x)}{s}\right)dx = \\ &= \frac{s^n}{\sqrt{s}}\frac{d^n}{du^n} f * \theta\left(\frac{-u}{s}\right) = s^n\frac{d^n}{du^n}(f * \bar{\theta}_s)(u), \qquad \bar{\theta}_s(x) = \frac{1}{\sqrt{s}}\theta\left(\frac{-x}{s}\right), \end{aligned} \tag{2.20}$$

where $f * \bar{\theta}$ denotes the convolution of functions. Thus the wavelet transform is the n^{th} derivative of the signal $f(x)$ smoothed by a function $\bar{\theta}_s(x)$ at the scale *s*. If the signal has a singularity at a certain point *u*, that means, it is not differentiable at *u*, then the CWT coefficients will have relatively large values. When the scale is large, the convolution with $\bar{\theta}_s(x)$ removes small signal fluctuation and therefore only detection of the large variation is possible [65]. Singularities are detected by finding the abscissa where the maxima of the wavelet transform modulus $|Wf(u,s)|$ converges at fine scales [63]. If the wavelet has only one vanishing moment, the wavelet modulus maxima are the maxima of the first order derivative of $f(x)$ smoothed by $\bar{\theta}_s(x)$. If the wavelet has two or more vanishing moments, the modulus maxima correspond to higher derivatives.

2.2.2. Discrete wavelet transform

2.2.2.1. Orthogonal wavelet transform

The discrete wavelet transform (DWT) is computed at intermediate scales called voices [63]. A family of discrete wavelets can be obtained from Eq. (2.13) substituting the continuous scale *s* and translation *u* with discrete $s = 2^j$ and $u = k2^j$:

$$\psi_{j,k}(x) = \frac{1}{\sqrt{2^j}}\psi\left(\frac{x-k2^j}{2^j}\right) = \frac{1}{\sqrt{2^j}}\psi\left(2^{-j}x-k\right), \tag{2.21}$$

where *j* and *k* are integers.

The continuous wavelet transform does not produce a discrete orthogonal or biorthogonal bases. In $\mathbf{L}^2(\mathrm{R})$ orthonormal wavelet basis is constructed by dilating and translating a single function ψ in the form:

$$\left\{\psi_{j,k}(x) = \frac{1}{\sqrt{2^j}}\psi\left(2^{-j}x-k\right)\right\}_{(j,k)\in\mathbf{Z}^2\,2}. \tag{2.22}$$

The construction of these bases can be related to multiresolution signal approximations. The approximation of function $f(x)\in\mathbf{L}^2(\mathrm{R})$ at the scale 2^j is defined as an orthogonal projection $P_{\mathrm{V}_j}f$ over an approximation space $\mathbf{V}_j \subset \mathbf{L}^2(\mathrm{R})$. To compute this projection the orthonormal basis of $\mathbf{V}_j$ is necessary [63]. This orthogonal basis is constructed by dilating and translating a scaling function ϕ:

$$\phi_{j,k}(x) = \frac{1}{\sqrt{2^j}}\phi\left(2^{-j}x-k\right). \tag{2.23}$$

An orthonormal basis of an approximation space $\mathbf{V}_j$ is defined as follows:

$$\left\{\phi_{j,k}(x) = \frac{1}{\sqrt{2^j}}\phi\left(2^{-j}x-k\right)\right\}_{(j,k)\in\mathbf{Z}^2\,2}. \tag{2.24}$$

The orthogonal projection of the function $f(x)$ over the space $\mathbf{V}_j$ is obtained with expansion in the scaling orthogonal basis [63]:

$$P_{\mathrm{V}_j}f = \sum_{k=-\infty}^{+\infty}\left\langle f,\phi_{j,k}\right\rangle\phi_{j,k}. \tag{2.25}$$

The inner products function $f(x)$ with scaling family functions $\phi_{j,k}$ provide a discrete approximation $a_j[k]$ at the scale 2^j:

$$a_j[k] = \left\langle f,\phi_{j,k}\right\rangle = \int_{-\infty}^{+\infty} f(x)\frac{1}{\sqrt{2^j}}\phi\left(2^{-j}x-k\right). \tag{2.26}$$

The multiresolution theory developed by Mallat [66] and Meyer [70] imposes, that $\mathbf{V}_j \subset \mathbf{V}_{j-1}$. Let $\mathbf{W}_j$ be the orthogonal complement of $\mathbf{V}_j$ in $\mathbf{V}_{j-1}$:

$$\mathbf{V}_{j-1} = \mathbf{V}_j \oplus \mathbf{W}_j . \tag{2.27}$$

The orthogonal projection of the function $f(x)$ on $\mathbf{V}_{j-1}$ can be decomposed (Fig. 2.3) into the sum of orthogonal projections on $\mathbf{V}_j$ and $\mathbf{W}_j$ [63]:

$$P_{\mathbf{V}_{j-1}} f = P_{\mathbf{V}_j} f + P_{\mathbf{W}_j} f . \tag{2.28}$$

The orthogonal projection of a signal $f(x)$ in a detail space $\mathbf{W}_j$ is obtained with the partial expansion in its wavelet basis:

$$P_{\mathbf{W}_j} f = \sum_{k=-\infty}^{+\infty} \left\langle f, \psi_{j,k} \right\rangle \psi_{j,k} . \tag{2.29}$$

The inner products $d_j[k]$ are the wavelet coefficients calculated at scale 2^j:

$$d_j[k] = \left\langle f, \psi_{j,k} \right\rangle = \int_{-\infty}^{+\infty} f(x) \frac{1}{\sqrt{2^j}} \psi\left(2^{-j} x - k\right). \tag{2.30}$$

Both equations (2.26) and (2.30) can be rewritten as the convolution products:

$$a_j[k] = f * \bar{\phi}_j(2^j k) , \tag{2.31}$$

$$d_j[k] = f * \bar{\psi}_j(2^j k) , \tag{2.32}$$

where $\bar{\phi}_j(x) = \sqrt{2^{-j}} \phi(2^{-j} x)$ and $\bar{\psi}_j(x) = \sqrt{2^{-j}} \psi(2^{-j} x)$.

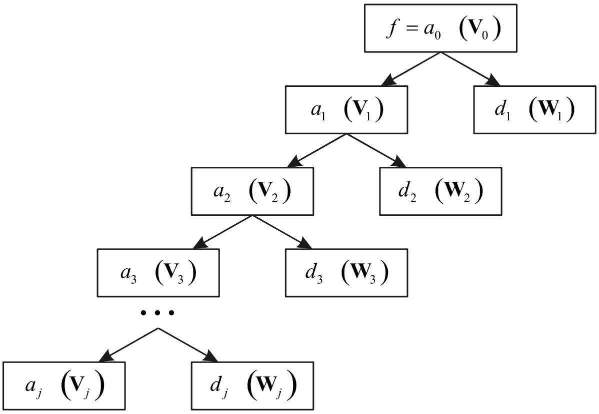

Fig. 2.3. Wavelet decomposition of one-dimensional signal

A signal expansion in a wavelet orthogonal basis can be defined as an aggregation of details at all scales 2^j [63]:

$$f(x) = \sum_{j=-\infty}^{+\infty} P_{\mathbf{W}_j} f = \sum_{j=-\infty}^{+\infty} \sum_{k=-\infty}^{+\infty} \left\langle f, \psi_{j,k} \right\rangle \psi_{j,k}. \tag{2.33}$$

A multiresolution approximation is entirely characterized by the scaling function ϕ that generates an orthogonal basis of each space $\mathbf{V}_j$. It is proved that any scaling and wavelet functions are specified by a discrete conjugated mirror filter [63]:

$$\begin{aligned} \phi(x) &= \sqrt{2} \sum_{k \in \mathbf{Z}} h_k \phi(2x-k), \\ \psi(x) &= \sqrt{2} \sum_{k \in \mathbf{Z}} g_k \phi(2x-k). \end{aligned} \tag{2.34}$$

The low-pass filter h determines the scaling function, whereas the high-pass filter g produces the wavelet function. Equations (2.34) are the links between the wavelets and filters. They were developed separately, but now they work together [107].

The discrete wavelet transform decomposes signal into low-pass and high-pass components downsampled by 2. The inversed transform provides reconstruction. Decomposition and reconstruction of the one-dimensional signal using orthogonal filter banks are given in Fig. 2.4. Decomposition and reconstruction are performed using the same filters h and g ($\bar{h}_k = h_{-k}$, $\bar{g}_k = g_{-k}$). It is known that symmetry and exact reconstruction is incompatible if the same filters are used for reconstruction and decomposition [20].

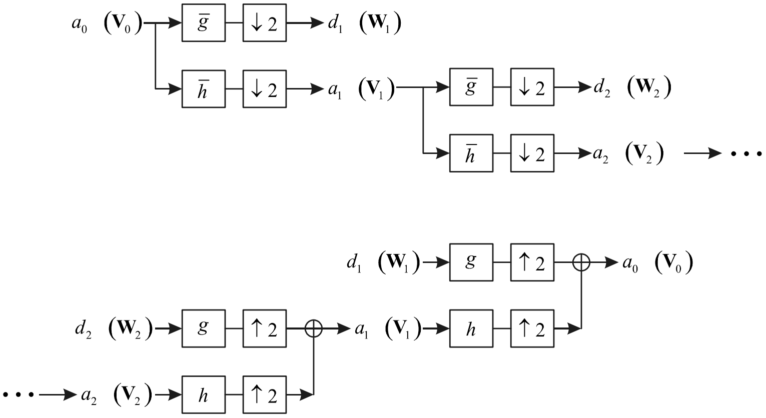

Fig. 2.4. Decomposition and reconstruction of one-dimensional signal by orthogonal filter banks

2.2.2.2. Biorthogonal wavelet transform

The simultaneous symmetry and perfect reconstruction theory was supplemented with the biorthogonal wavelets [49, 60]. The biorthogonal wavelets are constructed using different filters for decomposition (h and g), and different filters for reconstruction ($\tilde{h}$ and $\tilde{g}$). The different filters for decomposition and reconstruction cause that the resulting basis is non-orthogonal [63]. The biorthogonal wavelets require dual bases. The scaling function families $\{\phi_{j,k}\}_{(j,k)\in\mathbf{Z}^2 2}$ and $\{\tilde{\phi}_{j,k}\}_{(j,k)\in\mathbf{Z}^2}$ are biorthogonal Riesz bases for $\mathbf{V}_j$ and $\tilde{\mathbf{V}}_j$, whereas the wavelets $\{\psi_{j,k}\}_{(j,k)\in\mathbf{Z}^2 2}$ and $\{\tilde{\psi}_{j,k}\}_{(j,k)\in\mathbf{Z}^2 2}$ are the biortogonal Riesz bases for $\mathbf{W}_j$ and $\tilde{\mathbf{W}}_j$. Two scaling functions and two wavelets functions are defined by:

$$\begin{aligned} \phi(x) &= \sqrt{2}\sum_{k\in\mathbf{Z}} h_k\phi(2x-k), & \tilde{\phi}(x) &= \sqrt{2}\sum_{k\in\mathbf{Z}} \tilde{h}_k\tilde{\phi}(2x-k), \\ \psi(x) &= \sqrt{2}\sum_{k\in\mathbf{Z}} g_k\phi(2x-k), & \tilde{\psi}(x) &= \sqrt{2}\sum_{k\in\mathbf{Z}} \tilde{g}_k\tilde{\phi}(2x-k). \end{aligned} \tag{2.35}$$

The biorthogonal multiresolution has two sequences $\mathbf{V}_j$ and $\tilde{\mathbf{V}}_j$ with $\mathbf{V}_{j+1} = \mathbf{V}_j + \mathbf{W}_j$ and $\tilde{\mathbf{V}}_{j+1} = \tilde{\mathbf{V}}_j + \tilde{\mathbf{W}}_j$. The biorthogonality denotes that $\mathbf{V}_j \perp \tilde{\mathbf{W}}_j$ and $\tilde{\mathbf{V}}_j \perp \mathbf{W}_j$. A signal expansion in a wavelet biorthogonal basis is defined as:

$$f(x) = \sum_{j=-\infty}^{+\infty}\sum_{k=-\infty}^{+\infty}\left\langle f,\psi_{j,k}\right\rangle\tilde{\psi}_{j,k} = \sum_{j=-\infty}^{+\infty}\sum_{k=-\infty}^{+\infty}\left\langle f,\tilde{\psi}_{j,k}\right\rangle\psi_{j,k}\ . \tag{2.36}$$

Decomposition and reconstruction of a one-dimensional signal using the biorthogonal filter banks are illustrated in Fig. 2.5.

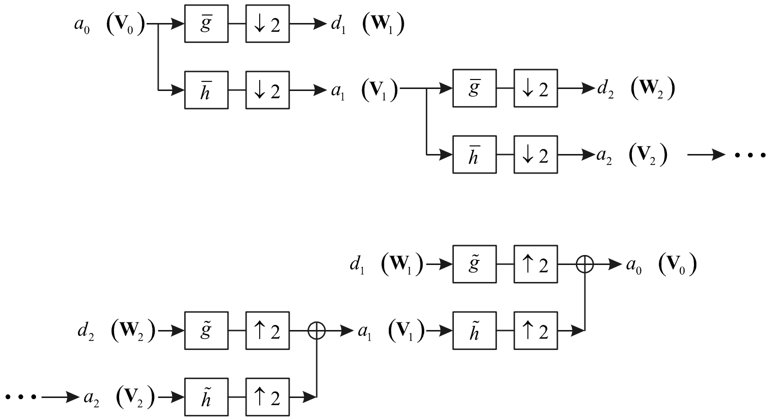

Fig. 2.5. Decomposition and reconstruction of one-dimensional signal by biorthogonal filter banks

2.2.3. Examples of wavelets

There are many wavelet functions and new ones are still being developed. Generally speaking, everybody can create his own wavelet. From the historical point of view, the first one was the Haar wavelet (Fig. 2.6a) known since 1910 [20]. It is a simplest wavelet, however it is discontinuous, and therefore, it cannot be used for damage detection. It has an explicit form given by:

$$\psi(x) = \begin{cases} 1 & 0 \le x < 0.5 \\ -1 & 0.5 \le x < 1\ . \\ 0 & \text{otherwise} \end{cases} \tag{2.37}$$

Other real wavelets given in explicit forms are for instance the Morlet, Gaussian, Mexican hat and Meyer wavelets.

The family of Gaussian wavelet (Fig. 2.8) is built starting from the Gaussian function $g(x) = C_a e^{-x^2}$, by taking its a^{th} derivative of $g(x)$. The integer value a is a parameter of this family and C_a is a constant such that $\| g^{(p)} \|^2 = 1$, where $g^{(p)}$ is the a^{th} derivative of $g(x)$ [72]. The first four wavelets from the Gaussian family have the following form [31]:

$$\begin{array}{ll} \text{gaus1} & \psi(x) = (-1)^1 2\sqrt[4]{2/\pi}\, x e^{-x^2}, \\ \text{gaus2} & \psi(x) = (-1)^2 \dfrac{2\sqrt[4]{2/\pi}}{\sqrt{3}}(1-2x^2)e^{-x^2}, \\ \text{gaus3} & \psi(x) = (-1)^3 \dfrac{-4\sqrt[4]{2/\pi}}{\sqrt{15}}(3x-2x^3)e^{-x^2}, \\ \text{gaus4} & \psi(x) = (-1)^4 \dfrac{4\sqrt[4]{2/\pi}}{\sqrt{105}}(3-2x^2+4x^4)e^{-x^2}. \end{array} \tag{2.38}$$

The Mexican hat (Fig. 2.6b) is the wavelet equal to the second derivative of the Gaussian function $e^{-x^2/2}$. If it is normalized so that its $\mathbf{L}^2$-norm is equal to 1 and $\psi(0) > 0$, the following form can be obtained [20]:

$$\psi(x) = \frac{2}{\pi^{1/4}\sqrt{3}}\left(1-x^2\right)\exp\left(-\frac{x^2}{2}\right). \tag{2.39}$$

The Morlet wavelet (Fig. 2.6c) is defined as:

$$\psi(x) = e^{-x^2/2}\cos(5x). \tag{2.40}$$

It is the one that does not satisfy exactly the admissibility condition (2.12) [72].

The Meyer wavelet (Fig. 2.6d) is defined in the frequency domain [72]:

$$\Psi(\omega) = \begin{cases} (2\pi)^{-1/2} e^{i\omega/2} \sin\left(\dfrac{\pi}{2}\upsilon\left(\dfrac{3}{2\pi}|\omega| - 1\right)\right) & \text{if } \dfrac{2\pi}{3} \le |\omega| \le \dfrac{4\pi}{3} \\ (2\pi)^{-1/2} e^{i\omega/2} \cos\left(\dfrac{\pi}{2}\upsilon\left(\dfrac{3}{4\pi}|\omega| - 1\right)\right) & \text{if } \dfrac{4\pi}{3} \le |\omega| \le \dfrac{8\pi}{3} \\ 0 & \text{otherwise} \end{cases} \tag{2.41}$$

where $\upsilon(a) = a^4(35 - 84a + 70a^2 - 20a^3),\ a \in \langle 0,1 \rangle$.

Not all wavelets are written in the explicit form. There is a group of wavelets that have the implicit form. The Daubechies wavelets (Fig. 2.10), Coiflets (Fig. 2.7), Symlets (Fig. 2.12) are the orthogonal wavelets that come from the orthogonal conjugated mirror filters. The disadvantage of these wavelets is poor regularity and poor symmetry, which is important in damage detection. The biorthogonal filters produce the Biorthogonal (Fig. 2.9) and Reverse Biorthogonal (Fig. 2.11) wavelets. The real wavelets characteristics are given in Table 2.1.

Table 2.1

Real wavelets characteristics

Wavelet family name	Orthogonal	Biorthogonal	Order N Order $N_r.N_d$	No. of vanishing moments	Symmetry	Support width	CWT	DWT
Haar	yes	yes	–	1	yes	1	yes	yes
Daubechies N	yes	yes	$N = 1,2,\ldots$	N	far from	$2N - 1$	yes	yes
Symlet N	yes	yes	$N = 2,3,\ldots$	N	near from	$2N - 1$	yes	yes
Coiflet N	yes	yes	N=1,2,3,4,5	2 N	near from	$6N - 1$	yes	yes
Biorthogonal $N_r.N_d$	no	yes	$N_r = 1$, $N_d = 1,3,5$ $N_r = 2$, $N_d = 2,4,6,8$ $N_r = 3$, $N_d = 1,3,5,7,9$ $N_r = 4$, $N_d = 4$ $N_r = 5$, $N_d = 5$ $N_r = 6$, $N_d = 8$	$N_r - 1$	yes ($N_r = 1,3$) asymmetry ($N_r = 2,4,5,6$)	$2N_d + 1$	yes	yes
Reverse Biorthogonal $N_d.N_r$	no	yes	$N_d = 1$, $N_r = 1,3,5$ $N_d = 2$, $N_r = 2,4,6,8$ $N_d = 3$, $N_r = 1,3,5,7,9$ $N_d = 4$, $N_r = 4$ $N_d = 5$, $N_r = 5$ $N_d = 6$, $N_r = 8$	$N_d - 1$	yes ($N_d = 1,3$) asymmetry ($N_d = 2,4,5,6$)	$2N_r + 1$	yes	yes
Gaussian N	no	no	$N = 1,2,\ldots$	N	yes (N even) asymmetry (N odd)	10	yes	no
Meyer	yes	yes	–	–	yes	16	yes	yes
Mexican hat	no	no	–	2	yes	16	yes	no
Morlet	no	no	–	–	yes	16	yes	no

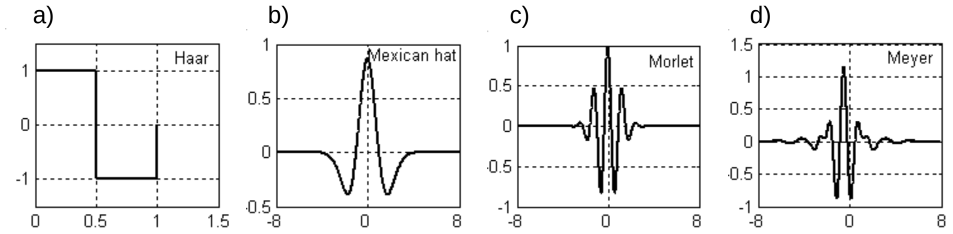

Fig. 2.6. Types of wavelet functions: (a) Haar; (b) Mexican hat; (c) Morlet; (d) Meyer

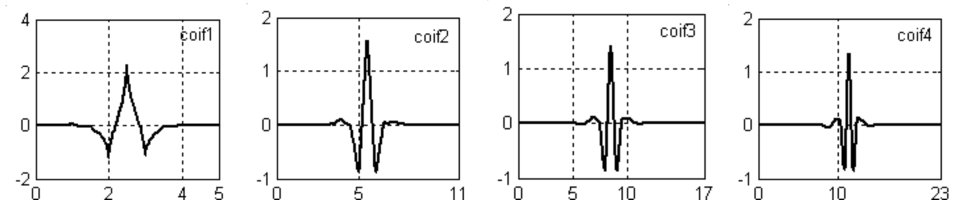

Fig. 2.7. Coiflet family of wavelet functions

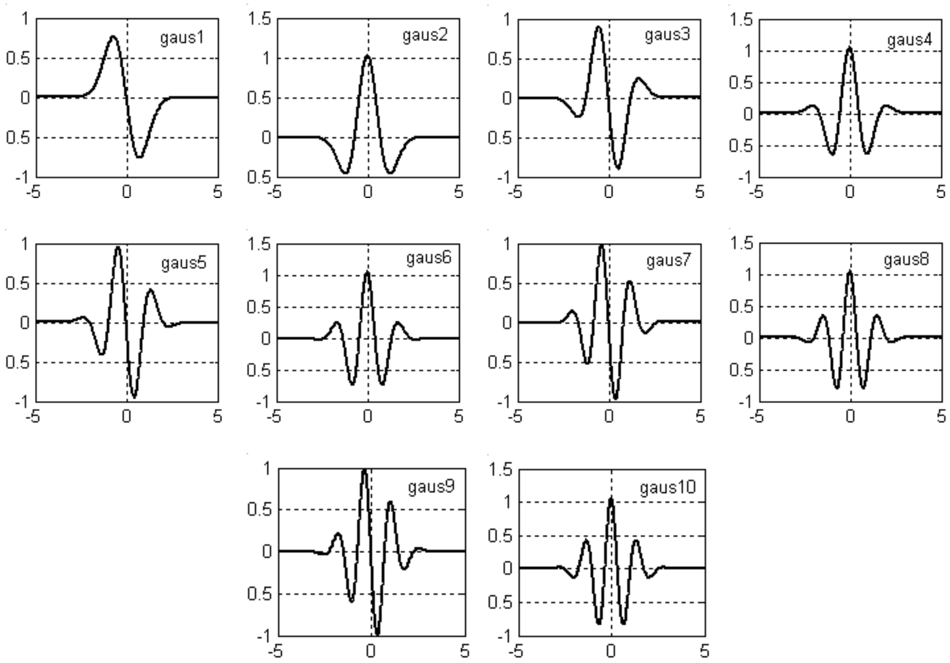

Fig. 2.8. Gaussian family of wavelets functions

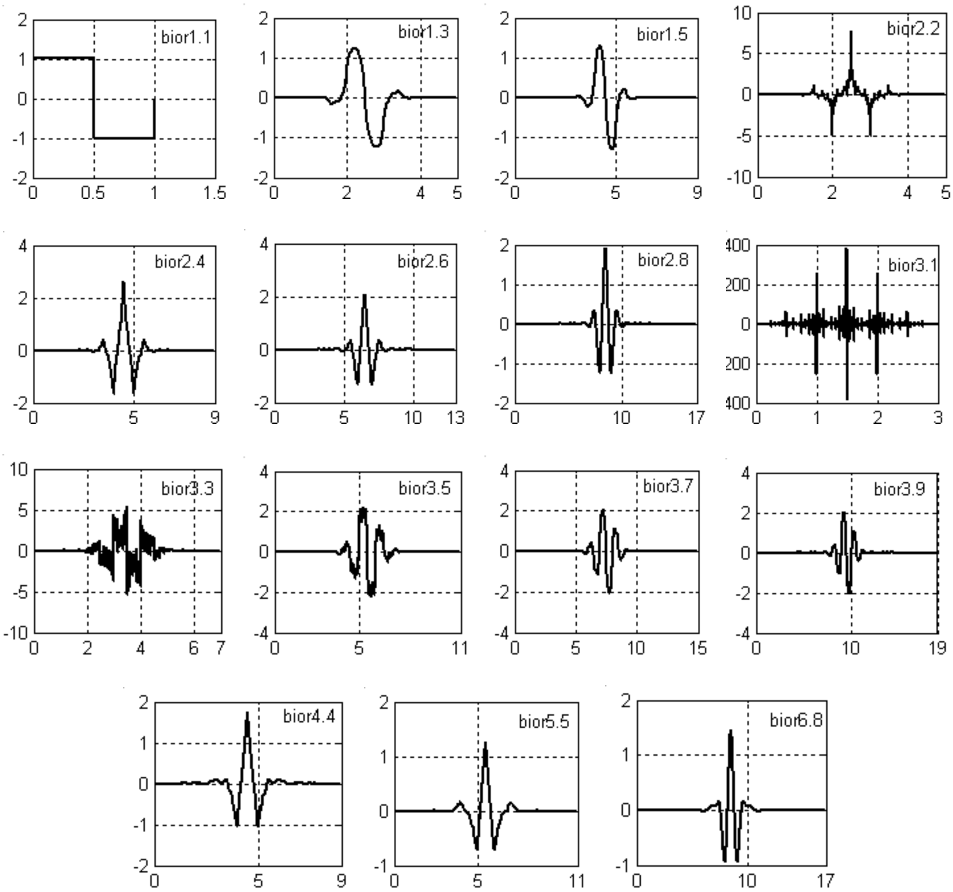

Fig. 2.9. Biorthogonal family of wavelets functions

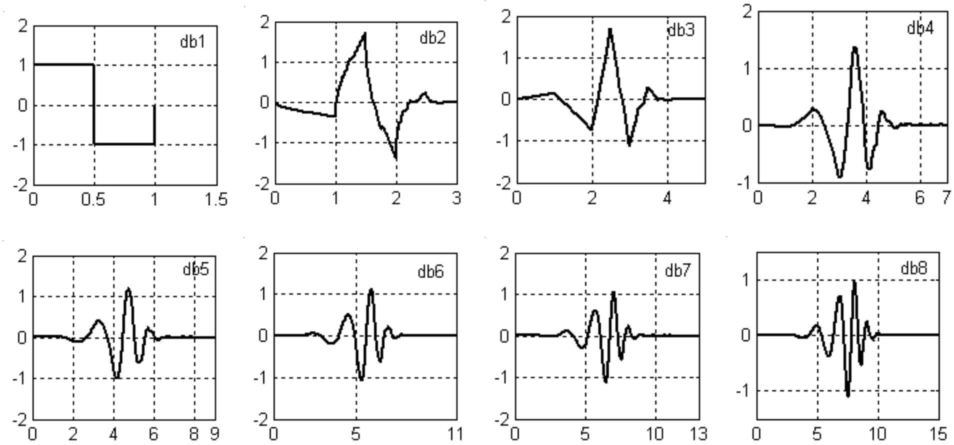

Fig. 2.10. Daubechies family of wavelets functions

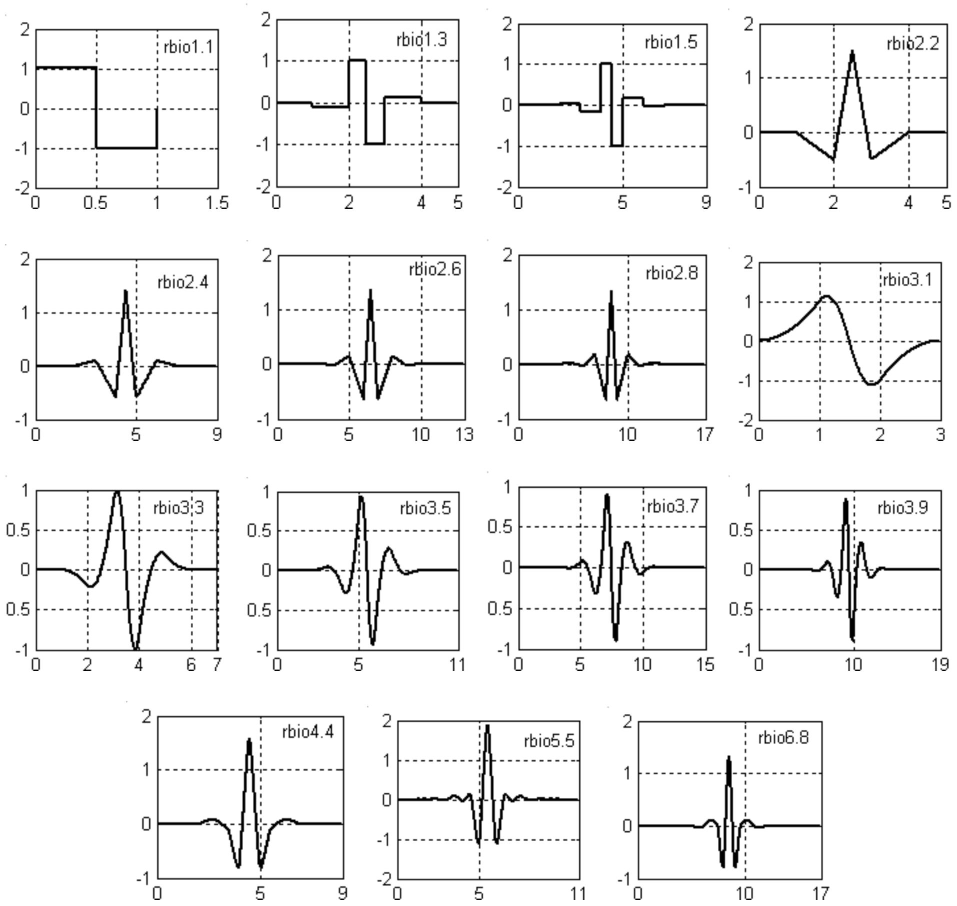

Fig. 2.11. Biorthogonal family of wavelets functions

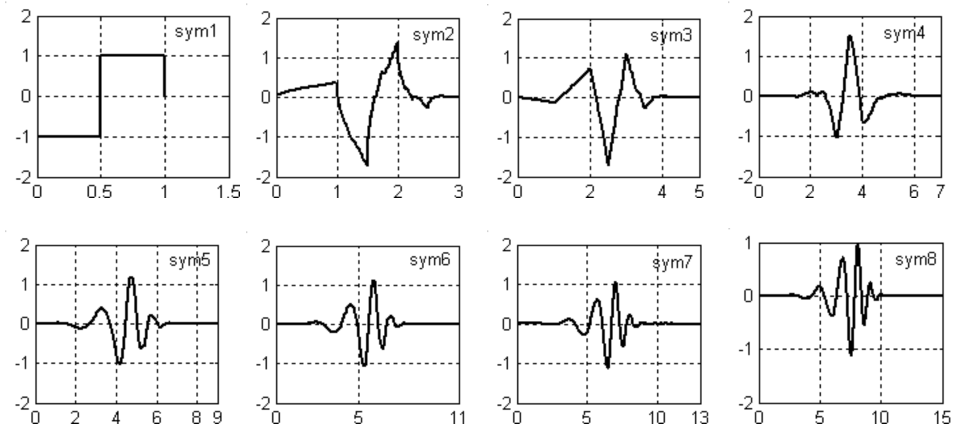

Fig. 2.12. Symlet family of wavelets functions

2.3. Two-dimensional wavelet transform

2.3.1. Continuous wavelet transform

The one-dimensional wavelet transform can be extended to arbitrary dimensions [66]. In this section the two-dimensional wavelet transform is studied. Let the function $f(x,y)$ be a signal belonging to the Hilbert $\mathbf{L}^2(\mathrm{R}^2)$ space of measurable, square-integrable two-dimensional functions. The horizontal wavelet $\psi^1(x,y)$ and the vertical one $\psi^2(x,y)$ are constructed with the separable products of a one-dimensional scaling function ϕ and a one-dimensional wavelet function ψ [63]:

$$\psi^1(x,y)=\phi(x)\psi(y), \qquad \psi^2(x,y)=\psi(x)\phi(y). \tag{2.42}$$

For two directions a family of wavelets can be written as:

$$\psi^i_{u,v,s}=\frac{1}{s}\psi^i\left(\frac{x-u}{s},\frac{y-v}{s}\right), \qquad i=1,2. \tag{2.43}$$

The wavelet transforms of the function $f(x,y)$ defined with respect to each of wavelets given by Eq. (2.42), are formulated as follows:

$$\begin{aligned} W^i f(u,v,s)=\left\langle f,\psi^i_{u,v,s}\right\rangle &=\frac{1}{s}\int_{-\infty}^{\infty}\int_{-\infty}^{\infty} f(x,y)\psi^i\left(\frac{x-u}{s},\frac{y-v}{s}\right)dxdy= \\ &=\frac{1}{s}f*\psi^i\left(\frac{-u}{s},\frac{-v}{s}\right)=f*\overline{\psi}^i_s(u,v) \qquad i=1,2. \end{aligned} \tag{2.44}$$

Two wavelets $\psi^1(x,y)$ and $\psi^2(x,y)$ can be defined as the partial derivatives of the smoothing function $\theta(x,y)$ with respect to *x* and *y* coordinates:

$$\psi^1(x,y)=\frac{\partial^n\theta(x,y)}{\partial x^n}, \qquad \psi^2(x,y)=\frac{\partial^n\theta(x,y)}{\partial y^n}, \tag{2.45}$$

where indexes 1 and 2 denote horizontal and vertical directions, respectively, and *n* is the number of vanishing moments. Two scaled wavelets can be rewritten in the form:

$$\begin{aligned} \psi^1_s(x,y)&=\frac{\partial^n\theta_s(x,y)}{\partial x}=s^n\,\frac{\partial\theta(x,y)}{\partial x}, \\ \psi^2_s(x,y)&=\frac{\partial^n\theta_s(x,y)}{\partial y}=s^n\,\frac{\partial\theta(x,y)}{\partial y}. \end{aligned} \tag{2.46}$$

The scaled smoothing function $\theta(x,y)$ is given by:

$$\theta_{u,v,s}(x,y)=\frac{1}{s}\theta\left(\frac{x-u}{s},\frac{y-v}{s}\right). \tag{2.47}$$

Finally, the derivative form of the wavelet transform can be expressed as:

$$\begin{aligned}\begin{pmatrix} W^1 f(u,v,s) \\ W^2 f(u,v,s)\end{pmatrix} &= \begin{pmatrix} f * \overline{\psi}_s^1(u,v) \\ f * \overline{\psi}_s^2(u,v)\end{pmatrix} = \begin{pmatrix} f * s^n \dfrac{\partial \overline{\theta}_s}{\partial u}(u,v) \\ f * s^n \dfrac{\partial \overline{\theta}_s}{\partial v}(u,v)\end{pmatrix} = \\ &= s^n \begin{pmatrix} \dfrac{\partial}{\partial u}(f * \overline{\theta}_s)(u,v) \\ \dfrac{\partial}{\partial v}(f * \overline{\theta}_s)(u,v)\end{pmatrix} = s^n \vec{\nabla}(f * \overline{\theta}_s)(u,v),\end{aligned} \tag{2.48}$$

where $\overline{\theta}_{u,v,s} = \theta_{u,v,s}(-x,-y)$. Therefore, the wavelet transform components of the derivative form given by Eq. (2.48) can be interpreted as the coordinates of a gradient vector of $f(x,y)$ smoothed by $\overline{\theta}_s(x,y)$. The wavelet component $W^1 f(u,v,s)$ indicates horizontal edges, while the component $W^2 f(u,v,s)$ indicates vertical edges. The names of these components are derived from image processing.

The function

$$Mf(u,v,s) = \sqrt{\left|W^1 f(u,v,s)\right|^2 + \left|W^2 f(u,v,s)\right|^2} \tag{2.49}$$

is called the modulus of the wavelet transform at the scale s, and it is proportional to the modulus of the gradient vector $\vec{\nabla}(f * \overline{\theta}_s)(x,y)$. The modulus $Mf(u,v,s)$ has local maxima in the direction of the gradient given by $Af(u,v,s)$:

$$Af(u,v,s) = \tan^{-1}\left(\frac{W^2 f(u,v,s)}{W^1 f(u,v,s)}\right). \tag{2.50}$$

The angle between the gradient vector $\vec{\nabla}(f * \overline{\theta}_s)(x,y)$ and the horizontal direction indicates locally the direction in which the signal has the sharpest variation [64]. The direction of the gradient vector at a point (x_0, y_0) indicates the direction in the plane (x,y) along which the directional derivative of $f(x,y)$ has the largest absolute value.

2.3.2. Discrete wavelet transform

2.3.2.1. Orthogonal wavelet transform

A one-dimensional scaling function ϕ and a one-dimensional wavelet function ψ are used to generate three wavelets, horizontal $\psi^1(x,y)$, vertical $\psi^2(x,y)$ and diagonal $\psi^3(x,y)$:

$$\begin{aligned}\psi^1(x,y) &= \phi(x)\psi(y), \\ \psi^2(x,y) &= \psi(x)\phi(y), \\ \psi^3(x,y) &= \psi(x)\psi(y).\end{aligned} \tag{2.51}$$

For these three directions the family of wavelets is computed as follows:

$$\psi^i_{j,k,m} = \frac{1}{2^j}\psi^i\left(\frac{x-2^j k}{2^j}, \frac{y-2^j m}{2^j}\right), \qquad i = 1,2,3. \tag{2.52}$$

The wavelet family:

$$\left\{\psi^1_{j,k,m}(x,y),\psi^2_{j,k,m}(x,y),\psi^3_{j,k,m}(x,y)\right\}_{(k,m)\in\mathbf{Z}^2\,\mathbf{2}} \tag{2.53}$$

is an orthogonal basis of space $\mathbf{W}_j^2$ and

$$\left\{\psi^1_{j,k,m}(x,y),\psi^2_{j,k,m}(x,y),\psi^3_{j,k,m}(x,y)\right\}_{(j,k,m)\in\mathbf{Z}^3\,\mathbf{2}} \tag{2.54}$$

is an orthogonal basis of space $\mathbf{L}^2(\mathrm{R}^2)$ [63]. The three wavelets extract three details and approximation on each level j:

$$a_j[k,m]=\left\langle f,\phi_{j,k,m}\right\rangle,\quad d_j^i[k,m]=\left\langle f,\psi^i_{j,k,m}\right\rangle,\quad i=1,2,3. \tag{2.55}$$

Decomposition and reconstruction of a two-dimensional signal by orthogonal filter banks are given in Fig. 2.13.

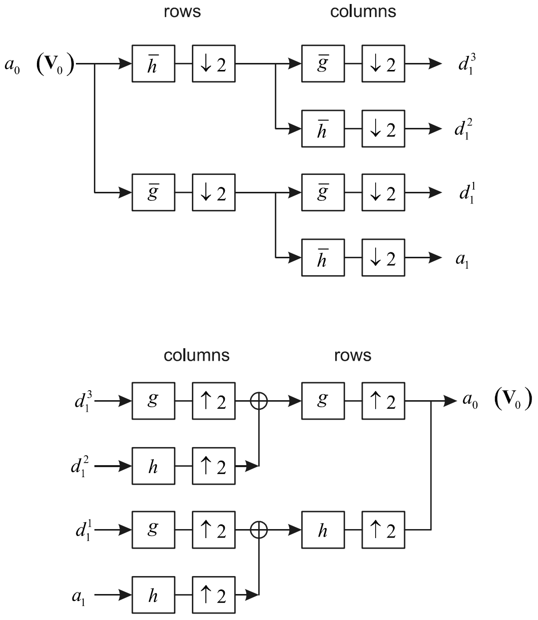

Fig. 2.13. Decomposition and reconstruction of two-dimensional signal by orthogonal filter banks

2.3.2.2. Biorthogonal wavelet transform

The one-dimensional biorthogonal wavelets bases can be extended to the biorthogonal bases of $\mathbf{L}^2(\mathrm{R}^2)$. The dual wavelets to horizontal $\psi^1(x,y)$, vertical $\psi^2(x,y)$ and diagonal $\psi^3(x,y)$ wavelets are:

$$\begin{aligned}\tilde{\psi}^1(x,y)&=\tilde{\phi}(x)\tilde{\psi}(y),\\ \tilde{\psi}^2(x,y)&=\tilde{\psi}(x)\tilde{\phi}(y),\\ \tilde{\psi}^3(x,y)&=\tilde{\psi}(x)\tilde{\psi}(y).\end{aligned} \tag{2.56}$$

The wavelet families:

$$\left\{\psi^1_{j,k,m}(x,y),\psi^2_{j,k,m}(x,y),\psi^3_{j,k,m}(x,y)\right\}_{(j,k,m)\in\mathbf{Z}^3\,\mathbf{2}} \tag{2.57}$$

and

$$\left\{\tilde{\psi}^1_{j,k,m}(x,y),\tilde{\psi}^2_{j,k,m}(x,y),\tilde{\psi}^3_{j,k,m}(x,y)\right\}_{(j,k,m)\in\mathbf{Z}^3\,\mathbf{2}} \tag{2.58}$$

are the biorthogonal Riesz bases of $\mathbf{L}^2(\mathrm{R}^2)$.

The decomposition and reconstruction using the biorthogonal wavelets are performed in the same way like for the orthonormal wavelets with the difference using dual filters $\tilde{h}$ and $\tilde{g}$ instead of g and h.

2.3.3. Examples of wavelets

A construction of two-dimensional wavelets requires existence of a scaling filter $\phi(x)$. The Morlet, Mexican hat and Gaussian wavelets have no scaling function, so they cannot be used in the two-dimensional analysis. In Fig. 2.14 selected wavelet functions and scaling functions are presented. The two-dimensional wavelet and scaling functions for Haar, Coiflet, Symlet and Reverse Biorthogonal families are given in Fig. 2.15, Fig. 2.16, Fig. 2.17 and Fig. 2.18, respectively.

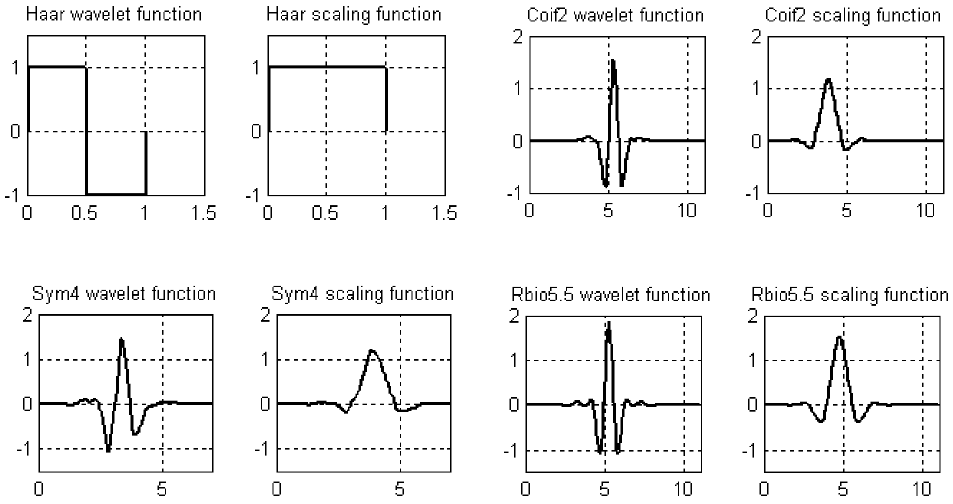

Fig. 2.14. Wavelet and scaling functions for Haar, Coiflet, Symlet and Reverse Biorthogonal families

2.4. Summary

In this chapter, the fundamentals of the continuous and discrete wavelet transform have been presented. The derivation of the continuous wavelet transform has been conducted. The one dimensional transform has been extended into a two dimensions. The significance of vanishing moments in singularities detection has been addressed.

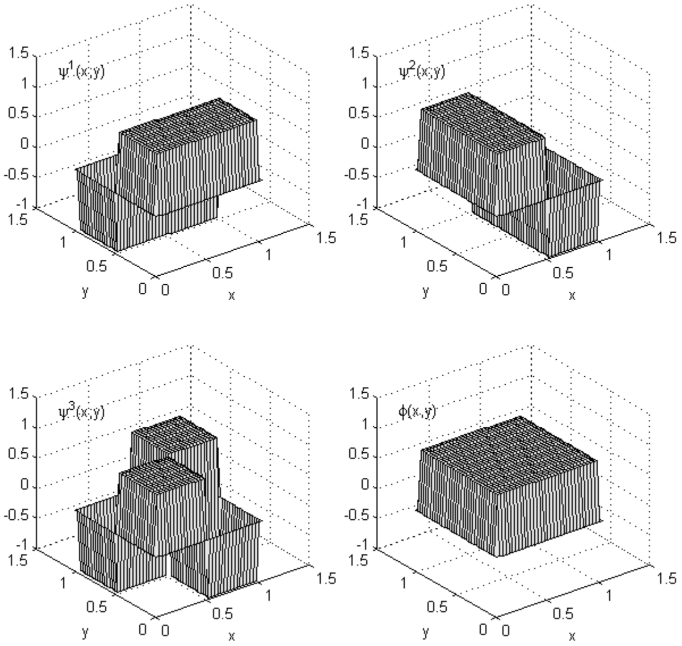

Fig. 2.15. Wavelet functions $\psi^1(x,y)$, $\psi^2(x,y)$, $\psi^3(x,y)$ and scaling function $\phi(x,y)$ for Haar

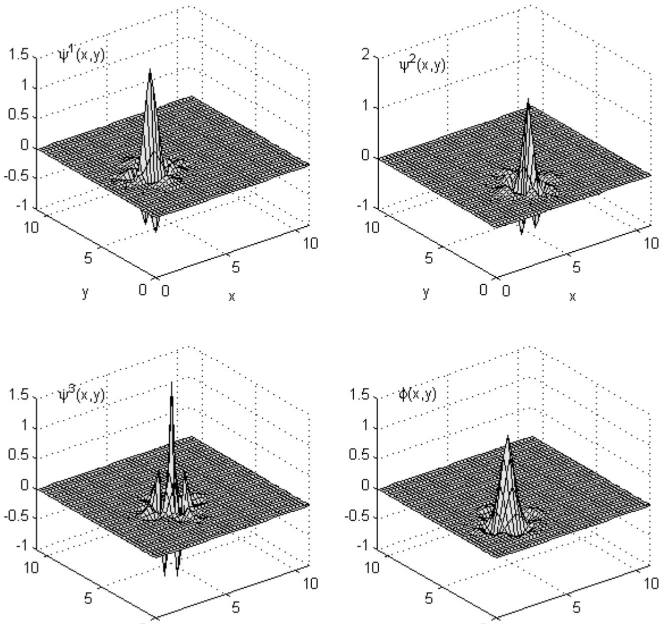

Fig. 2.16. Wavelet functions $\psi^1(x,y)$, $\psi^2(x,y)$, $\psi^3(x,y)$ and scaling function $\phi(x,y)$ for coif2

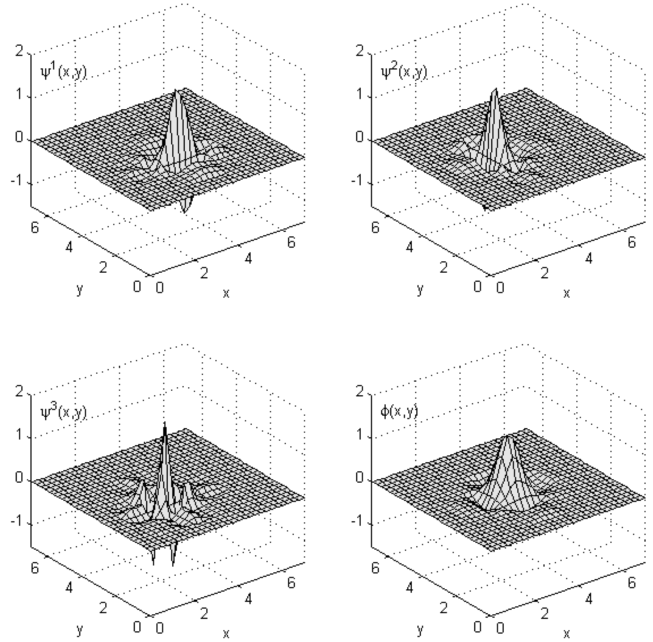

Fig. 2.17. Wavelet functions $\psi^1(x,y)$, $\psi^2(x,y)$, $\psi^3(x,y)$ and scaling function $\phi(x,y)$ for sym4

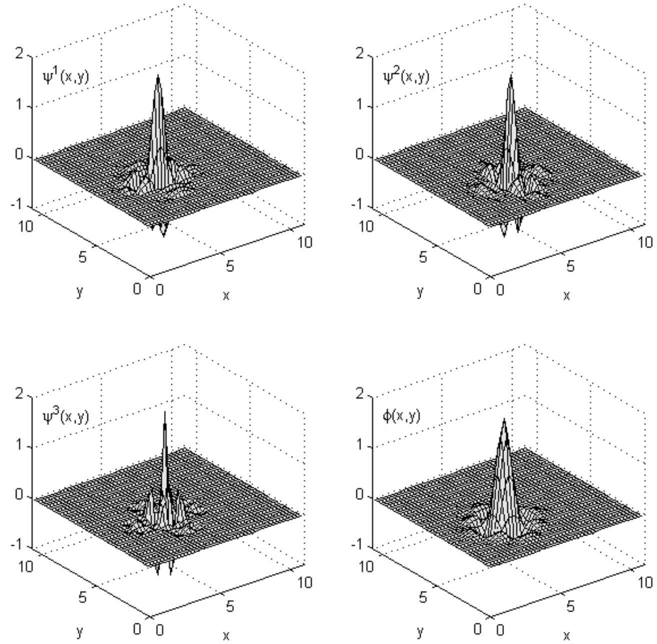

Fig. 2.18. Wavelet functions $\psi^1(x,y)$, $\psi^2(x,y)$, $\psi^3(x,y)$ and scaling function $\phi(x,y)$ for rbio5.5

Chapter 3

WAVELET ANALYSIS IN DAMAGE DETECTION

3.1. Input signals

Measured or calculated static or dynamic structure responses can be treated as a spatially distributed input signals and the continuous wavelet transform can be computed. A sudden change or a peak in the analyzed the wavelet coefficient can indicate the location of a defect.

The traditional methods of the static displacement measurements are the geodetic methods and application of the linear variable differential transducers (LVDT). These methods require a direct access to structures which is not always possible. Additionally, the geodetic methods do not guarantee sufficient accuracy of the measurements in the case of large structures [7]. Thus traditional methods are extended by new, precise and non-contact techniques, for example GPS (Global Positioning System) or laser techniques. GPS is successfully used for continuous monitoring of long-term bridge deformations [117]. Both, laser and GPS techniques can be also used in the dynamic displacement measurements. The scanning laser vibrometer provides the velocity readings at many points to determine the operational deflection shapes [74, 81]. The mode shapes can be measured in the dynamic tests (impulse, sweep or ambient vibration tests). The impulse testing or sweep testing are two methods that are commonly used for the experimental determination the dynamic structures properties. In the sine sweep testing the vibration generators are used to provide a source of a harmonic excitation force [18]. Usually, a vibration generator remains at the same position whereas an accelerometer or set of accelerometers is roving from one point to another. The impulse testing is based on structure excitation by striking it with a modal hammer [67], which generates a short time duration force. This method is often used in the experimental modal analysis. The excitation source can be easy moved from one point to another whereas the output accelerometer remains at the same point. Ambient vibration tests depend on using natural excitations such as traffic or wind [10, 11].

In this study one-dimensional or two-dimensional signals are considered. The static and dynamic beam responses and the mode shapes of the shell measured along center line provide one-dimensional input signals whereas the mode shape of the plate provides two-dimensional signal. To apply wavelet-based damage detection methods a response of a structure in large number of spatially distributed points is necessary. In this research, a non-contact photogrammetric measurement method to determine the static deflection is proposed. The presented photogrammetric technique allows simultaneous measurements of the static deflection in many points [94]. The mode shapes are measured by impulse tests that provide easy and precise method for mode shape identification for any structure.

3.1.1. Experimental procedure for deflection lines determination

The photogrammetric measurement technique is based on a digital photograph of structures with specially selected points. In the case of structural elements with uniform colours, like plexiglass, it is necessary to artificially introduce the measurement marks. In the case of concrete for example, the natural colour irregularities can be used as measurement points. The digital photograph saved in RGB (red, green, blue) space of colours (Fig. 3.1) is transformed into CMYK space (distribution on colours: cyan, magenta, yellow and black) according to the formula:

$$\mathrm{CMYK} = (c-k,\ m-k,\ y-k,\ k), \tag{3.1}$$

where:

$$\begin{aligned} c &= 255-r, \qquad & m &= 255-g, \\ y &= 255-b, \qquad & k &= \min(c,m,y). \end{aligned} \tag{3.2}$$

Colours are marked as follows: c – cyan, m – magenta, y – yellow, k – black, r – red, g – green, b – blue.

From CMYK space of colours, the component linked to magenta colour is chosen for a further processing. The last stage is application of a threshold to the image. The threshold is a process of calculating each output pixel value based on a comparison of the corresponding input pixel with a threshold value t_r. The threshold can provide the separation of the objects from the background. The output value indicates white when the pixel value is greater than t_r, and black otherwise [42]. As a result of using the threshold process, a RGB photograph is transformed into a binary picture (Fig. 3.2). For a given white points on the black background the beam deflections are calculated as centres of gravity of the white pixels areas. The accuracy of this method depends on the photograph resolution.

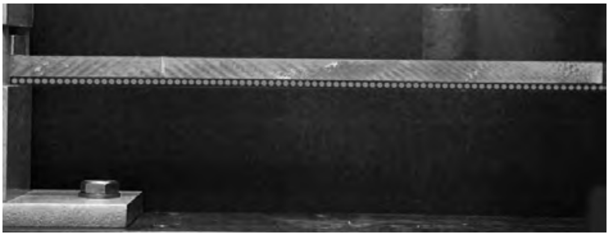

Fig. 3.1. Digital photograph in RGB space of colours

Fig. 3.2. Binary picture

3.1.2. Experimental procedure for mode shapes determination

Any discrete dynamic system can be described by the equations of motion with the initial conditions, e.g. [17–19]:

$$\mathbf{M}\ddot{\mathbf{x}}(t)+\mathbf{C}\dot{\mathbf{x}}(t)+\mathbf{K}\mathbf{x}(t)=\mathbf{f}(t), \quad \mathbf{x}(0)=\mathbf{x}_0,\, \dot{\mathbf{x}}(0)=\dot{\mathbf{x}}_0 \tag{3.3}$$

where $\mathbf{M}$, $\mathbf{C}$, $\mathbf{K}$ are the mass, damping and stiffness matrices, respectively, and $\mathbf{C}$ is assumed as a classical damping matrix. Matrices $\mathbf{M}$, $\mathbf{C}$, $\mathbf{K}$ are of size $n_d \times n_d$, where n_d

denotes the number of degrees of freedom. Solution of eigen problem for the equation of motion without damping:

$$\mathbf{M}\ddot{\mathbf{x}}(t)+\mathbf{K}\mathbf{x}(t)=\mathbf{0}, \tag{3.4}$$

gives the eigenvalues $\omega_{n_k}^2$ and the eigenvectors $\mathbf{u}_k$ (k = 1, 2 ,…, n_d). The n_d eigenvalues $\omega_{n_k}^2$ can be assembled into the diagonal matrix $\mathbf{\Omega}^2$ called the spectral matrix and the n_d eigenvectors can be assembled into the modal matrix **U**. The system described by Eq. (3.3) can be uncoupled using the modal coordinates $\mathbf{q}(t)$:

$$\mathbf{x}(t)=\mathbf{U}\mathbf{q}(t). \tag{3.5}$$

Substituting Eq. (3.5) into Eq. (3.3) yields:

$$\mathbf{U}^T\mathbf{M}\mathbf{U}\ddot{\mathbf{q}}(t)+\mathbf{U}^T\mathbf{C}\mathbf{U}\dot{\mathbf{q}}(t)+\mathbf{U}^T\mathbf{K}\mathbf{U}\mathbf{q}(t)=\mathbf{U}^T\mathbf{f}(t). \tag{3.6}$$

The modal equation (3.6) can be simplified to the form:

$$\bar{\mathbf{M}}\ddot{\mathbf{q}}(t)+\bar{\mathbf{C}}\dot{\mathbf{q}}(t)+\bar{\mathbf{K}}\mathbf{q}(t)=\mathbf{U}^T\mathbf{f}(t), \tag{3.7}$$

where matrices $\bar{\mathbf{M}}$, $\bar{\mathbf{C}}$, $\bar{\mathbf{K}}$ denotes the modal mass, modal damping and modal stiffness matrices. They are of size $m\times m$, where m denotes the number of modes of vibration.

The Laplace transform of the equations of motion (3.3) gives:

$$(\mathbf{M}s^2+\mathbf{C}s+\mathbf{K})\mathbf{X}(s)-\mathbf{M}s\mathbf{X}(0)-\mathbf{M}\dot{\mathbf{X}}(0)-\mathbf{C}\mathbf{X}(0)=\mathbf{F}(s). \tag{3.8}$$

If the initial conditions are zero, the equation (3.8) can be rewritten as:

$$\mathbf{B}(s)\mathbf{X}(s)=\mathbf{F}(s), \tag{3.9}$$

where $\mathbf{B}(s)$ known as a system matrix is given by:

$$\mathbf{B}(s)=\mathbf{M}s^2+\mathbf{C}s+\mathbf{K}. \tag{3.10}$$

The transfer function matrix is defined as follows:

$$\mathbf{H}(s)=\mathbf{B}(s)^{-1}=\frac{\mathrm{adj}\mathbf{B}(s)}{\det\mathbf{B}(s)}=\frac{\mathbf{R}(s)}{\det\mathbf{B}(s)}, \tag{3.11}$$

where $\mathbf{R}(s)$ is called the residue matrix and $\mathrm{adj}\mathbf{B}(s)$ denotes adjugate of matrix $\mathbf{B}(s)$.

The solutions of the system characteristic equation $\det\mathbf{B}(s)=0$ are called the poles:

$$p_k=-\xi\omega_{n_k}\pm i\omega_{d_k}, \tag{3.12}$$

where ξ is a damping ratio, ω_d is a damped circular frequency, ω_n is a natural circular frequency and k = 1, 2 ,…, m. The transfer function matrix in the partial fraction expansion form can be written as:

$$\mathbf{H}(s)=\sum_{k=1}^{m}\left(\frac{\mathbf{R}_k}{s-p_k}+\frac{\mathbf{R}_k^*}{s-p_k^*}\right), \tag{3.13}$$

where $\mathbf{R}_k$ is a residue matrix $n_d\times n_d$ for the k^{th} mode. Residues are related to mode shapes and can be determined from Laplace transform of Eq. (3.7):

$$\mathbf{R}_k = t_k \mathbf{u}_k \mathbf{u}_k^T, \quad k = 1, 2, ..., n_d, \tag{3.14}$$

where t_k is a scaling factor for the k^{th} mode.

Evaluating the transfer function matrix described by Eq. (3.13) along frequency axis ($s = i\omega$) results in the frequency response function matrix given as:

$$\mathbf{H}(\omega) = \sum_{k=1}^{m} \left(\frac{t_k \mathbf{u}_k \mathbf{u}_k^T}{i\omega + \xi\omega_{n_k} - i\omega_{d_k}} + \frac{t_k^* \mathbf{u}_k^* \left(\mathbf{u}_k^*\right)^T}{i\omega + \xi\omega_{n_k} + i\omega_{d_k}} \right). \tag{3.15}$$

The relationship between the displacement response and the excitation force transformed to frequency domain is called the receptance [62]:

$$H_{jk}(\omega) = \frac{X_j(\omega)}{F_k(\omega)}. \tag{3.16}$$

However, the dynamics properties of a system, expressed in terms of displacements, can be converted into accelerations and in that case is called the accelerance:

$$A_{jk}(\omega) = \frac{\ddot{X}_j(\omega)}{F_k(\omega)}. \tag{3.17}$$

The relationship between the accelerance and the receptance is given by:

$$A_{jk}(\omega) = -\omega^2 H_{jk}(\omega). \tag{3.18}$$

The receptance expressed in terms of the accelerations is:

$$H_{jk}(\omega) = \frac{-1}{\omega^2} \frac{\ddot{X}_j(\omega)}{F_k(\omega)}. \tag{3.19}$$

The receptance and accelerance describe the same dynamic properties of the system; however in the experimental works the accelerance is more convenient, whereas the receptance is often used in analytical works [62].

The matrix $\mathbf{H}(\omega)$ of the size $n_d \times n_d$, where n_d denotes number of degrees of freedom, contains the individual frequency response functions (FRFs) $H_{jk}(\omega)$ determined by impacting at point *k* and measuring the response at point *j*. To obtain one row of the FRF matrix $\mathbf{H}(\omega)$, the modal hammer signal is measured in all points, whereas the acceleration is measured in the same selected point. To determine one column of the FRF matrix $\mathbf{H}(\omega)$, the modal hammer signal is measured in one point, whereas the acceleration signals are collected in all points. The mode shape is contained in each row or column of the residue matrix. Therefore, the imaginary part ofc FRF $H(\omega)$ shows both the amplitude and direction of the response.

In this study impulse vibration testing is used as a technique for the mode shape determination. During measurements the acceleration and force signals are collected. The time signals are transformed into a frequency domain by the fast Fourier transform. Then FRF is computed. The examples of the time signals $f(t)$ and $\ddot{x}(t)$ are shown in Fig. 3.3. Their frequency representations $F(\omega)$ and $\ddot{X}(\omega)$ are given in Fig. 3.4. The example of the imaginary part of FRF is illustrated in Fig. 3.5.

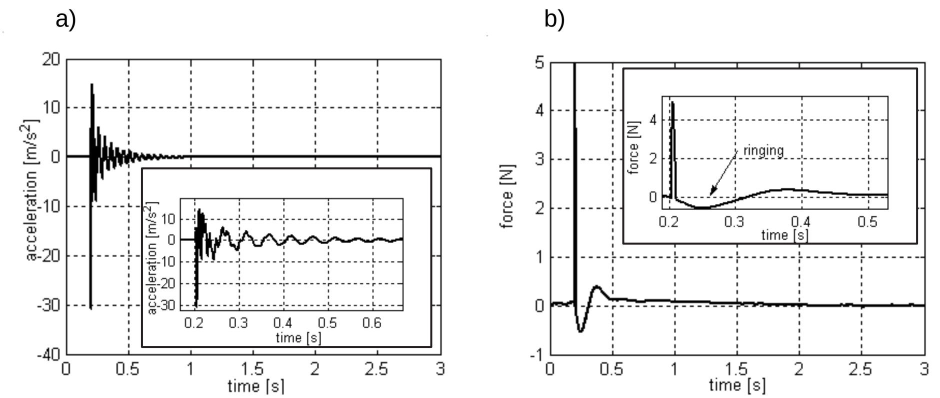

Fig. 3.3. Signals in time domain: a) acceleration signal; b) force signal

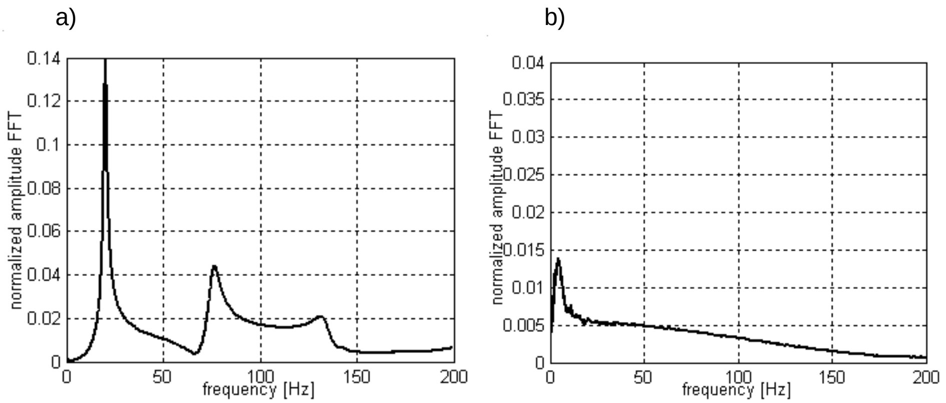

Fig. 3.4. Signals in frequency domain: a) acceleration signal; b) force signal

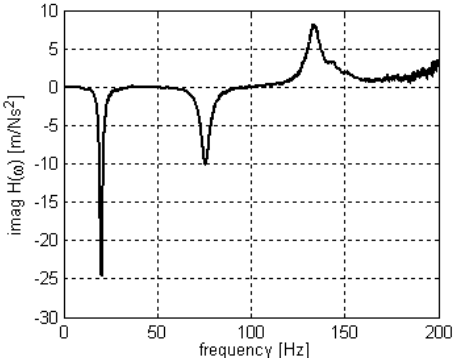

Fig. 3.5. Imaginary part of FRF

In practice, every measurement is affected by the errors from environmental conditions, temperature, humidity, cable noise, mounting the transducer, transducer mass, limited instrumentation resolution, etc. [67]. Therefore, determination of FRF is performed to minimize a noise in the response. Each acceleration and force measurement is repeated several times and data are several times averaged in the frequency domain. There are two estimators used depending on noise appearance i.e. $H_1(\omega)$ estimator is used in the case of noise in the output, whereas $H_2(\omega)$ is used in the case of noise in the input measurements [62]:

$$H_1(\omega) = \frac{G_{FX}(\omega)}{G_{FF}(\omega)}, \tag{3.20}$$

$$H_2(\omega) = \frac{G_{XX}(\omega)}{G_{XF}(\omega)}, \tag{3.21}$$

where: $G_{FX}(\omega)$ - cross spectrum between the response and the force, $G_{XF}(\omega)$ - cross spectrum between the force and the response, $G_{XX}(\omega)$ - autospectrum of the response, $G_{FF}(\omega)$ - autospectrum of the force. The cross spectra and autospectra are estimated by:

$$\begin{aligned} G_{FX}(\omega) &= \lim_{n\to\infty}\frac{1}{n}\sum_{i=1}^{n} F_i^*(\omega)X_i(\omega), \\ G_{XF}(\omega) &= \lim_{n\to\infty}\frac{1}{n}\sum_{i=1}^{n} X_i^*(\omega)F_i(\omega), \\ G_{XX}(\omega) &= \lim_{n\to\infty}\frac{1}{n}\sum_{i=1}^{n} X_i^*(\omega)X_i(\omega), \\ G_{FF}(\omega) &= \lim_{n\to\infty}\frac{1}{n}\sum_{i=1}^{n} F_i^*(\omega)F_i(\omega), \end{aligned} \tag{3.22}$$

where $F(\omega)$, $X(\omega)$ are the Fourier transforms of the force $f(t)$ and response $x(t)$, respectively, and $F^*(\omega)$, $X^*(\omega)$ are the complex conjugated to $F(\omega)$ and $X(\omega)$, respectively.

A significant noise problem occurring during impact testing is linked with input measurements [67]. An input signal should be zero for over 99 percent of the time range. However, the input signals are not free from contaminations due to a cable noise. Additionally a ringing phenomenon, visible in Fig. 3.3b, can occur. At last, there is a difficulty with the impacting exactly at the selected point. Therefore, $H_2(\omega)$ estimator is proposed to use in the impulse vibration tests. The imaginary part of the FRF estimator $H_2(\omega)$ is presented in Fig. 3.6.

An indicator of the quality of the experimental works is the coherence function defined as the ratio of two estimators [51]:

$$\gamma^2(\omega) = \frac{H_1(\omega)}{H_2(\omega)} = \frac{\left|G_{FX}(\omega)\right|^2}{G_{XX}(\omega)G_{FF}(\omega)}. \tag{3.23}$$

The coherence determines the degree of linearity between output and input in the frequency domain. It can reach the values between zero and one. The coherence equal one means no noise in the measurements whereas coherence equals zero means pure noise. The example of the coherence function is shown in Fig. 3.7.

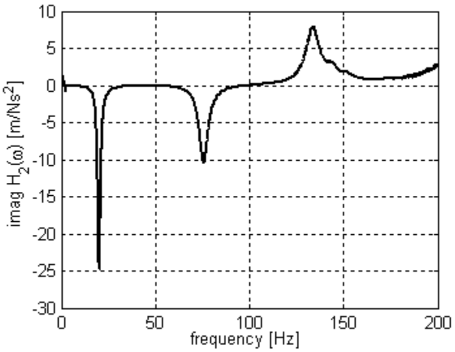

Fig. 3.6. Imaginary part of FRF estimator $H_2(\omega)$

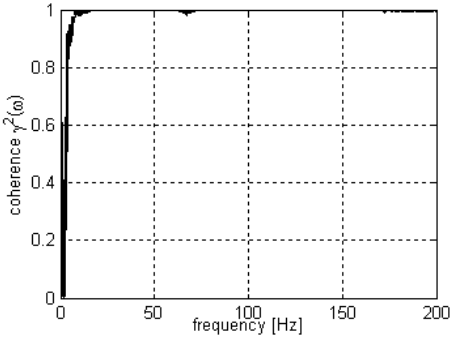

Fig. 3.7. Coherence function

3.2. Wavelet selection for damage detection

3.2.1. One-dimensional wavelets

The selection of an appropriate type of the wavelet and the choice of its number of vanishing moments is essential for effective use of the wavelet analysis in damage detection. The possibility of damage detection by the Haar [72, 87, 115] Gabor [87, 115], Mexican hat [39, 72], Symlet [24, 25, 72], Coiflet [72, 98] or Gaussian wavelets [31, 69, 96, 98] has been discussed. Hong *et al.* [39] proved that in the case of crack detection in beams the number of the vanishing moments should be at least 2. Douka *et al.* [24] stated that in practice the wavelet having higher number of vanishing moments provides more stable performance. However, this proposal cannot be extended to infinity. Since wavelets with vanishing moments have longer supports, the trade-off between the number of vanishing moments and the support sizes must be considered.

A static deflection line of a cracked cantilever beam under the uniformly distributed load and point load can be described as a combination of polynomials of the 4th order. An example of the beam displacement line $f(x)$, described further in section 4.1 (case 3 from Table 4.1), is given in Fig. 3.8. The left side of Fig. 3.8 shows 1st, 2nd, 3rd and 4th derivative of the displacement line, while the transforms of $f(x)$ by the Gaussian wavelet with 1, 2, 3 and 4 vanishing moments and scale 8 are shown on the right side. This example clearly illustrates the differential action of the wavelets. The similar comparison between the derivatives and the wavelet transforms acting on the mode shape cantilever cracked beam is presented in Fig. 3.11. Both the numerical results of the static deflection line (Fig. 3.8) and the mode shape (Fig. 3.11) were determined with high precision (ten significant numbers). Note that the numerical differentiation of $f(x)$ could not be precisely determined even though the signal $f(x)$ is obtained numerically with high precision. In the case of numerical differentiation of the mode shape the results are poor. The derivatives of the beam responses determined numerically with normal precision (four significant numbers) and experimentally are given in Fig. 3.9 and Fig. 3.10, respectively. It is noted that the derivatives consist of a noise. Using of the wavelet transform instead of differentiation provides the noise-free response even in the case of the experimental data. Advantage of wavelet analysis is the fact that it produces information about derivatives without performing the numerical differentiation.

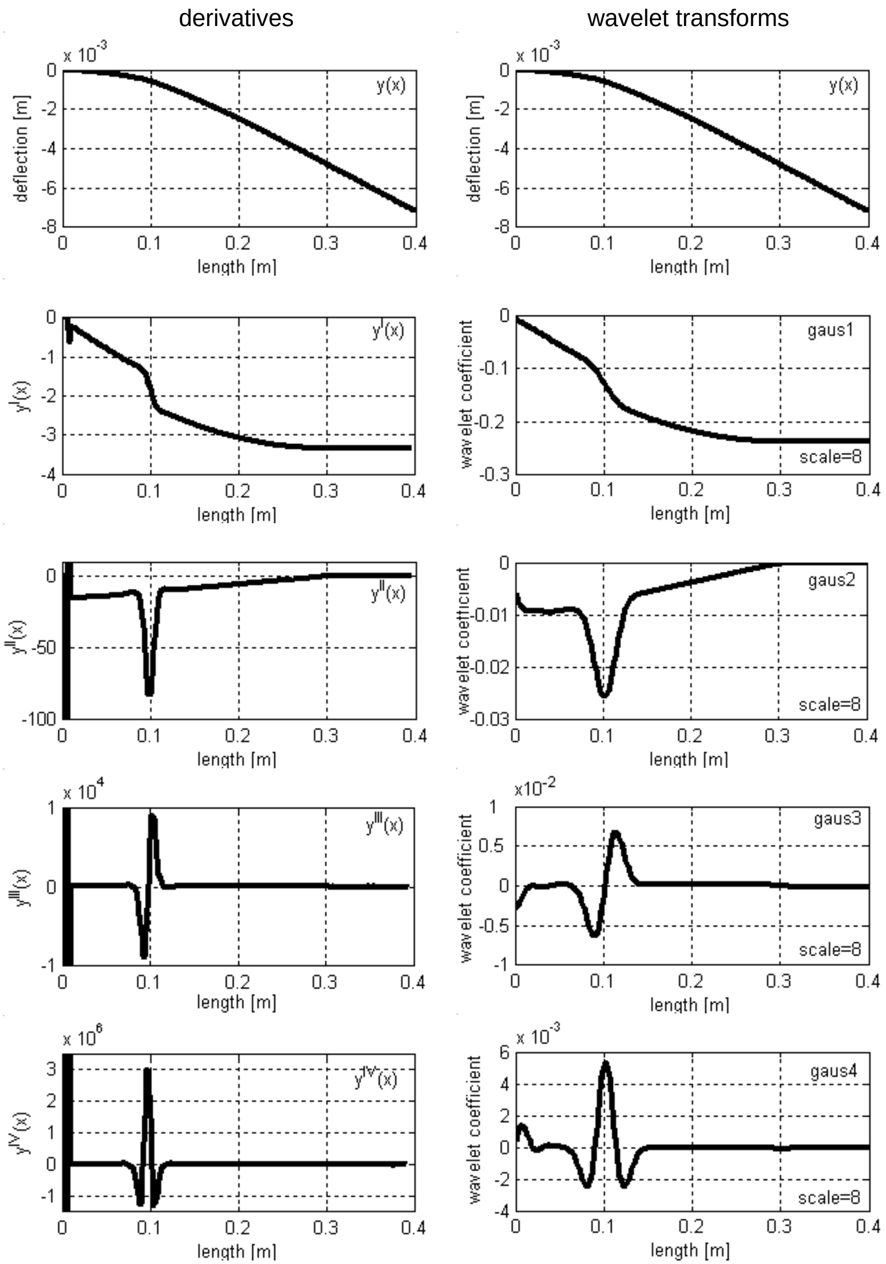

Fig. 3.8. Derivatives and wavelet transforms of static deflection line of beam case 3 from Table 4.1 (high precision)

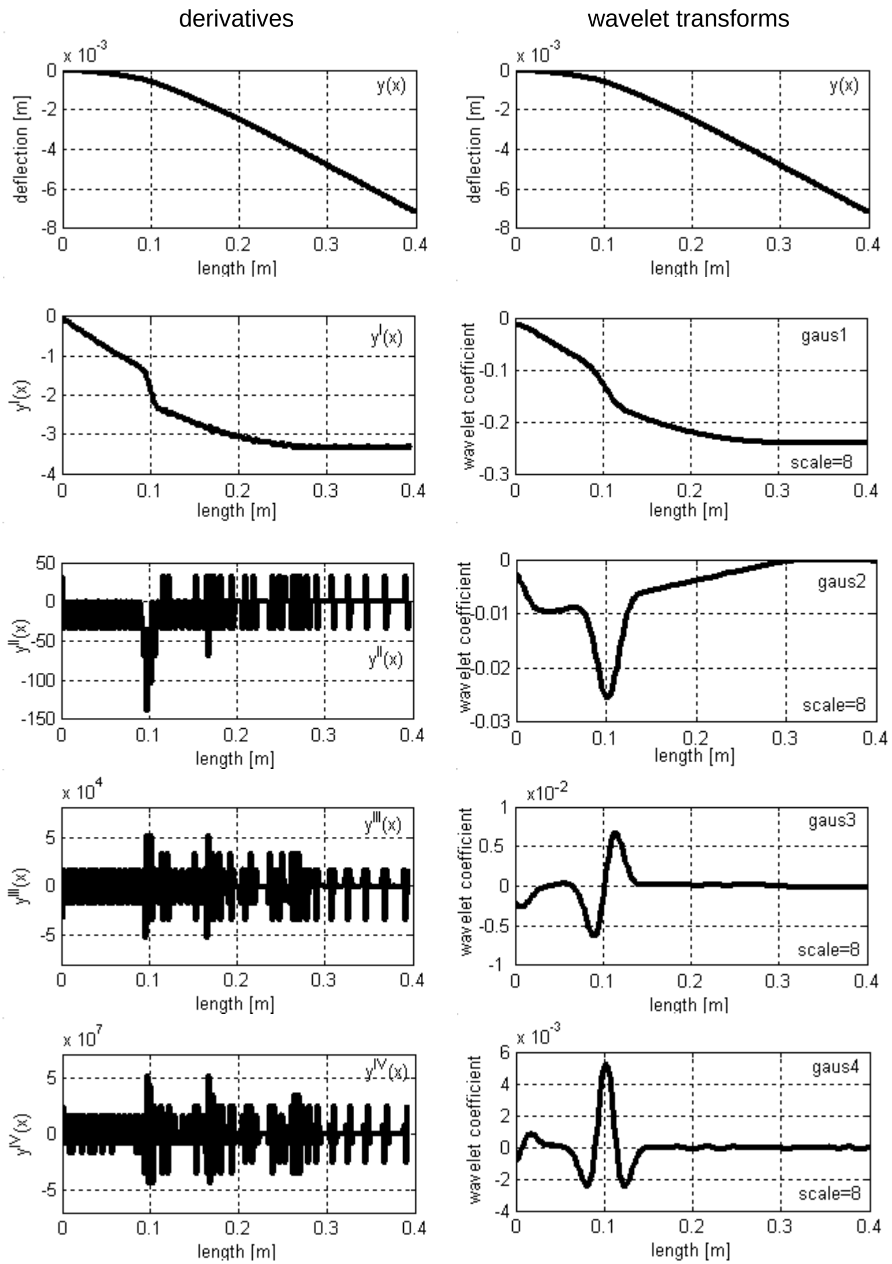

Fig. 3.9. Derivatives and wavelet transforms of static deflection line of beam case 3 from Table 4.1 (normal precision)

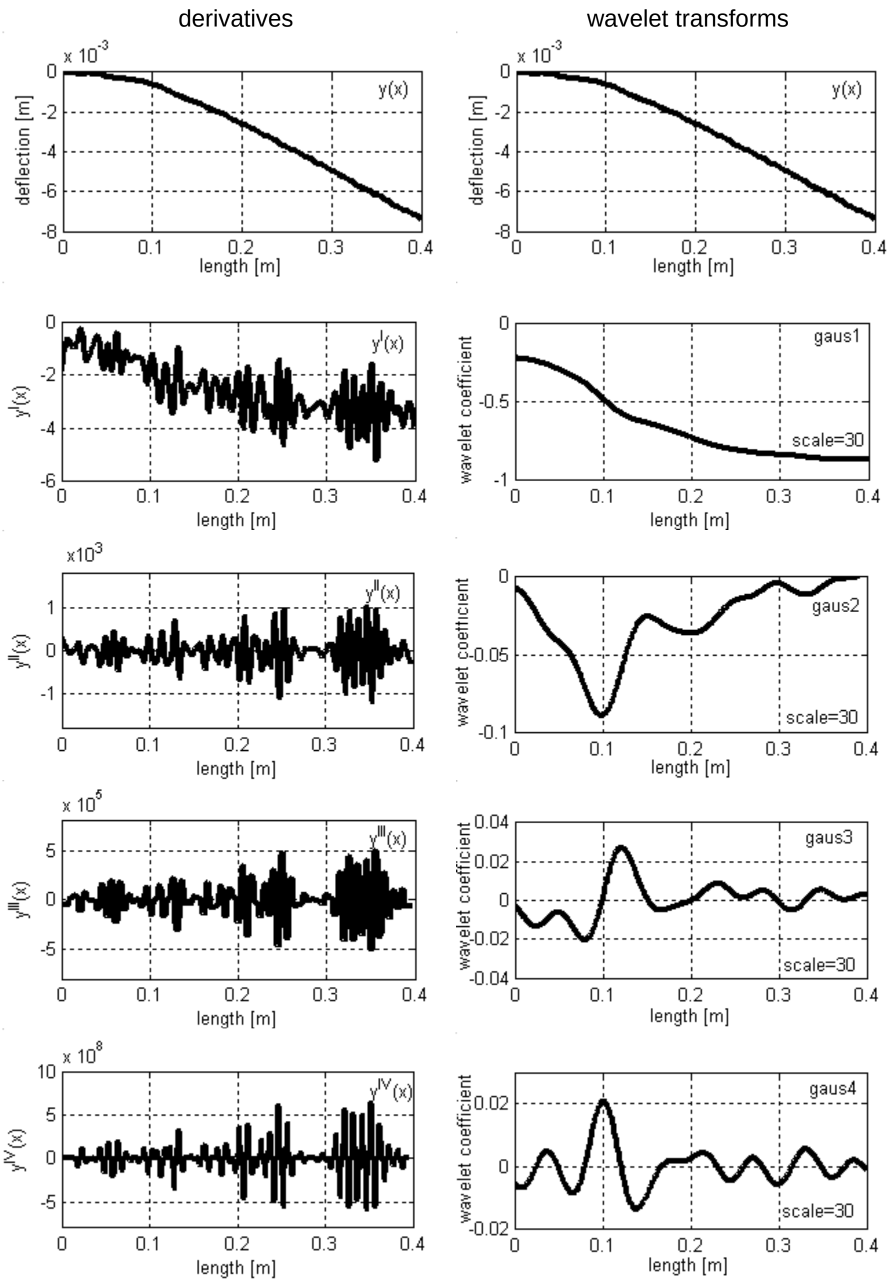

Fig. 3.10. Derivatives and wavelet transforms of static deflection line of beam case 3 from Table 4.1 (experimental data)

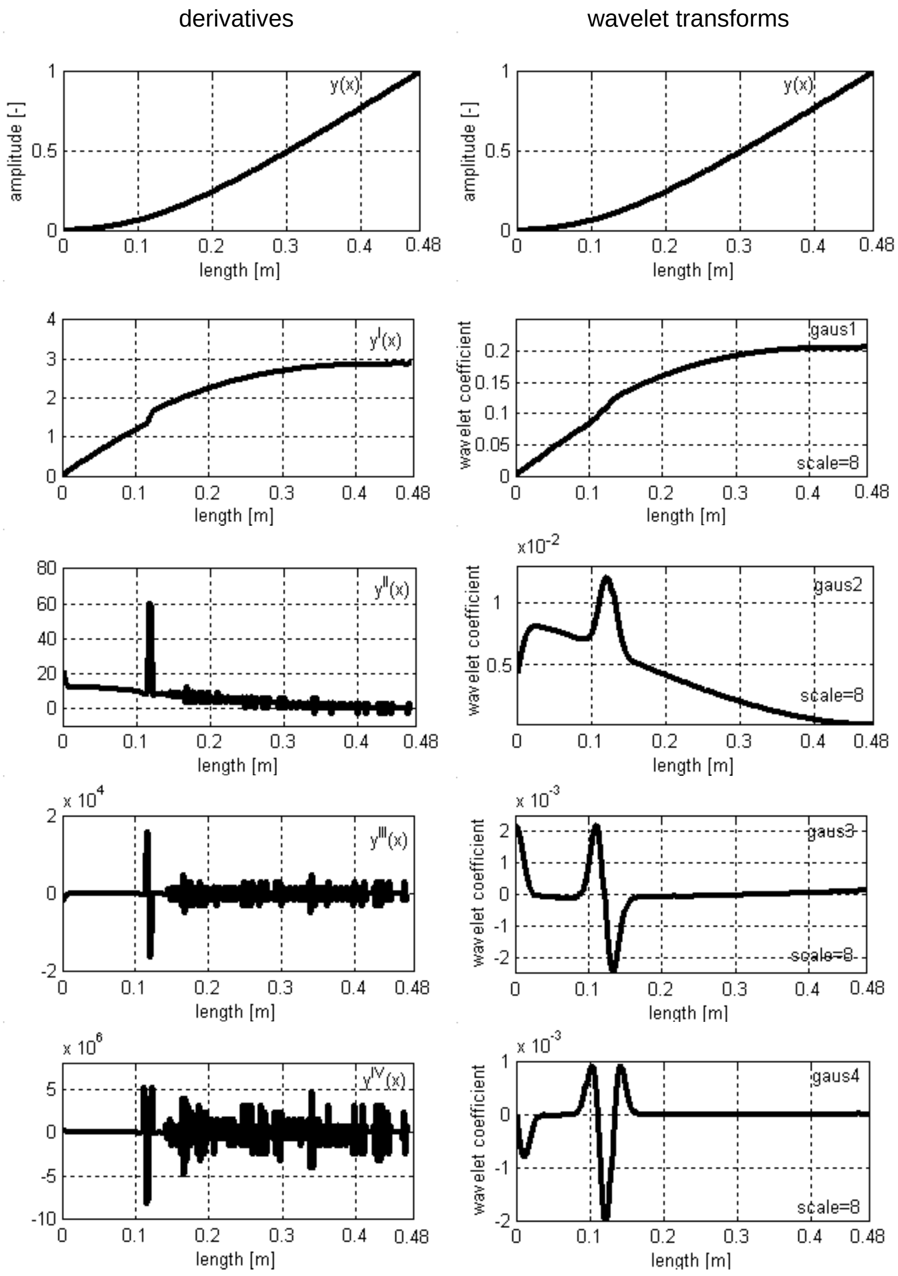

Fig. 3.11. Derivatives and wavelet transforms of mode shape line of beam case 1 from Table 4.3 (high precision)

As it is shown in Fig. 3.11, only wavelets with 2 or 4 vanishing moments can indicate damage position as a local maximum, whereas the wavelet with three vanishing moments reaches zero at the damage position. The wavelets with 2 vanishing moments have shorter length (Fig. 3.12) but they produce wavelet coefficients different from zero for all lengths (Fig. 3.14).

However, it can be observed, that the wavelet with four vanishing moments (Fig. 3.13) guarantee that non-zero values of the wavelet coefficients correspond only to the abnormalities of the signal, as it is shown in Fig. 3.15. Using the wavelets that create the maximum number of wavelet coefficients that are close to zero is proposed in this study.

The design of wavelet optimized to produce the maximum number of wavelet coefficients that are close to zero depends mostly on the number of vanishing moments and the size of the support of the wavelet function. The support size and the number of vanishing moments are independent. However, the constrains imposed on the orthogonal wavelets imply that if $\psi(x)$ has n vanishing moments then its supports have length at least $2n$-1 [63]. The Daubechies wavelets are optimal in the sense that they have a minimum size support for a given number of vanishing moments. Nevertheless, the Daubechies wavelets are very irregular and regularity of $\psi(x)$ function has a large influence on applicability in damage detection.

If a beam would have only few isolated singularities a wavelet with many vanishing moments should be chosen. Supposing that the structure response would have singularities in density distances it might be better to decrease the size of the support at the cost of reducing the number of vanishing moments.

After the extensive numerical experimentations the Gaussian wavelet (gaus4) was chosen as the best candidate to damage detection with the one-dimensional continuous wavelet transform. For the structural responses that are similar to polynomial of higher order than 4, the use of wavelets with higher number of vanishing moments is necessary (gaus6 or higher).

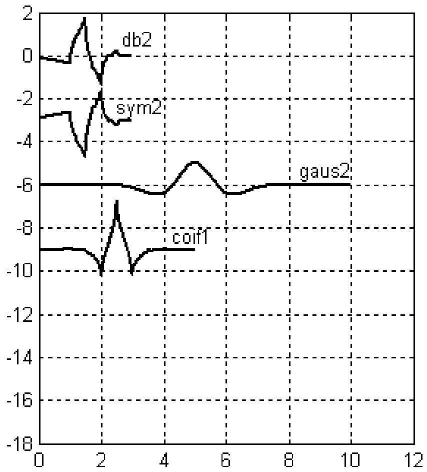

Fig. 3.12. Wavelets having two vanishing moments

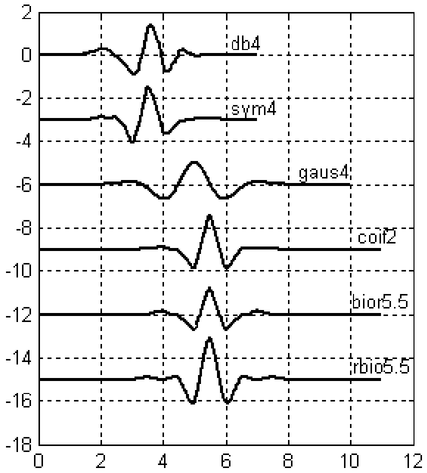

Fig. 3.13. Wavelets having four vanishing moments

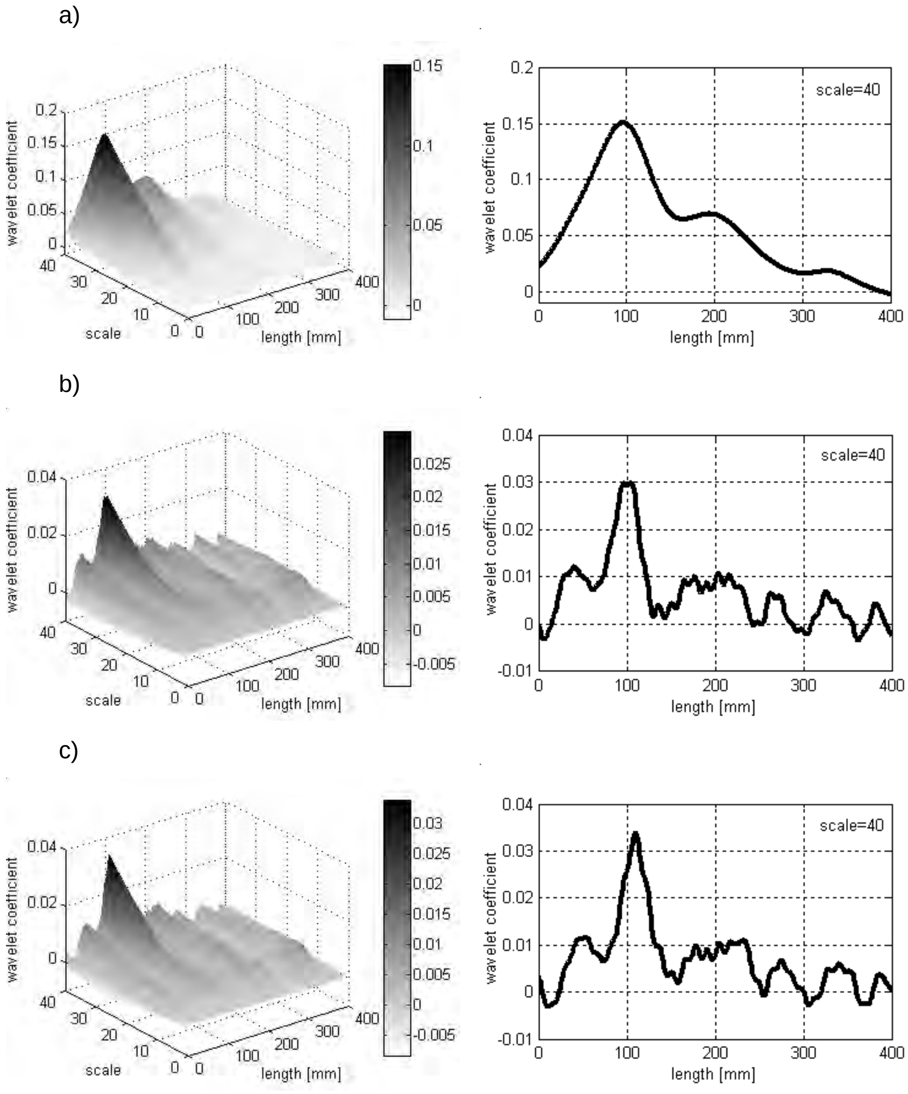

Fig. 3.14. Wavelet transforms of beam deflection line (beam case 3 from Table 4.1) using wavelets with 2 vanishing moments: a) gaus2; b) coif1; c) db2

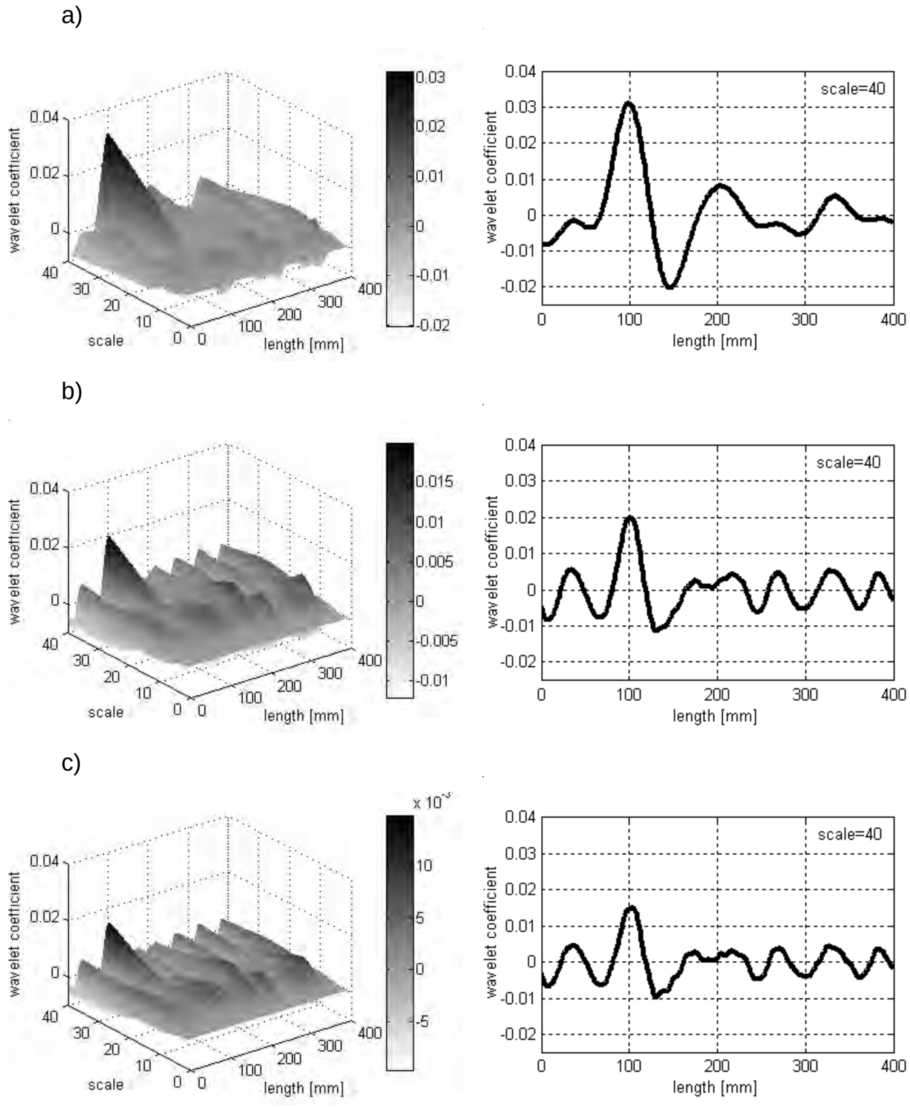

Fig. 3.15. Wavelet transforms of beam deflection line (beam case 3 from Table 4.1) using wavelets with 4 vanishing moments: a) gaus4; b) rbio5.5; c) coif2; d) sym4; e) bior5.5; f) db4

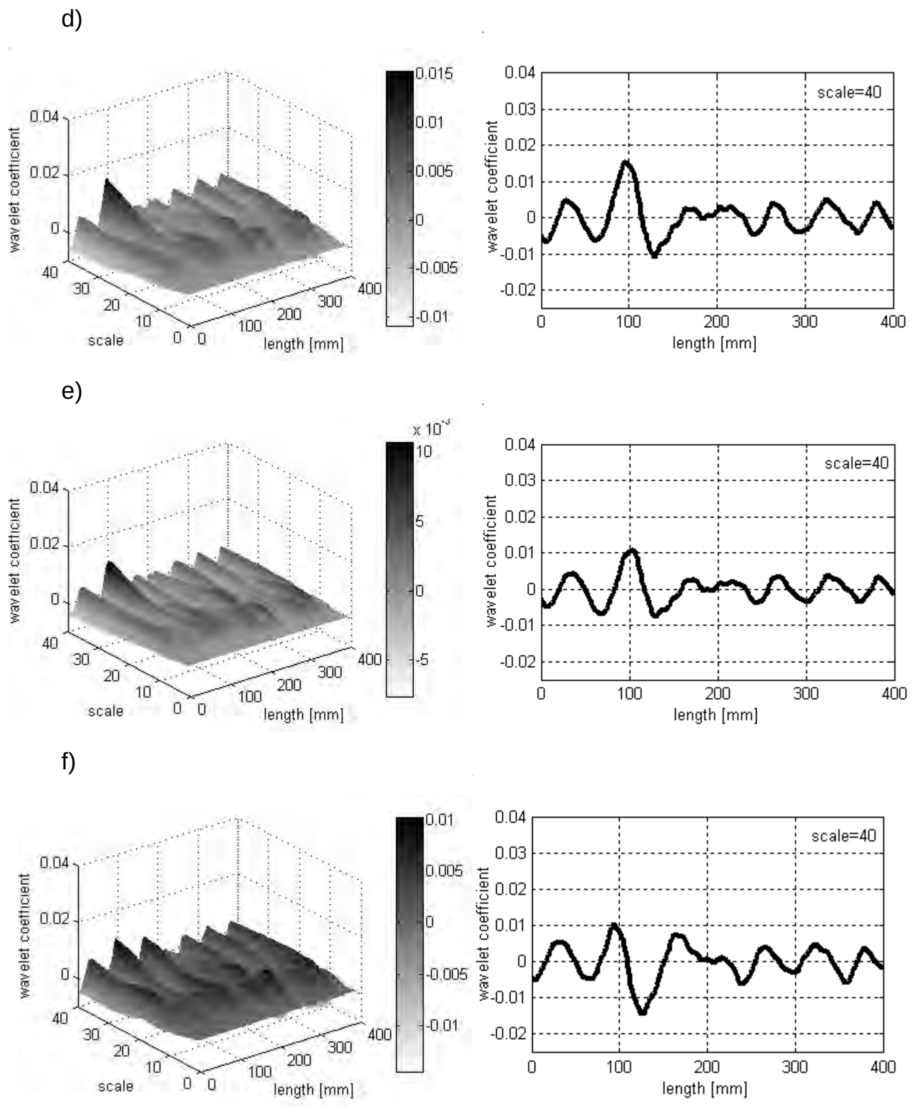

Fig. 3.15. (continued)

3.2.2. Two-dimensional wavelets

As the best candidate selected to the one-dimensional wavelet transform, namely the Gaussian wavelet, does not have a scaling function, it cannot be used to two-dimensional analysis. The Reverse Biorthogonal wavelet (rbio5.5) with four vanishing moments was chosen as the best candidate in the two-dimensional wavelet transform (Fig. 2.18).

3.3. Discrete and continuous wavelet transform in damage detection

3.3.1. One-dimensional wavelet transform

In order to limit computations time as well as the memory requirements, it is possible to change a continuous scale to a variations scale limited to dyadic sequence ($s = 2^j$) leading to the discrete wavelet transform (DWT). The DWT is particularly suitable in denoising and compressing of the signal problems or image processing for edge detection where the analysis is conducted at fine scales. However, in the case of damage location in structures, higher scales are required. Thus the DWT has two disadvantages in using it to damage detection. The length of the wavelet coefficients vector decreases to half of its initial length on each level *j*. Second disadvantage is the fact, that scale is limited to dyadic sequence ($s = 2^j$). Therefore, between $s = 32$ and $s = 64$ there is a big gap in wavelet resolution and an important information might be lost. It can be compared with searching of cracks on a concrete wall during night, using only a flashlight. If the light is directed to one part of the wall, then switched off and next moved for another part, some of cracks can be missed or no crack can be discovered. But if the light is moved continuously along the wall all, cracks can be found.

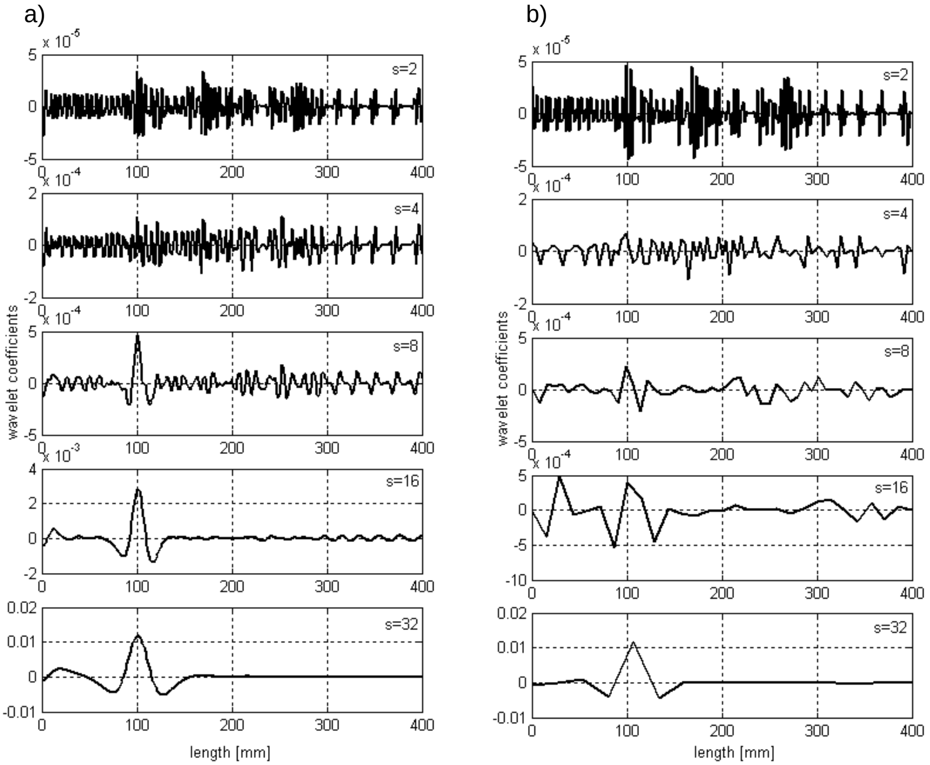

Fig. 3.16. Wavelet coefficients of numerical static deflection line (beam case 3 from Table 4.1): a) CWT; b) DWT

Therefore, the costs of computations cannot be limited in this case and application of the continuous scales is recommended. A comparison the continuous wavelet transform (CWT) results with the discrete wavelet transform results is given in Fig. 3.16 (numerical data) and Fig. 3.17 (experimental data).

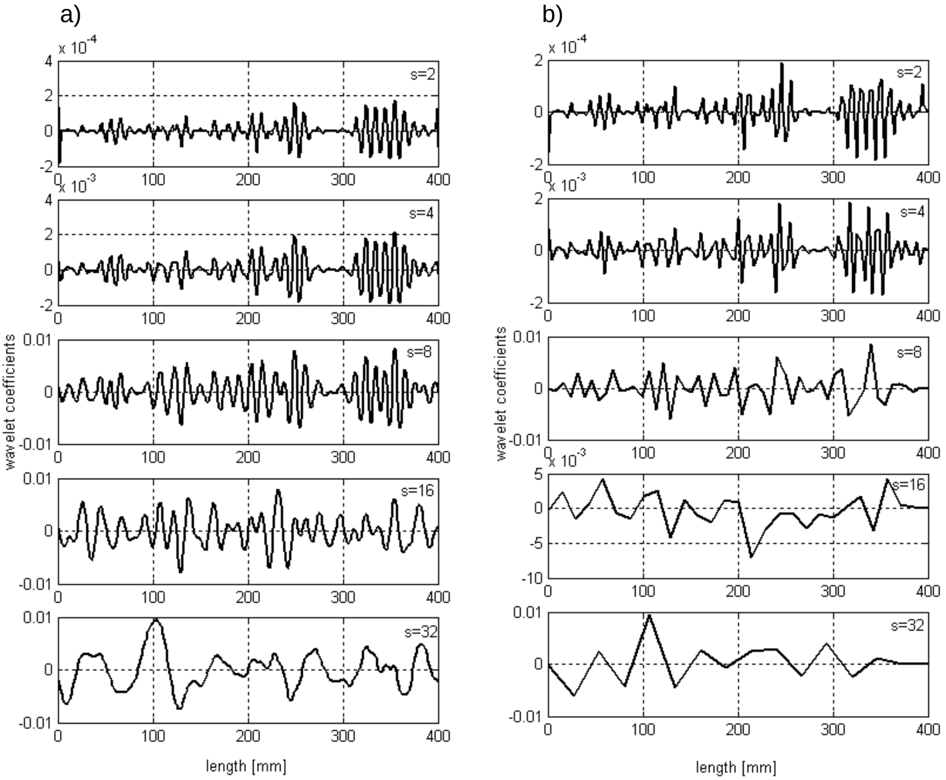

Fig. 3.17. Wavelet coefficients of experimental static deflection line (beam case 3 from Table 4.1): a) CWT; b) DWT

3.3.2. Two-dimensional wavelet transform

As in the case of the one-dimensional discrete wavelet transform, the two-dimensional DWT is very useful tool but its applicability to damage detection problems is limited. The two-dimensional DWT is very helpful in image recognition and edge detection, but searching singularities is a task for the two-dimensional CWT.

3.4. Boundary effects

3.4.1. One-dimensional wavelet transform

The wavelet transform is defined as integral of the product of the wavelet and the signal of infinite length, i.e. $x \in <-\infty, \infty>$. Since deflection of a beam $f(x)$, treated as a spatially distributed signal, has a finite length, i.e. $x \in < 0, L >$, a border distortion problem appears. The wavelet coefficients achieve an extremely high value at the signal ends. Therefore, the border of the signal should be treated independently from the rest of the signal. The influence of boundary effects can be reduced by extension from the signal beyond the boundary. It is obvious that the length of the extended signal depends on the scale of the used wavelet. The edge effect width can be estimated as a half width of the wavelet with the highest scale.

There are some possibilities to extend the signal, e.g.: extension by zeros, by reflection, by periodicity and by extrapolation [72, 107]. The extension by zeros assumes that the signal is zero outside the domain. This method creates artificial discontinuities at the border. Another method is extension of the signal by reflection that assumes recovery of the signal outside its original support by symmetric boundary value replication. The reflection generally introduces discontinuities in the first derivative at the border. It is also possible to recover the signal by its periodic extension. This method also creates discontinuities at the borders.

In this study, to avoid large discrepancy at the boundaries, the signal is extended outside its original support by a cubic spline extrapolation based on three neighbouring points. An example of a beam deflection line signal used for the wavelet transform analysis is given in Fig. 3.18. The spline provides a technique for obtaining a smoother interpolation. Extrapolation is continuous, with continuous first and second derivatives. Only the third derivative is allowed to have jumps at the connection points.

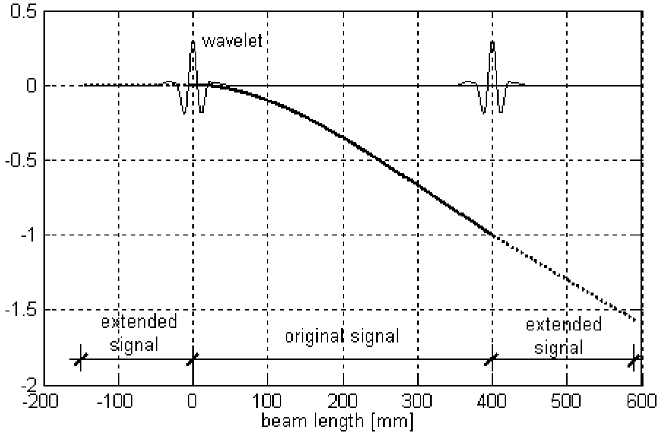

Fig. 3.18. Wavelet transform action on the extended signal

3.4.2. Two-dimensional wavelet transform

The mode shape of the plate $f(x, y)$, treated as a spatially distributed signal, has a finite length and width, i.e. $x \in < 0, L >$ and $y \in < 0, B >$, therefore, a border distortion problem appears. As in the case of one-dimensional signals, the two-dimensional signal is extended outside its original support by a cubic spline extrapolation based on three neighbouring points. The spline extrapolation is continuous, with continuous first and second derivatives. However, the fourth derivative used in this study is allowed to have jumps at the connection points. Therefore, the integration of the wavelet function with the mode shape near the location of the plate edges result in non zero value of the CWT coefficients. These maxima near the sides of the plate cannot be considered as indication of damage.

3.5. Summary and conclusions

In this chapter, the application of the wavelet analysis in damage detection has been presented. The four main issues has been taken into consideration, namely the way of the static deflections or mode shapes determination, the appropriate wavelet function selection, the choice between continuous wavelet transform and the discrete wavelet transform, and finally, the border distortion problem.

The determination of the static deflection lines by the photogrametric method has been proposed and applied in the cantilever beam. The method accuracy depends on picture resolution. The advantage of the method is possibility of the simultaneous measurements of the static deflection in large number of spatially distributed points. The proposed method can be extended to determined operational deflection shapes of a structure using digital camera, which can record the motion of the structure.

The mode shapes determination has been conducted by impact testing using a modal hammer. The method enables the precise mode shape identification at large number of points. The existing errors in measurements (environmental conditions, cable noise, the inaccuracy in mounting the accelerometer and place of impact) have been reduced by application of the frequency response function estimator $H_2(\omega)$.

The selection of the appropriate type of wavelet has been conducted. The best candidate to damage detection is a symmetrical wavelet with minimum 4 vanishing moments. For one-dimensional wavelet analysis the Gaussian wavelet has been chosen, whereas the Reverse Biorthogonal wavelet was chosen for the two-dimensional transform.

In this chapter, the advantage of the CWT over the DWT in damage detection has been discussed. CWT provides better resolution necessary for successful damage localization. It is also shown that the CWT acts as a differential operator and can be effectively applied for noisy signals.

The border solution problem has been considered. It has been found that the better way to avoid the border distortion is an extension of the signal by a cubic spline extrapolation.

Chapter 4

DAMAGE DETECTION ON EXPERIMENTAL EXAMPLES

4.1. Beam – static deflection lines

4.1.1. Experimental investigations of beam deflection lines

A cantilever beam (Fig. 4.1) of length L, height H and width B is considered. The beam is made of polymethyl methacrylate (PMMA), which is commonly called the plexiglass or the acrylic glass. The tests were carried out on two types of the cantilever beams of different cross sections and material properties. Material characteristics (Young's modulus, Poisson ratio and mass density) were determined experimentally. The first type of beams (cases 1 to 10 from Table 4.1) is characterized by Young's modulus $E = 3317$ MPa, Poisson ratio $\nu = 0.32$ and mass density $\rho = 1187$ kg/m^3. The properties of the second type of beams (cases 11 to 13 from Table 4.1) are: Young's modulus $E = 3450$ MPa, Poisson ratio $\nu = 0.36$ and mass density $\rho = 1044$ kg/m^3. Some beams contain an open crack of length L_r and depth a at distance $L_1 = 100$ mm from the clamped end. Descriptions of the geometry of the beams and sizes of cracks for individual beams are given in Table 4.1.

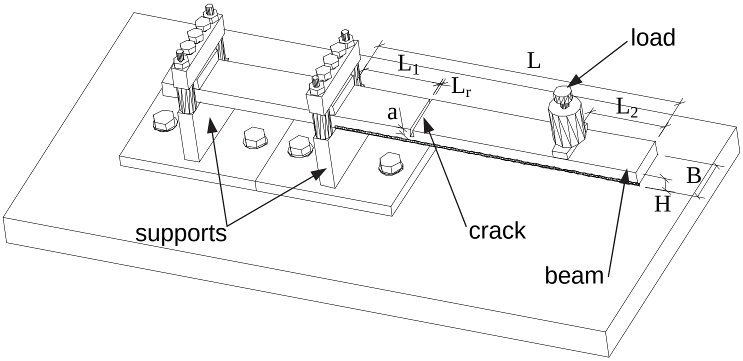

Fig. 4.1. Experimental setup

Each beam was subjected to a static load applied at the distance $L_2 = 100$ mm from the free end of the beam. The three levels magnitudes of the static load were $F = 9.81$ N, $F = 19.62$ N, $F = 49.05$ N for the cases 1 – 10 and $F = 0.1962$ N, $F = 0.4905$ N, $F = 0.6869$ N for the cases 11 – 13. In the experiment, steel weights were used as loads. They were put on the beam using a plexiglass washer. After the removal of one weight and before the application of another one, 60 second intervals were applied to compensate the rheological effects.

Table 4.1

Experimental programme

Case no.	Dimensions of beam			Size of crack	
	Length L [mm]	Height H [mm]	Width B [mm]	Length L_r [mm]	Depth a [mm]
1	400	20	60	0	0
2				2	7
3				2	10
4				2	13
5				4	7
6				4	10
7				4	13
8				6	7
9				6	10
10				6	13
11		3.7	40	0	0
12				5	1
13				5	2

The beam displacements at spatially distributed points were determined by the photogrammetric measurement technique. The one side of the beam was equipped with 81 points of diameter 3.7 mm used to track the beam displacement. The pink points were placed at a distance of 5 mm. Then digital photographs of beams under a dead load and static point loads F were taken. Measurements for all cases presented in Table 4.1 were repeated three times. The digital photographs of the beam were taken by Sony digital still camera DSC-F707. The possible size of the pictures obtained by this equipment was 5 megapixels.

The displacement profile estimation was conducted according to the procedure described in section 3.1.1. Fig. 4.2 shows the digital photograph of the cantilever beam saved in the RGB format. From the CMYK colour space component linked with magenta was chosen for a further processing. Then each output pixel value was compared to the designed threshold and converted to black or white. Hence, white pixels were representing the tracking points on the black background (Fig. 4.3). The beam deflections (Fig. 4.4) in 81 points were calculated with the accuracy corresponding to one pixel size of 0.17 mm.

To verify the credibility of the proposed method, the displacements of the beam at several selected points were measured by the displacement gauges. The displacements of the free end of the non-cracked beam (case 1) and the cracked beam (case 9) are presented in Table 4.2. The variables used in Table 4.2 are define as follows: u_0 denotes the beam displacement under a dead load, u_F is a displacement of the beam loaded by a concentrated static force F at a distance of 100 mm from the beam free end. The differences between the photogrammetrically measured deflections relative to the deflections measured using the displacement gauges vary from 0.1% to 5.8%.

Since the beam displacements were measured at a sampling distance of 5 mm, a piecewise cubic spline data interpolation was used to increase the number of points from 81 to 401. Then each deflection line was normalized to 1.

Table 4.2

Displacement of the free end of non-cracked beam

Case no.	Static load F [N]	Static displacement of a free end of a beam $u_F - u_0$ [mm]		
		Numerical	Experimental	
		FEM	Photograph	Displacement gauge
1	9.81 19.62 49.05	1.017 2.035 5.087	1.033 2.008 5.317	– 2.010 5.025
2	9.81 19.62 49.05	1.146 2.293 5.733	1.304 2.340 6.052	– – –
3	9.81 19.62 49.05	1.343 2.685 6.714	1.527 2.859 7.036	– – –
4	9.81 19.62 49.05	1.901 3.802 9.505	1.944 3.760 10.167	– – –
5	9.81 19.62 49.05	1.168 2.336 5.839	0.966 2.323 6.027	– – –
6	9.81 19.62 49.05	1.400 2.799 6.999	1.481 2.925 7.060	– – –
7	9.81 19.62 49.05	2.084 4.168 10.419	2.030 4.357 11.133	– – –
8	9.81 19.62 49.05	1.189 2.377 5.942	1.136 2.390 6.238	– – –
9	9.81 19.62 49.05	1.455 2.909 7.274	1.392 2.818 7.585	– 2.914 7.285
10	9.81 19.62 49.05	2.266 4.532 11.332	2.334 4.907 11.818	– – –
11	0.1962 0.4905 0.6867	4.569 11.647 16.306	4.906 11.965 16.727	– – –
12	0.1962 0.4905 0.6867	5.056 12.640 17.696	4.922 12.306 17.343	– – –
13	0.1962 0.4905 0.6867	6.088 15.221 21.309	6.358 15.954 22.254	– – –

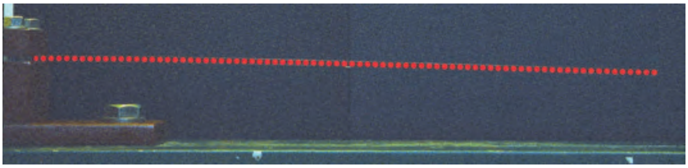

Fig. 4.2. Digital photograph of cantilever beam

Fig. 4.3. Binary picture

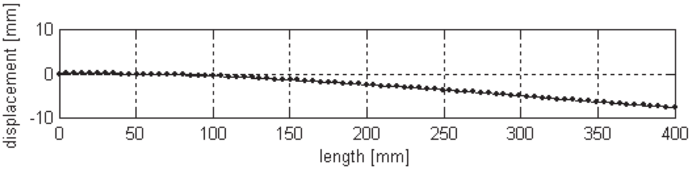

Fig. 4.4. Displacement of cantilever beam obtained from digital photograph

4.1.2. Numerical simulations

The deflection lines for all cases of the cracked beams taken into consideration (Table 4.1) were computed by the commercial finite element method (FEM) program SOFiSTiK. A solid six-sided element with eight nodes was chosen [30]. The applied mesh is shown in Fig. 4.6. For the cases from 1 to 10 the displacement data follow the sampling distance of 2 mm results in a number of 201 points along a beam length whereas for the cases from 11 to 13 the displacement data follow the sampling distance of 1.25 mm results in a number of 321 points along a beam length.

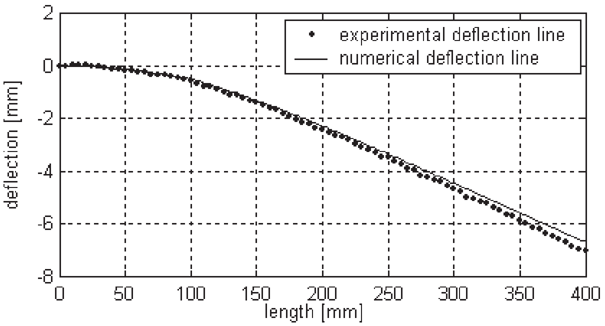

Fig. 4.5. Experimental and numerical deflection lines (beam case 3 from Table 4.1)

As in the case of the experimental data, the number of points was increased up to 401 by cubic spline interpolation and next each deflection line was normalized to 1.

A comparison of the numerical calculated static deflection line with experimentally determined ones is illustrated in Fig. 4.5.

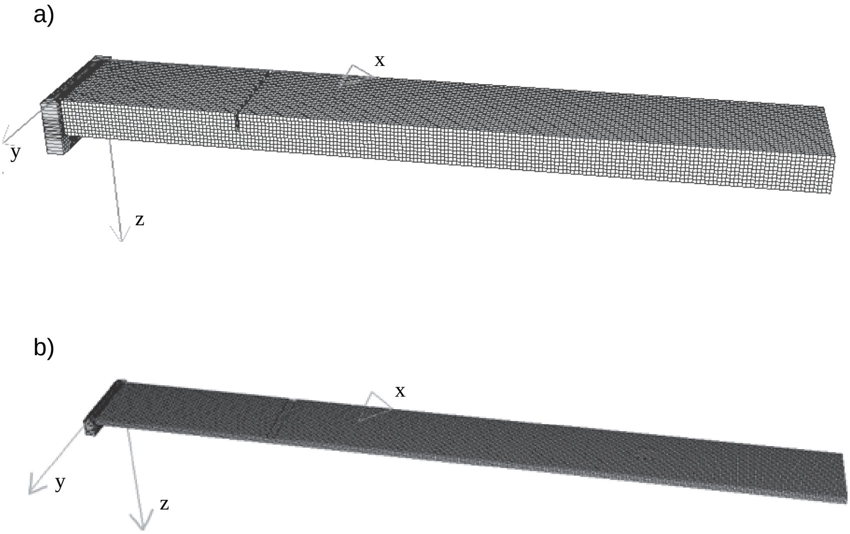

Fig. 4.6. Finite element method model of the cracked beam: a) case 2 from Table 4.1; b) case 12 from Table 4.1

4.1.3. Results of wavelet analysis

The continuous wavelet transform is conducted on the beam static deflection lines assumed as the spatially distributed signals by the Gaussian and Reverse Biorthogonal wavelet families for scales $s = 1 \div 30$. Fig. 4.7 shows the wavelet analysis results for the non-cracked beam (case 1 from Table 4.1) computed from the numerical data, whereas Fig. 4.8 and Fig. 4.9 show the wavelet analysis results for the cracked beam (case 2 from Table 4.1) computed from the numerical data. The wavelet transform for the non-cracked beam is almost flat; however two small peaks are visible. One peak, located near the support, is a result of the border distortion. Another peak indicates the location of the applied static load. The wavelet coefficients computed for the cracked beam have one very distinct maximum. Both the wavelet coefficients and the wavelet transform moduli allow detecting the singularity position. The maximum value grows with the increase of the scale and clearly points to the crack position. The maximum values of the CWT coefficients based on the Gaussian (Fig. 4.8) and Reverse Biorthogonal (Fig. 4.9) wavelets for scale 30 are about 0.01 and 0.006, respectively. Beside maximum due to the defect there exists almost invisible maximum line due to the static force. However, influence of a crack is larger than influence of the applied force and almost makes impossible to detect the location of the force. It is supposed, that in experimental data determination of force location will be impossible due to noise. Figures 4.10 to 4.22 show the wavelet transform modulus computed from the experimental determined deflection lines. A comparison of the action of the Gaussian (gaus4) and Reverse Biorthogonal (rbio5.5) wavelets is performed. The wavelet transform modulus for the non-cracked beam (Fig. 4.10) contains many local maxima that appear due to noise in the measurements. The plots for the case 2 (crack depth of 35% of beam height), shown in Fig. 4.11, have also several maxima lines and the line with the largest value does not correspond to the location of the crack. The presence of the noise in the data masks signals abnormalities that can be detected by the wavelet transform. The results for the case 3 (crack depth of 50% of the beam height) allow localization the crack position (Fig. 4.12). For the scale $s = 30$ the peak of the maximum line can be observed and the value of the CWT modulus reaches 0.02 for the gaus4 wavelet. The rbio5.5 wavelet has just begun to detect crack location at the scale $s = 30$. The crack location can be easily identified in the case 4 (Fig. 4.13), where the crack has an opening of 65% of the beam height. In this case the CWT modulus reaches the values of 0.04 for the gaus4 and 0.026 for the rbio5.5 wavelet.

Next three figures (Fig. 4.14 to Fig. 4.16) provide results for the cases 5, 6 and 7, in which the crack length is twice longer than in the cases 2, 3 and 4. Even though the crack length was increased twice, the results of the case 5 (crack depth of 35% of beam height) do not allow to detect crack position (Fig. 4.14). The CWT modulus for the case 6 (Fig. 4.15), in which the crack has an opening of 35% of the beam height, brings defect identification; however only the gaus4 wavelet allow to detect the crack position. The crack location can be recognized in the case 7 (the crack depth of 65% of the beam height), where both the gaus4 and rbio5.5 wavelets provide proper crack position (Fig. 4.16).

In the next experiment (the cases 8, 9 and 10) the length of the crack was increased three times in comparison with the cases 2, 3 and 4. Expansion of the crack length to 6 mm causes that defect localization was possible in the beam with crack depth of 35% of beam height (the case 8). However, only the gaus4 wavelet allows detection of crack position (Fig. 4.17). The CWT modulus for the cases 9 and 10 (crack depth of 50% and 65% of the beam height) provides proper identification of the crack localization (Fig. 4.18 and Fig. 4.19). Figs. 4.20 to 4.22 show the wavelet transforms for the cases 11, 12 and 13, where the flexible beam was experimentally tested. The results for the beam without a crack (Fig. 4.20) contain many local maxima that appear due to noise in the measurements. In the case 12 (crack depth of 27% of beam height) the localization of damage cannot be determined (Fig. 4.21). In the case 13 (crack depth of 54% of beam height), shown in Fig. 4.22, both considered wavelets precisely indicate the crack position.

Fig. 4.10 and Fig. 4.20 show that the presence of noise in the signal creates fake maxima lines. For both the gaus4 and rbio5.5 wavelets, in the cases 1, 2, 5, 8, 11 and 12 the noisy maxima lines reach the value of about 0.01 and they decrease to the value of about 0.006 for the cases 3, 4, 6, 7, 9, 10 and 13, i.e. for the cases with crack depth of 50% of the beam height or deeper. For the gaus4 wavelet the noisy maxima lines hide the true maxima line for scales up to 15. This scale corresponds to the effective support length of about 98 mm. For the rbio5.5 wavelet, detection of the crack is not possible for scales smaller than 20. The effective support length of the rbio5.5 wavelet corresponding to this scale is about 130 mm.

There are described crack positions recognized from the plots of the wavelet transform modulus on Figs. 4.10 to 4.22. Compatibility of recognized by the wavelets crack centre positions with actual ones amounts from 0% to 6.8%. None of the considered wavelets data based on experiments could locate the force position due to excessive noise.

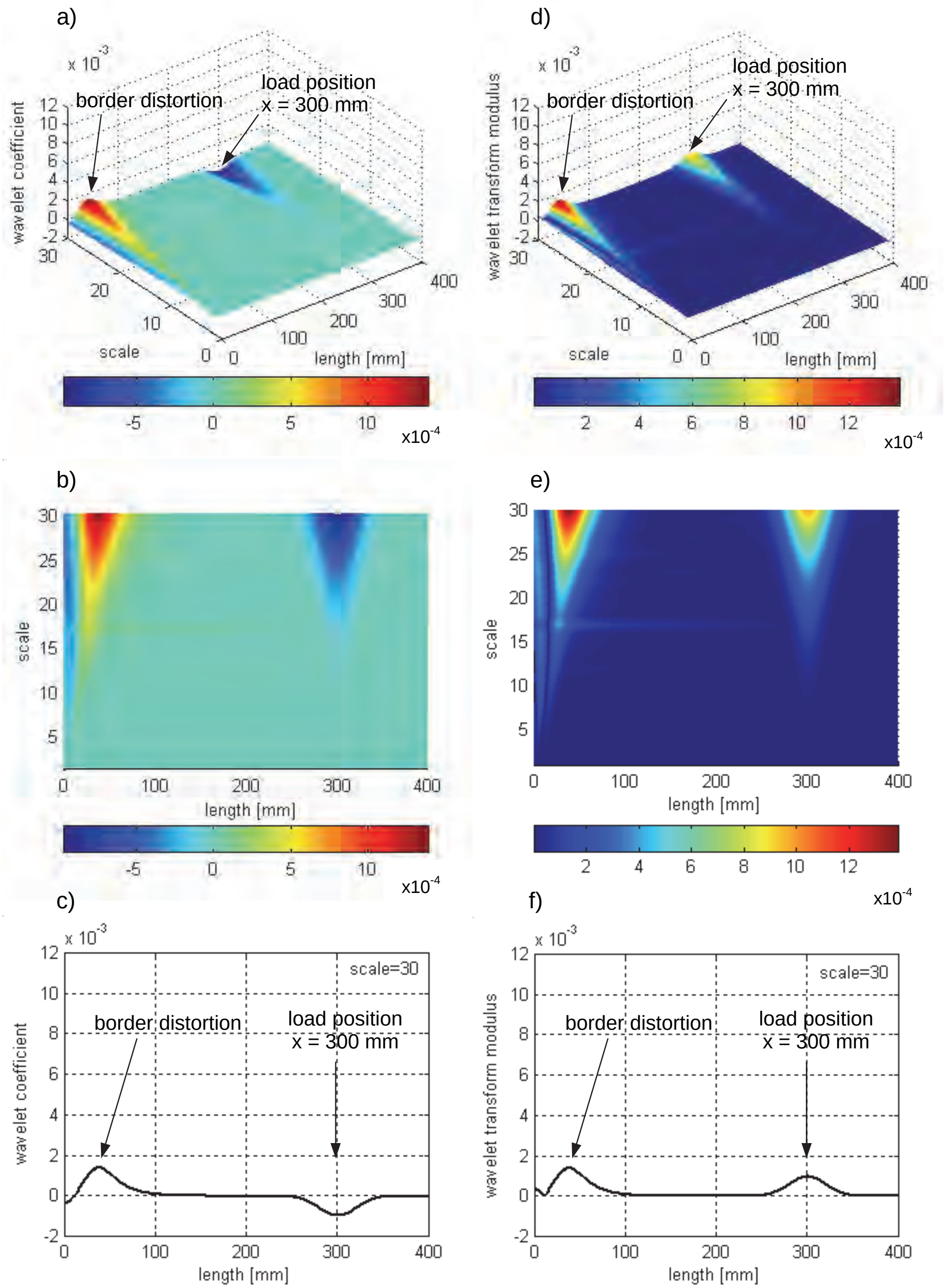

Fig. 4.7. Wavelet analysis of the numerical deflection line of the beam without a crack (case 1 from Table 4.1) performed using gaus4 wavelet: a) wavelet coefficient; b) wavelet coefficient – space-scale plane; c) wavelet coefficient for scale s = 30; d) wavelet transform modulus; e) wavelet transform modulus – space-scale plane; f) wavelet transform modulus for scale s = 30

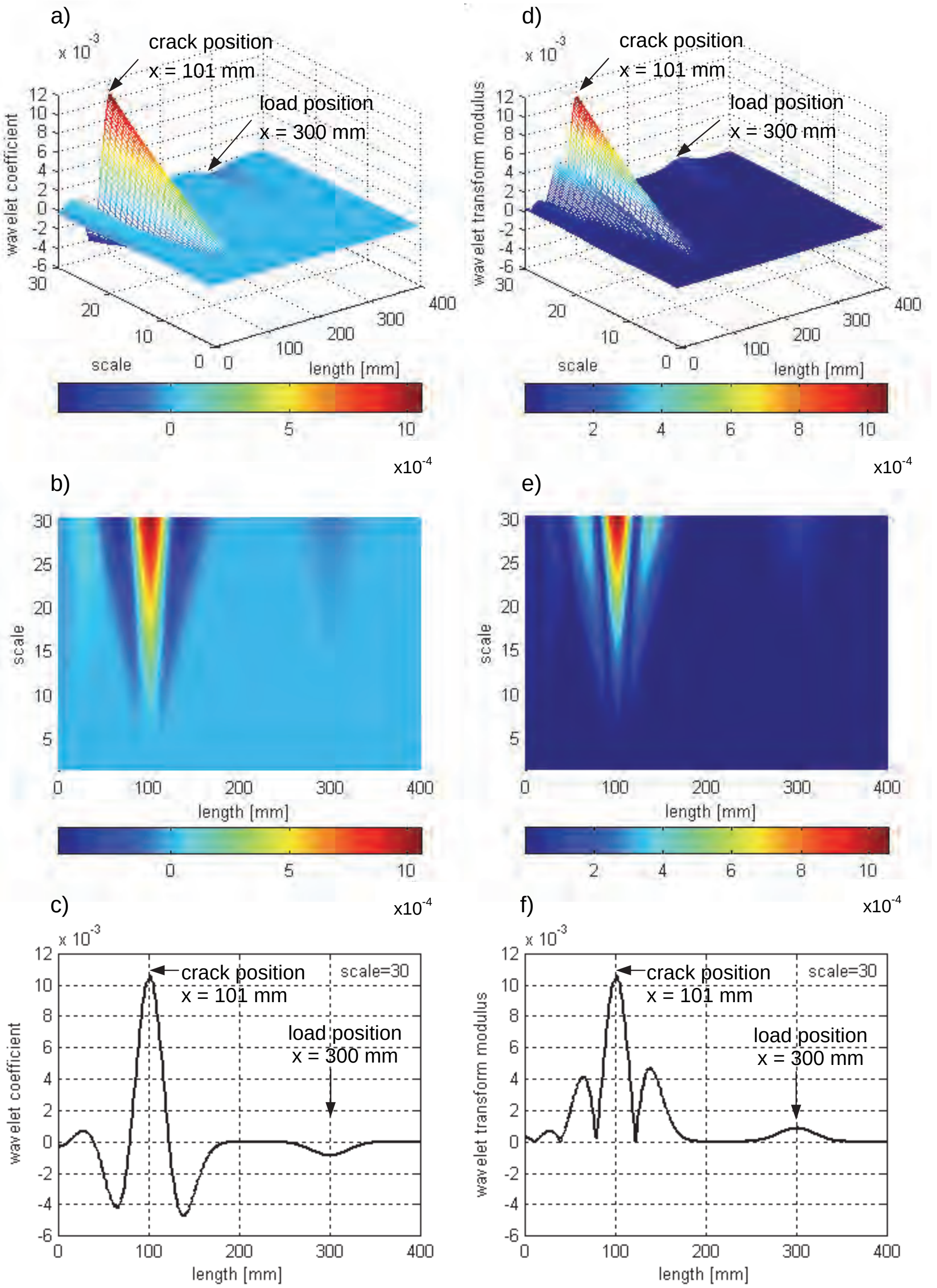

Fig. 4.8. Wavelet analysis of the numerical deflection line of the beam with a crack (case 2 from Table 4.1) performed using gaus4 wavelet: a) wavelet coefficient, b) wavelet coefficient – space-scale plane; c) wavelet coefficient for scale s = 30; d) wavelet transform modulus; e) wavelet transform modulus – space-scale plane; f) wavelet transform modulus for scale s = 30

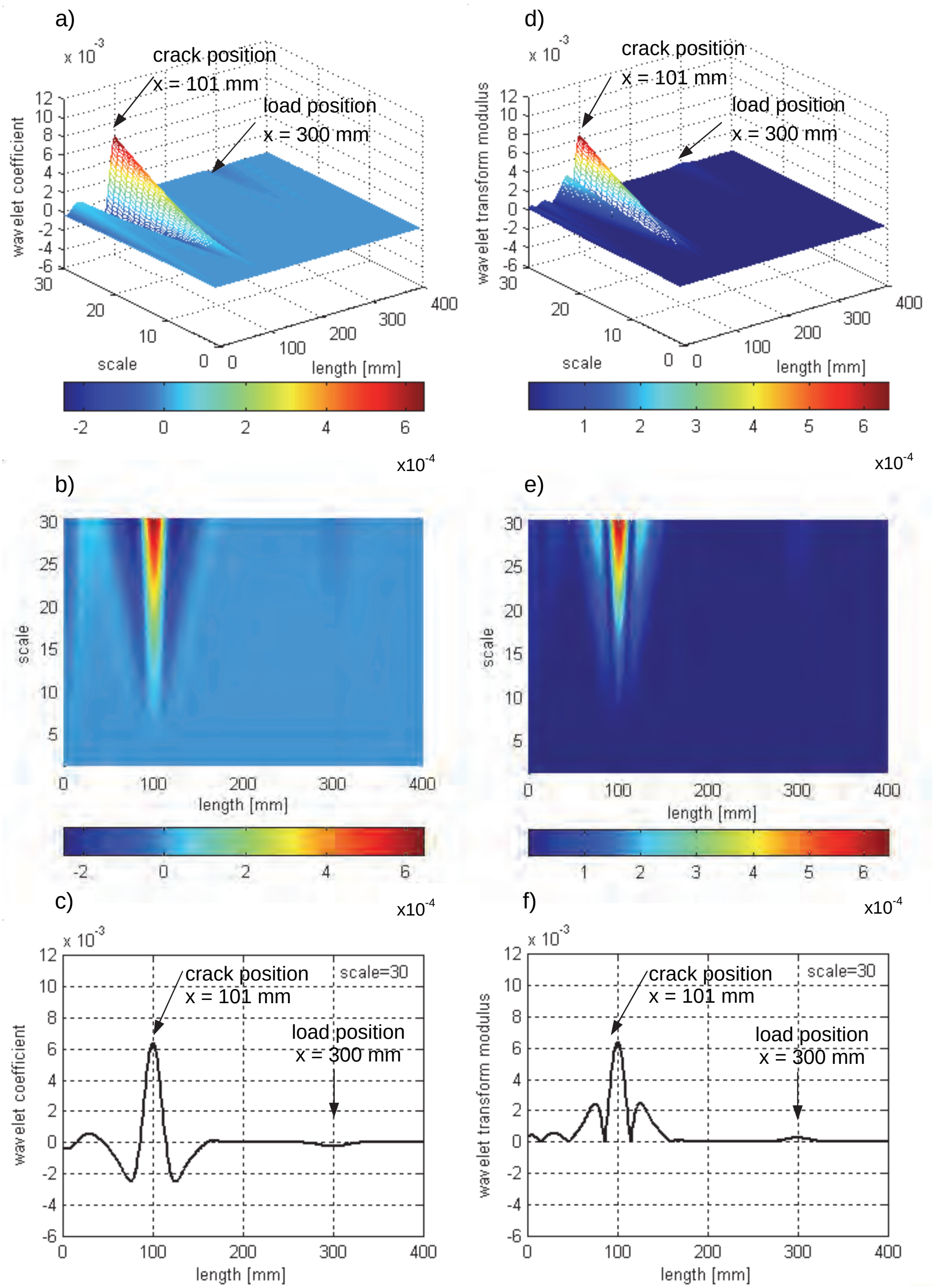

Fig. 4.9. Wavelet analysis of the numerical deflection line of the beam with a crack (case 2 from Table 4.1) performed using rbio5.5 wavelet: a) wavelet coefficient; b) wavelet coefficient – space-scale plane; c) wavelet coefficient for scale s = 30; d) wavelet transform modulus; e) wavelet transform modulus – space-scale plane; f) wavelet transform modulus for scale s = 30

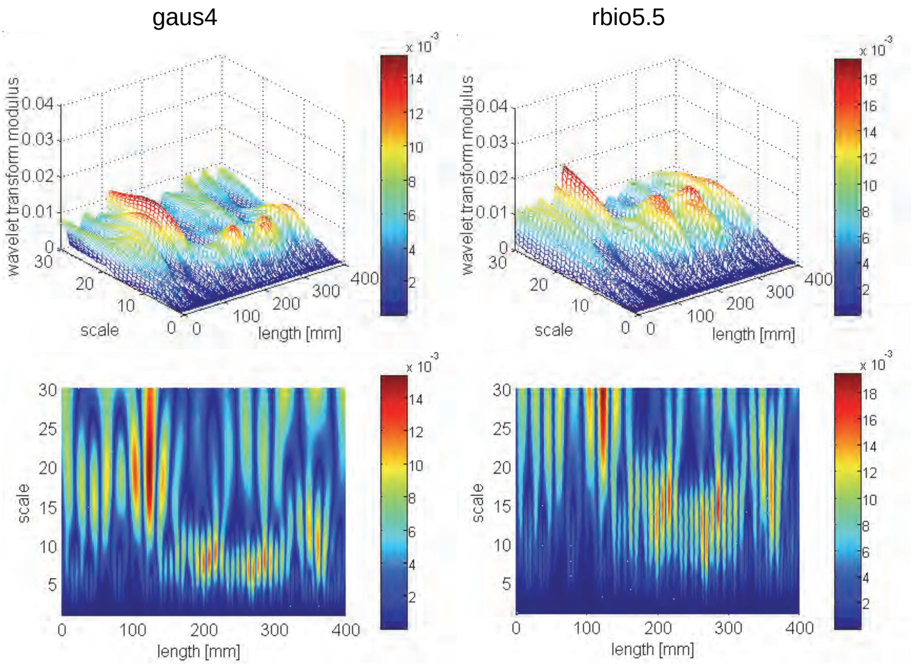

Fig. 4.10. Wavelet transform modulus of experimental deflection line (beam case 1 from Table 4.1)

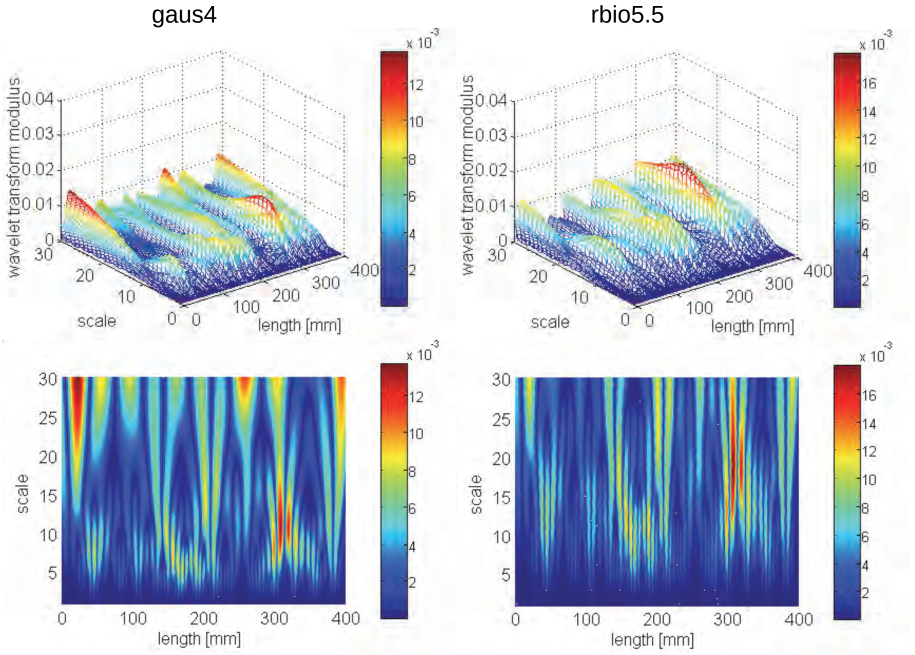

Fig. 4.11. Wavelet transform modulus of experimental deflection line (beam case 2 from Table 4.1)

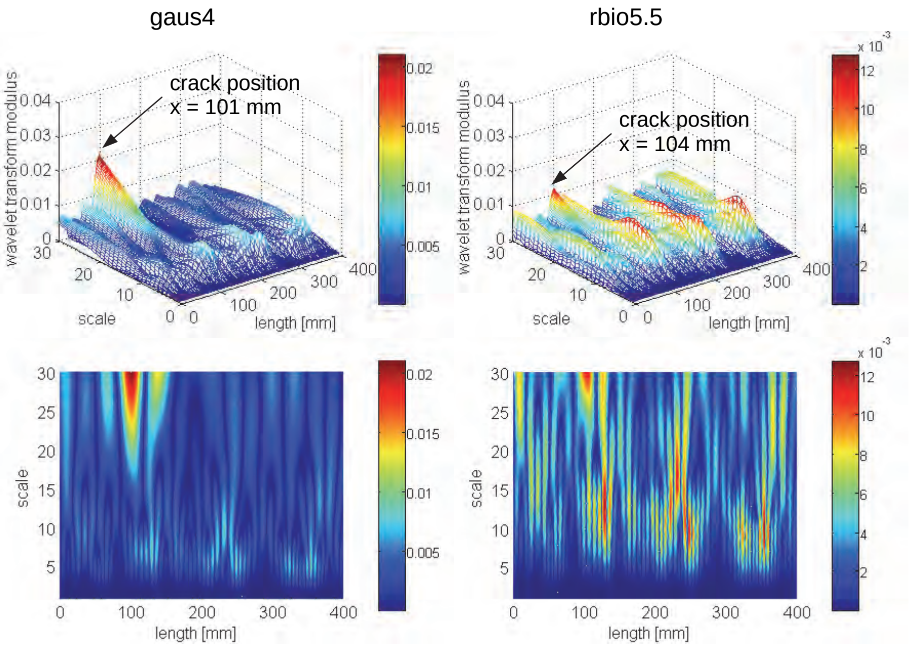

Fig. 4.12. Wavelet transform modulus of experimental deflection line (beam case 3 from Table 4.1)

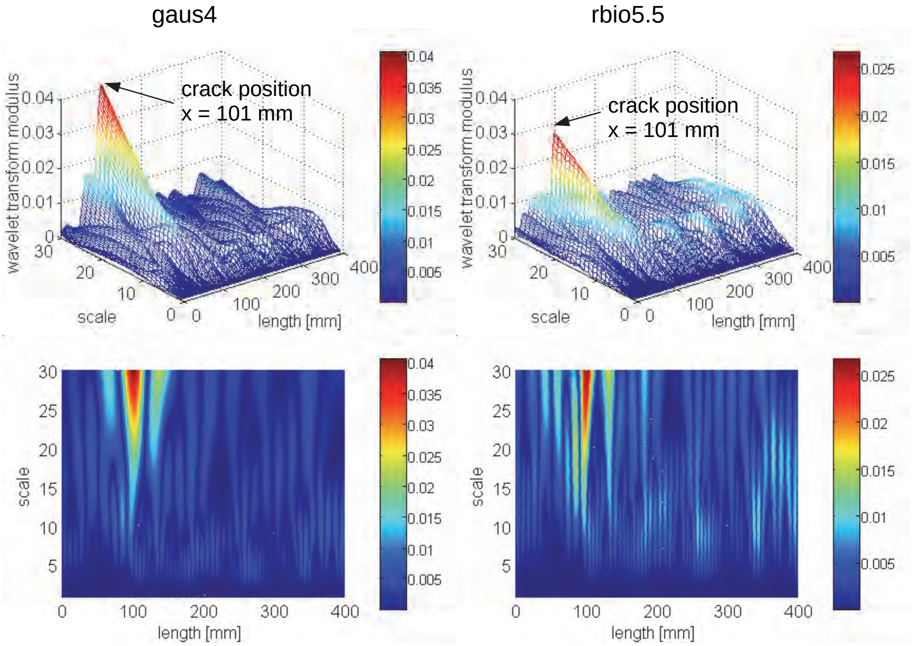

Fig. 4.13. Wavelet transform modulus of experimental deflection line (beam case 4 from Table 4.1)

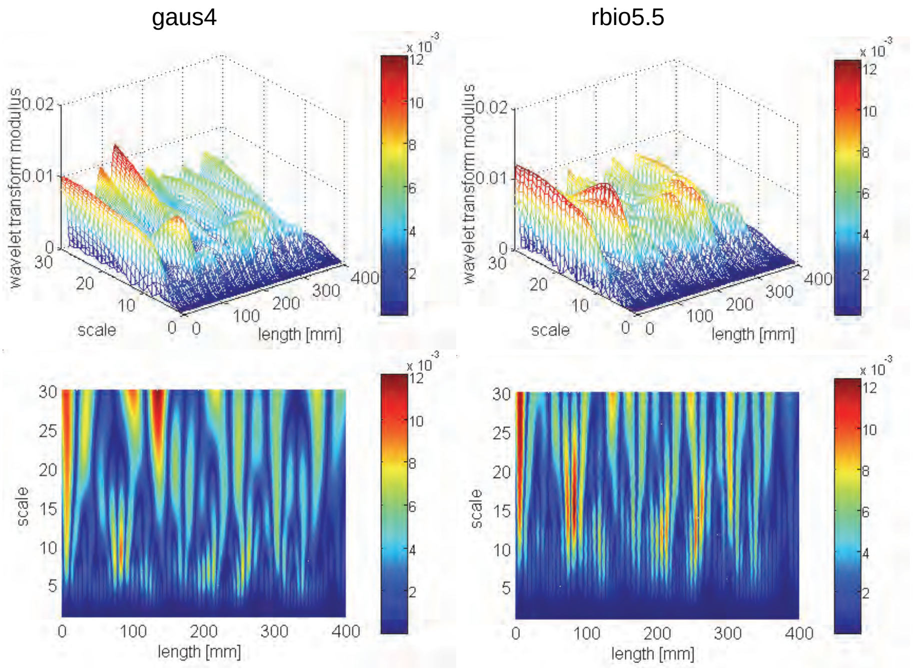

Fig. 4.14. Wavelet transform modulus of experimental deflection line (beam case 5 from Table 4.1)

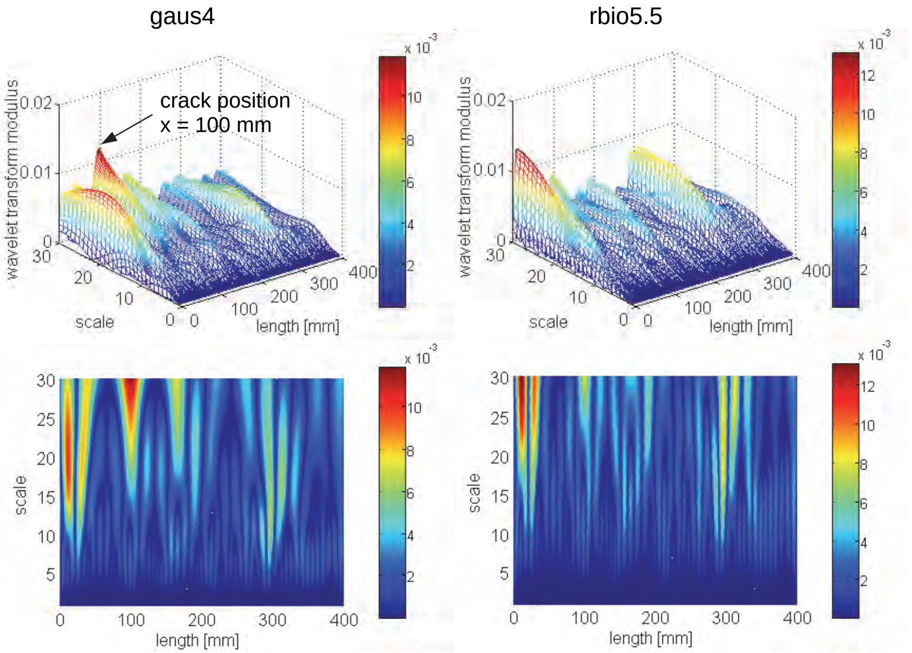

Fig. 4.15. Wavelet transform modulus of experimental deflection line (beam case 6 from Table 4.1)

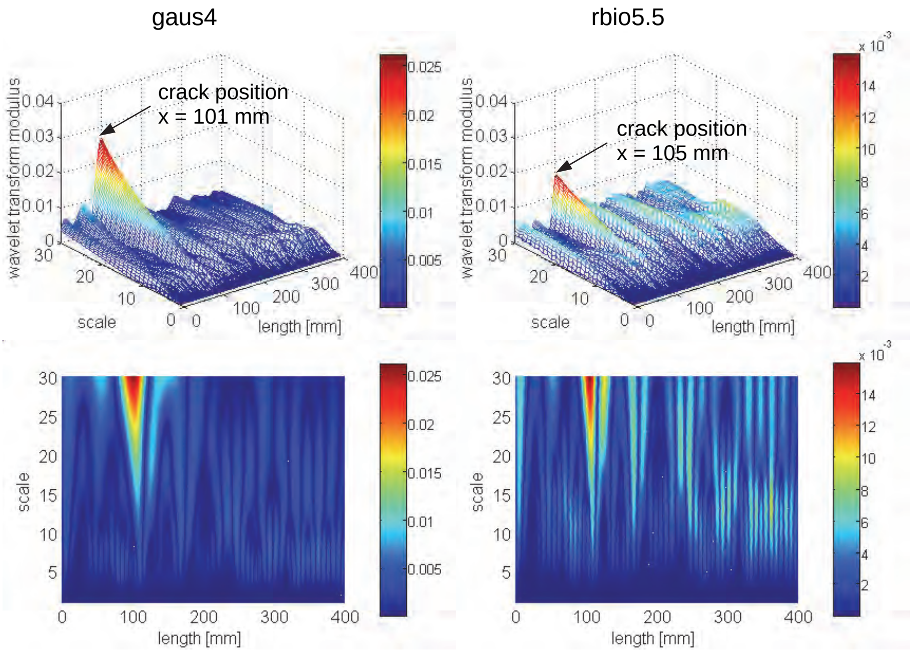

Fig. 4.16. Wavelet transform modulus of experimental deflection line (beam case 7 from Table 4.1)

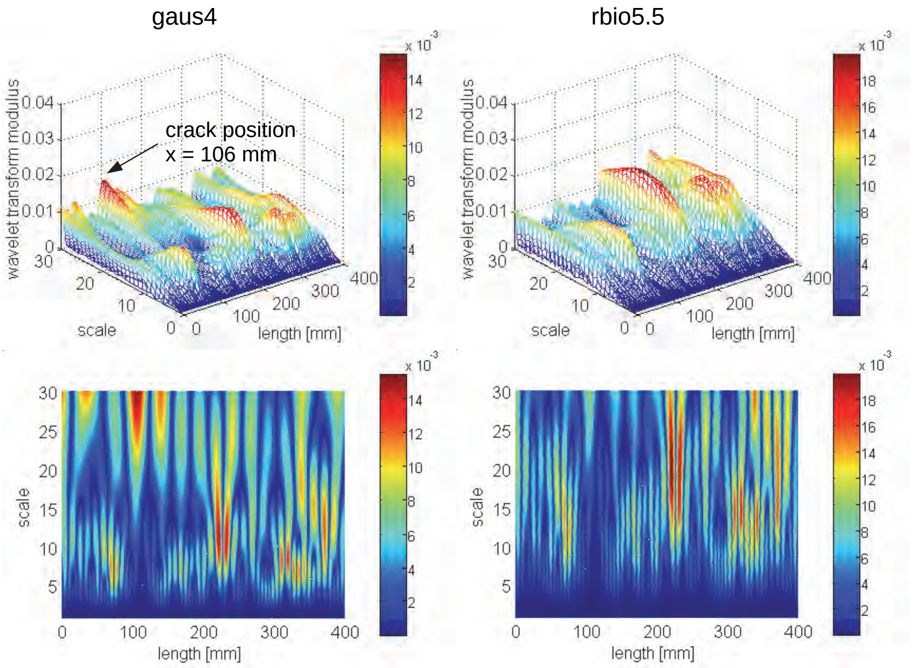

Fig. 4.17. Wavelet transform modulus of experimental deflection line (beam case 8 from Table 4.1)

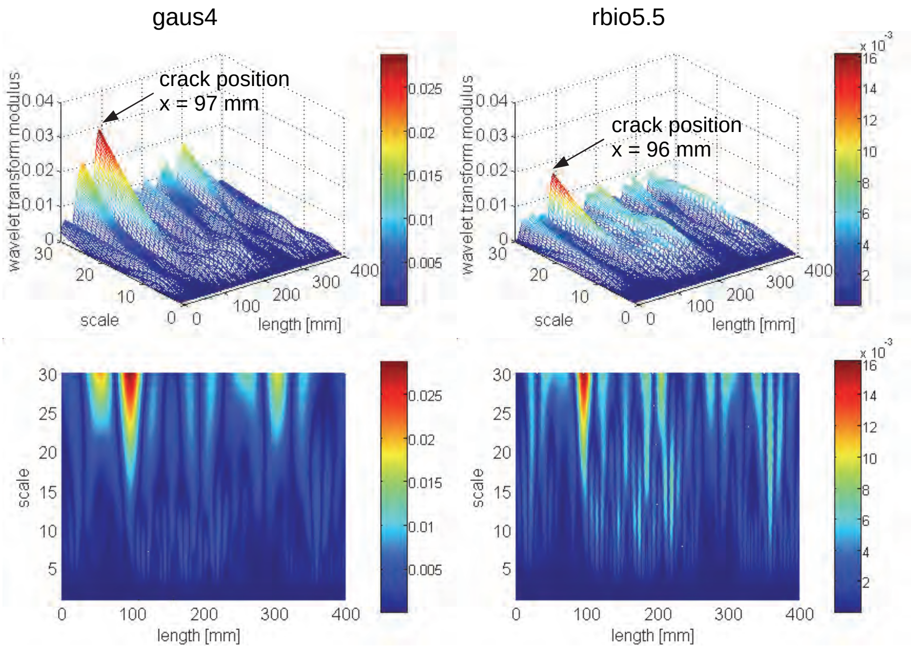

Fig. 4.18. Wavelet transform modulus of experimental deflection line (beam case 9 from Table 4.1)

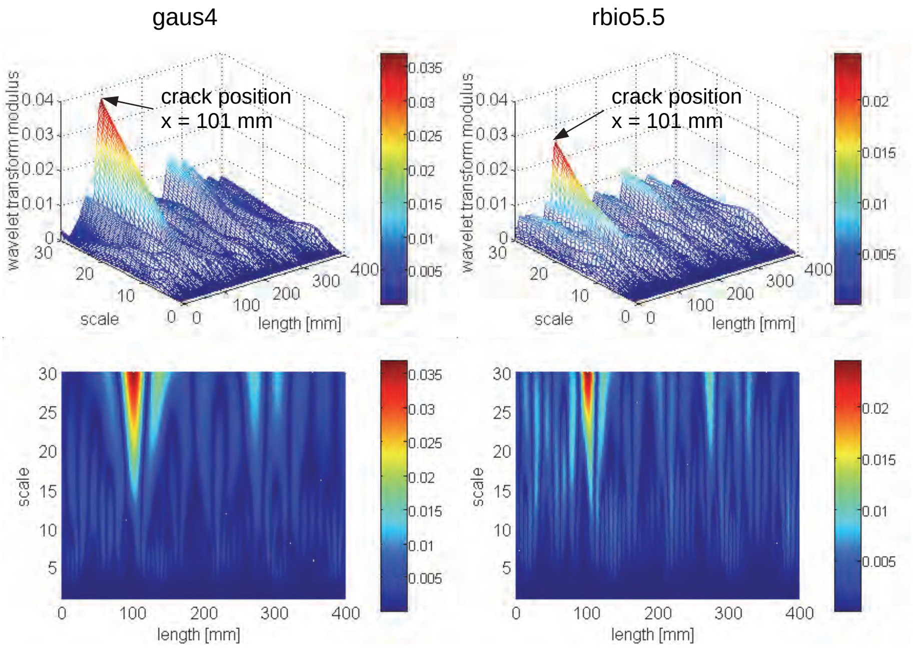

Fig. 4.19. Wavelet transform modulus of experimental deflection line (beam case 10 from Table 4.1)

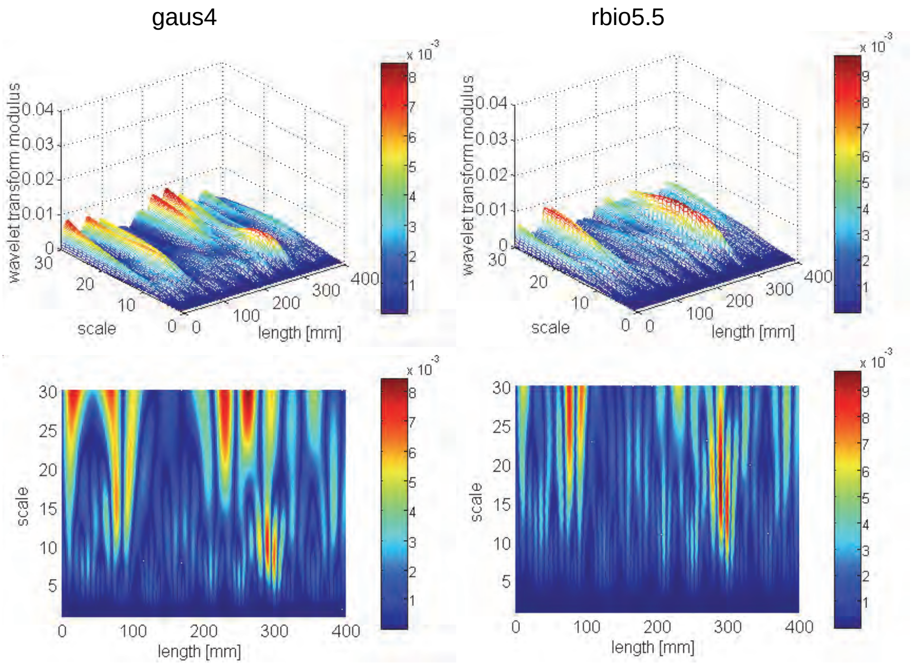

Fig. 4.20. Wavelet transform modulus of experimental deflection line (beam case 11 from Table 4.1)

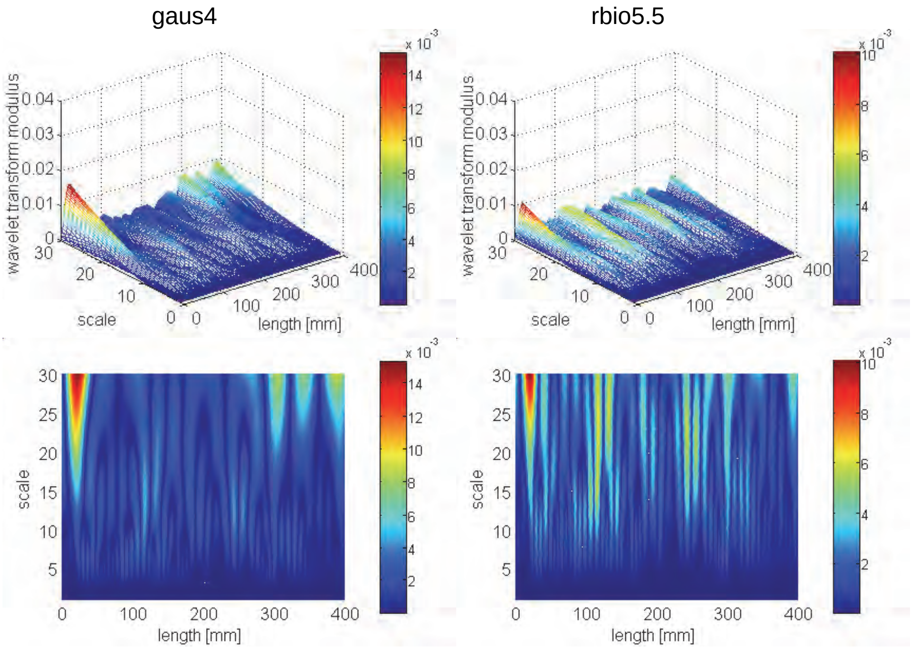

Fig. 4.21. Wavelet transform modulus of experimental deflection line (beam case 12 from Table 4.1)

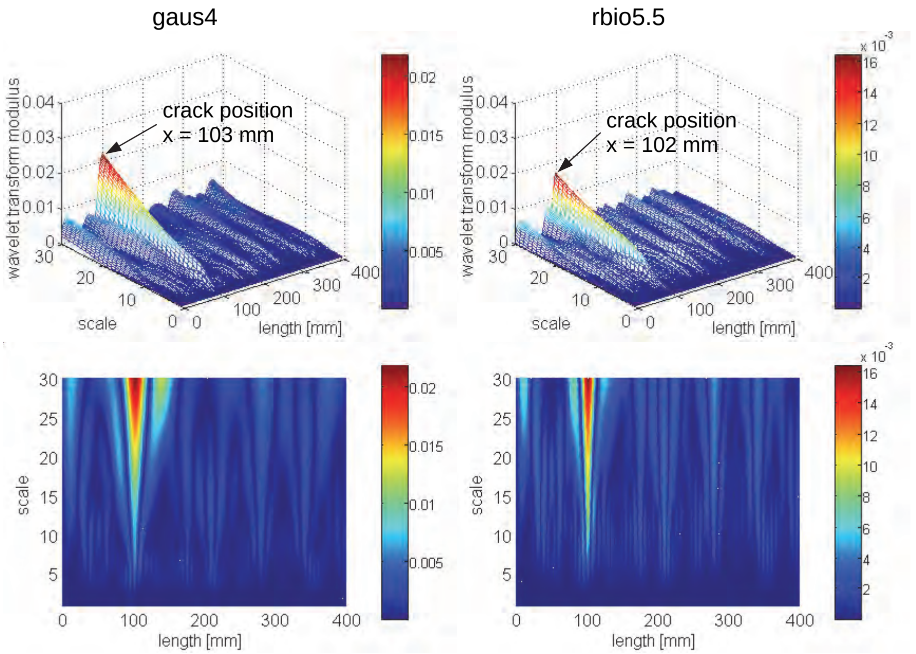

Fig. 4.22. Wavelet transform modulus of experimental deflection line (beam case 13 from Table 4.1)

4.2. Beam – mode shapes

4.2.1. Experimental investigations of beam mode shapes

A cantilever beam is considered. The beam (Fig. 4.23) of length L = 480 mm, height H = 20 mm and width B = 60 mm are made of PMMA. Experimentally determined material properties are: Young's modulus E = 3420 MPa, Poisson ratio $\nu = 0.32$ and mass density is ρ = 1187 kg/m^3. Each beam contains one open crack of length L_r = 2 mm and height a at a distance L_1 = 120 mm from the clamped end. Two beams with different depth of a crack were taken into consideration, namely the beam with the crack of depth 35 % and 45% of the beam height (cases 1 and 2 from Table 4.3).

Table 4.3

Experimental programme

Case no.	Dimensions of beam			Size of crack	
	Length L [mm]	Height H [mm]	Width B [mm]	Length L_r [mm]	Depta a [mm]
1	480	20	60	2	7
2				2	9

The beam was subjected to the dynamic impulse load applied perpendicular to the beam axis. The black dots, plotted in Fig. 4.23, indicate the load application points. The measurements were made using one accelerometer to record the response of the structure. The dynamic impulse load was induced by the modal hammer PCB 086C03 in 48 points on the beam. An accelerometer was attached to the free end of the beam, i.e. at point no. 48. The data were collected by the data acquisition system of Bruel&Kjaer (Pulse type 3650C).

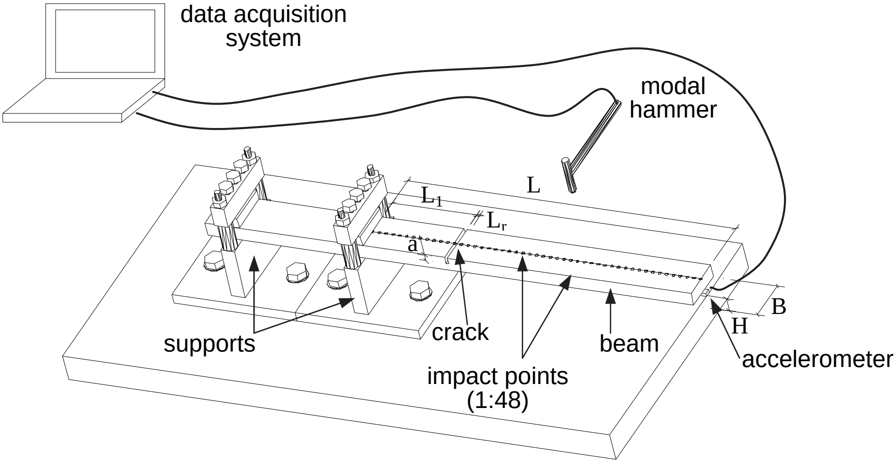

Fig. 4.23. Experimental setup

The mode shapes determination was performed using the complex frequency response function according to the procedure described in Section 3.1.2. In the performed experimental tests, the modal hammer was roving from one point to another point (from 1 to 48), so the measured FRFs determine one of row of the FRF matrix $\mathbf{H}(\omega)$, namely 48th row, because accelerometer was attached to the point no. 48. During impact at each point the acceleration and force signals were measured. Then the signals were transformed into a frequency domain by the Fourier transform. The examples of the time signals $f_{40}(t)$ and $\ddot{x}_{48}(t)$ measured at the point 48 due to impact at the point 40 and corresponding their frequency representations $F_{40}(\omega)$ and $\ddot{X}_{48}(\omega)$ are given in Fig. 4.24. The imaginary part of the frequency response function $H_{48,40}(\omega)$ obtained by impact at the point no. 40 and measurements of response in the point 48 is shown in Fig. 4.25.

The $H_2(\omega)$ estimator was used to the mode shapes estimation. Each acceleration and force measurement was repeated five times and data were five times averaged in the frequency domain. The imaginary part of frequency response function estimator $H_{2(48,40)}(\omega)$ is shown in Fig. 4.26. Experimentally determined first and second mode shapes are presented in Fig. 4.29b and Fig. 4.30b, respectively.

The coherence function is shown in Fig. 4.27. The coherence is close to one, that means low level of noise in the measurements.

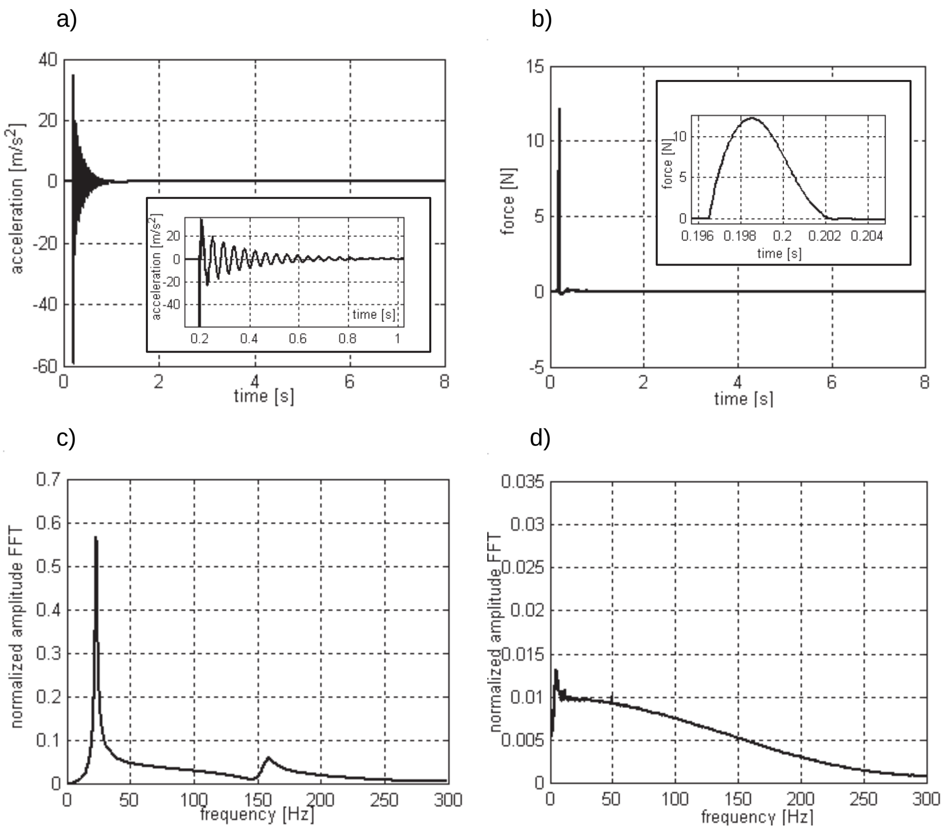

Fig. 4.24. Measured signals for the beam (case 1 from Table 4.3): a) acceleration signal; b) force signal; c) Fourier transform of acceleration; d) Fourier transform of force

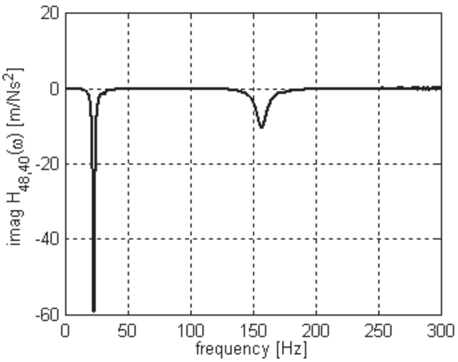

Fig. 4.25. Imaginary part of FRF for the beam (case 1 from Table 4.3)

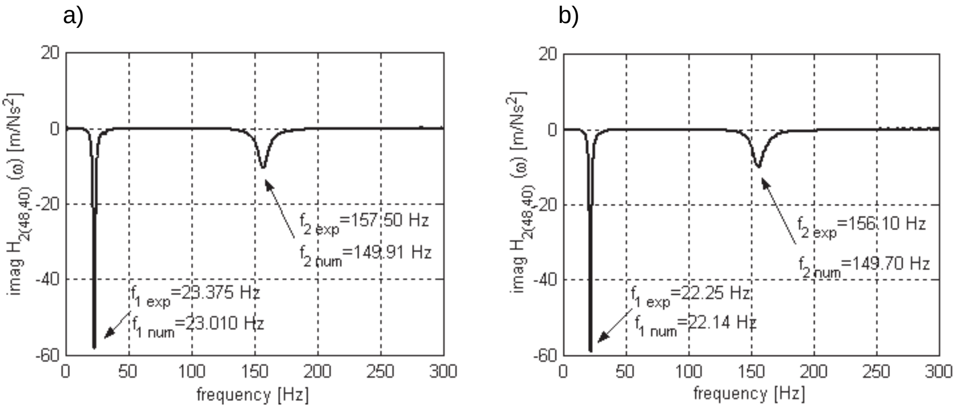

Fig. 4.26. Imaginary part of FRF estimator $H_2(\omega)$ for the beam: a) case 1 from Table 4.3; b) case 2 from Table 4.3

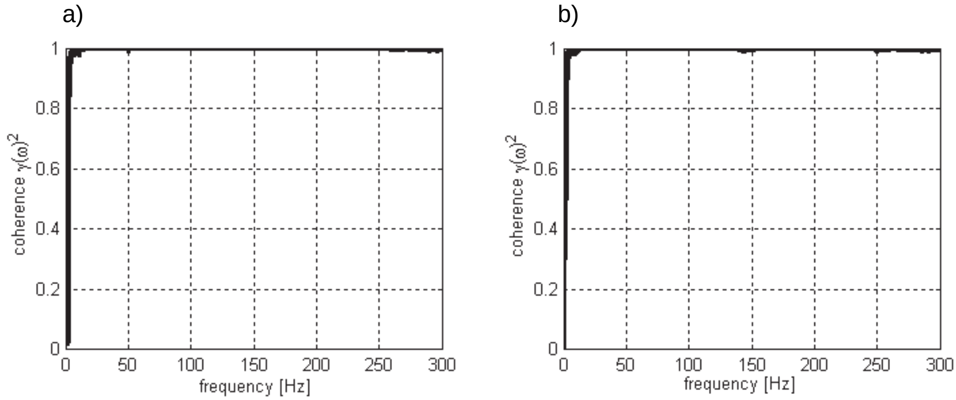

Fig. 4.27. Coherence function: a) beam case 1 from Table 4.3; b) beam case 2 from Table 4.3

4.2.2. Numerical simulations

The mode shapes for the cracked beam were computed by the FEM program SOFiSTiK with the use of a solid six-sided element with eight nodes [30]. Fig. 4.28 presents the applied mesh. The frequencies for the beam with 35% crack are f_1 = 23.010 Hz, f_2 = 149.91 Hz (numerical) and f_1 = 23.375 Hz, f_2 = 157.5Hz (experimental). The frequencies for the beam with 45% crack are found as f_1 = 22.14 Hz, f_2 = 149.70 Hz (numerical) and f_1 = 22.25 Hz, f_2 = 156.1 Hz (experimental).

The numerical and experimental mode shapes are compared in Fig. 4.29 and Fig. 4.30. The differences between the numerical and experimental first mode shape and frequencies are small. However, there is a noticeable difference between the second numerical and experimental mode shape. The beam experimental first mode shapes are slightly underestimated for the region near the support. These discrepancies are due to the difficulties in obtaining an ideal fixed support of the beam. The second mode shape is more underestimated than the first one due to the boundaries condition.

The mode shapes of the beam were measured with the sampling distance of 10 mm and calculated with the sampling distance of 2 mm, therefore a piecewise cubic spline data interpolation was used to decrease the sampling distance to 1 mm. After interpolation each mode shape line was normalized to 1.

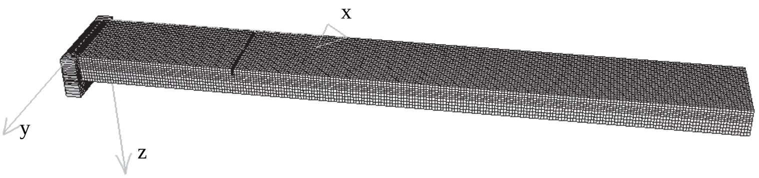

Fig. 4.28. Finite element method model of the cracked beam (case 1 from Table 4.3)

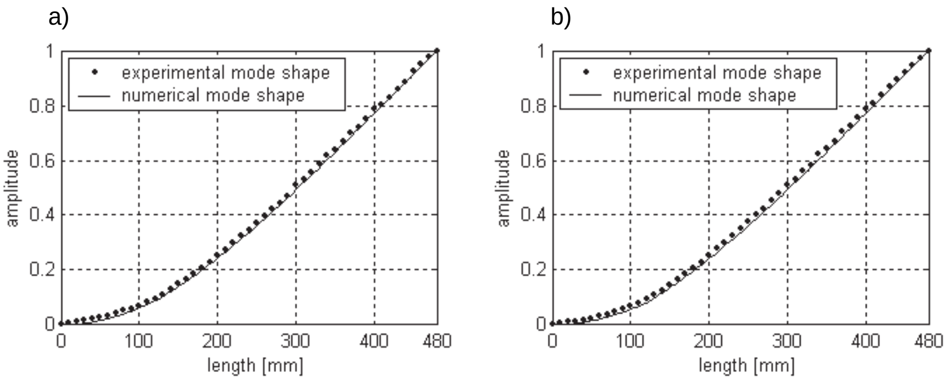

Fig. 4.29. Experimental and numerical first mode shapes: a) case 1 from Table 4.3;
b) case 2 from Table 4.3

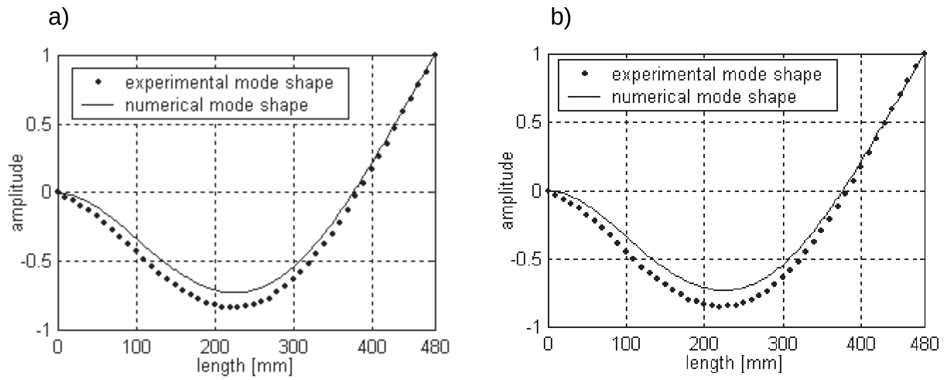

Fig. 4.30. Experimental and numerical second mode shapes: a) case 1 from Table 4.3;
b) case 2 from Table 4.3

4.2.3. Results of wavelet analysis

The wavelet analysis is conducted on the beam first and second mode shapes assumed as a spatially distributed signal by the Gaussian wavelets. The wavelet analysis of the first mode shape is performed using the gaus4 wavelet because the first mode shape is similar to the polynomial of 4th order. The second mode shape is analyzed using both the gaus4 and gaus6 wavelets because the second mode shape can be described by the polynomial of order higher than 4.

The wavelet transform modulus computed from the first mode shape numerical data is shown in Fig. 4.31 and Fig. 4.32 for the cases 1 and 2, respectively. One-dimensional continuous wavelet transforms of the numerical mode shapes are performed for the scales $s = 1 \div 30$. The modulus maximum value grows with the increase of the scale and clearly points to the crack position at 121 mm from the clamped end. The wavelet transform modulus results based on the experimental data (Fig. 4.33 and Fig. 4.34) have additional maxima lines resulting from the measurement noise. Nevertheless, the dominant maxima lines, corresponding to the crack positions, increases monotonically and for larger scales they achieve the largest values. The crack location can be easy recognized in the case 1 (crack depth of 35% of beam height) as well as the case 2 (crack depth of 45% of beam height). The positions of defects determined by the wavelet analysis are 132 mm and 136 mm for the case 1 and 2, respectively. A compatibility of recognized by wavelets the crack centre positions with actual ones amounts from 9.1% to 12.4%. The wavelet transforms of the experimental mode shapes require larger values of scales than the wavelet transforms of the numerical mode shapes. In the case of experimental data the crack positions cannot be detected for scales up to about 40 whereas in the case of the numerical data crack positions can be determined from the scale $s = 2$.

The wavelet transform modulus of the second numerical mode shape is presented in Fig. 4.35 and Fig. 4.36, for the cases 1 and 2, respectively. The Gaussian wavelet with 4 vanishing moments provides some non-zero coefficients besides the defect location. The Gaussian wavelet with 6 vanishing moments provides maximum only in the defect location. However, the maximum value of wavelet transform calculated using the gaus4 is larger than the maximum value calculated using the gaus6 wavelet. Therefore, using the wavelet with higher number of vanishing moments results in decreasing of the maximum value of the wavelet transform. The results based on the experimental second mode shapes (Fig. 4.37 and Fig. 4.38) contain some noise, however detection of the cracks is possible. Both the gaus4 and gaus6 wavelets clearly allow to indicate the defect position. In the case 1, the position of the crack determined by the wavelet analysis is 129 mm regardless of the wavelet applied. In the case 2 crack location is found to be 117 and 116 mm using the gaus4 and gaus6, respectively. A compatibility of recognized by the wavelets the crack centre positions with actual ones amounts from 3.3% to 6.6%. As in the case of the numerical data, in the experimental data the maximum value of the wavelet transform decreases with the increase of the number of vanishing moments so using the wavelet with higher number of vanishing moments than essential is not appropriate.

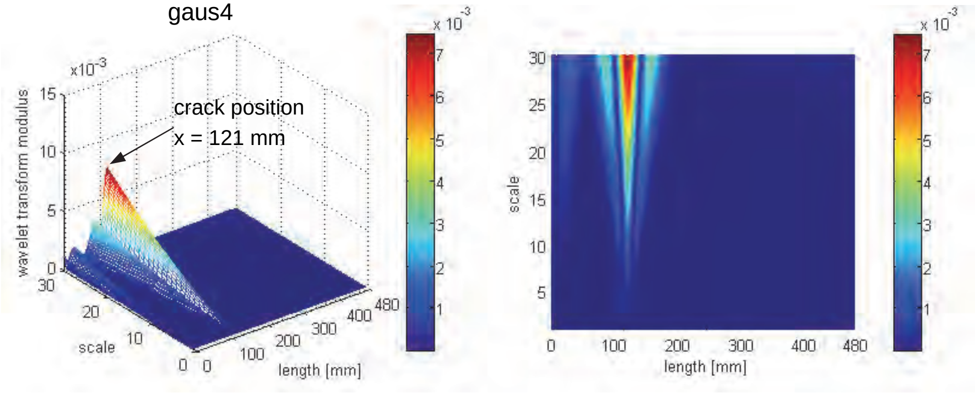

Fig. 4.31. Wavelet transform modulus of numerical first mode shape (case 1 from Table 4.3)

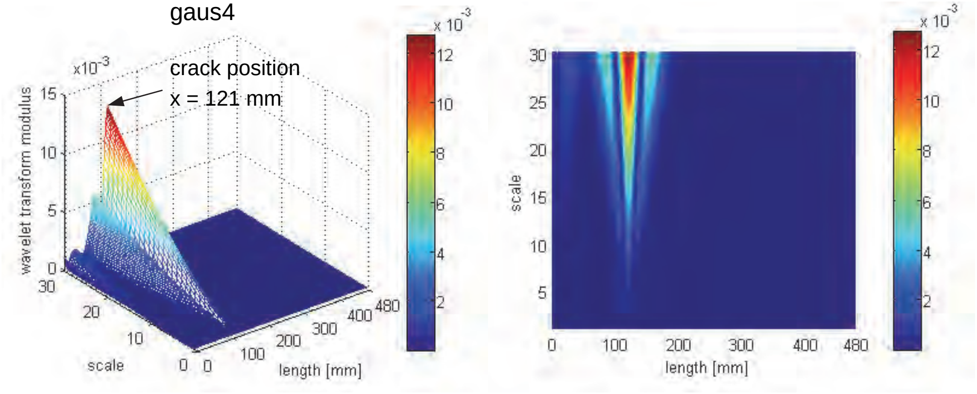

Fig. 4.32. Wavelet transform modulus of numerical first mode shape (case 2 from Table 4.3)

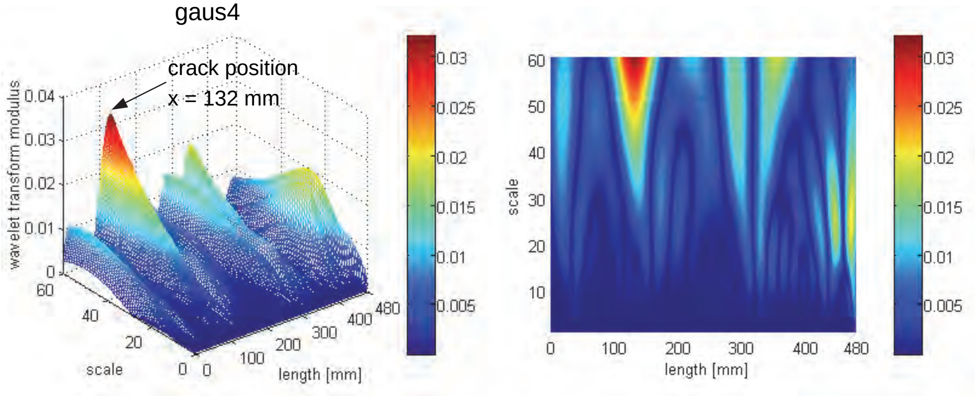

Fig. 4.33. Wavelet transform modulus of experimental first mode shape (case 1 from Table 4.3)

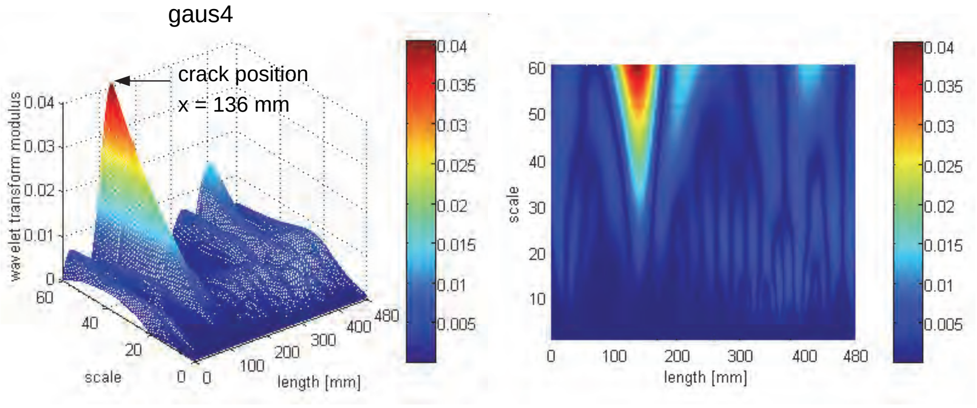

Fig. 4.34. Wavelet transform modulus of experimental first mode shape (case 2 from Table 4.3)

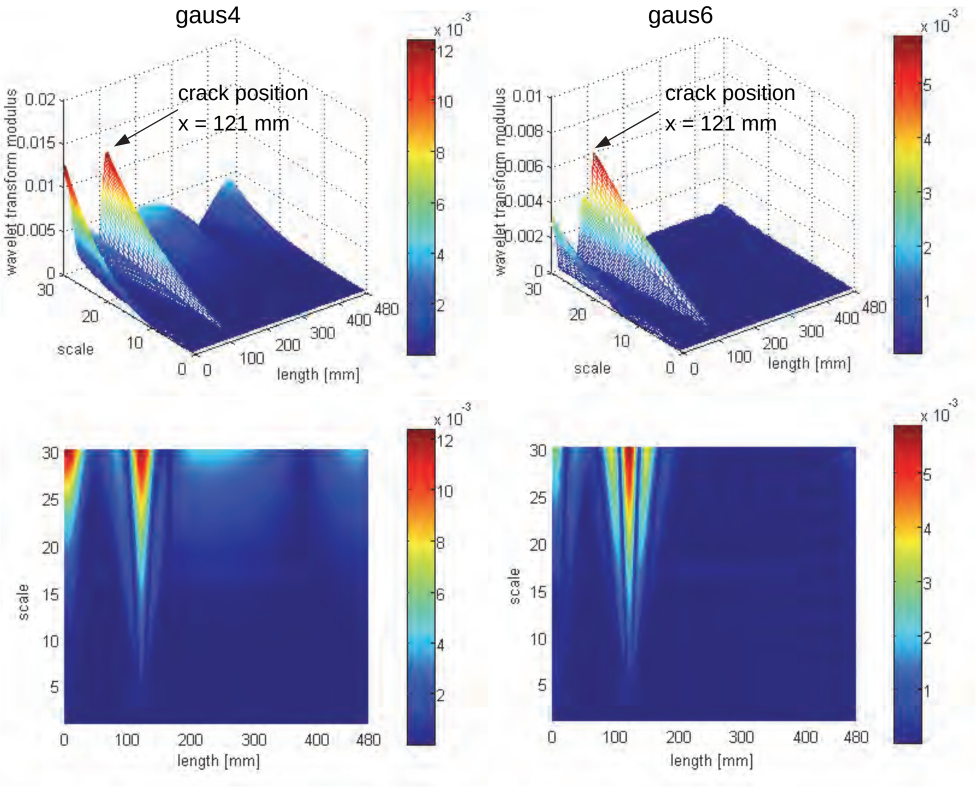

Fig. 4.35. Wavelet transform modulus of numerical second mode shape (case 1 from Table 4.3)

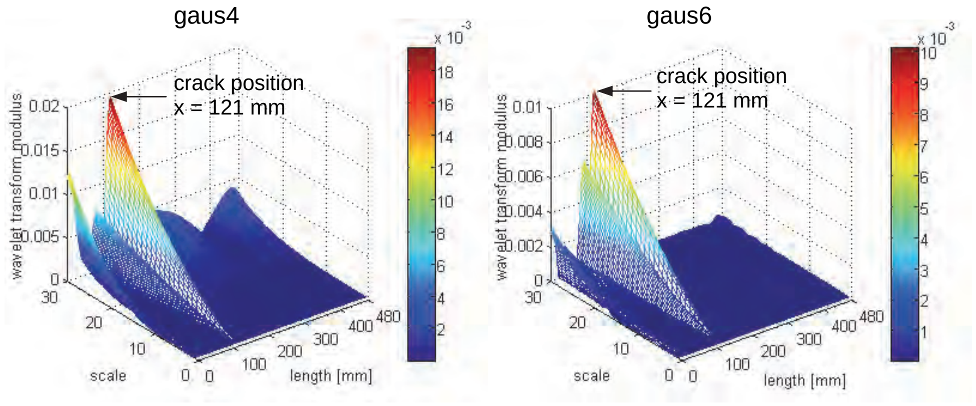

Fig. 4.36. Wavelet transform modulus of numerical second mode shape (case 2 from Table 4.3)

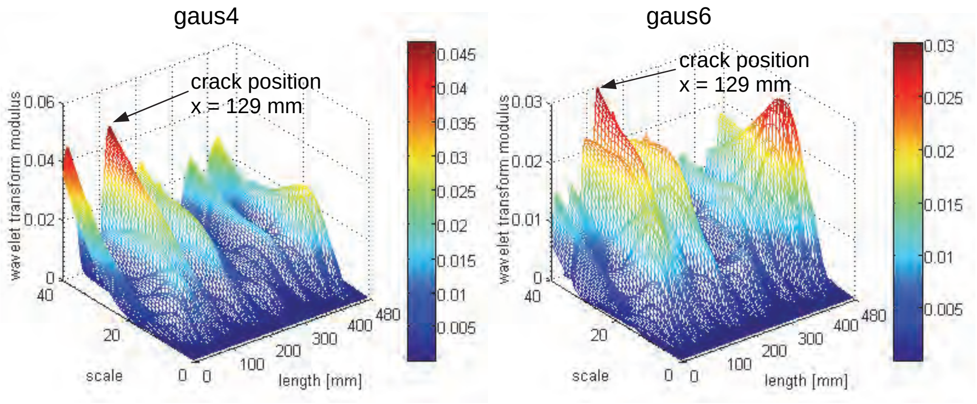

Fig. 4.37. Wavelet transform modulus of experimental second mode shape (case 1 from Table 4.3)

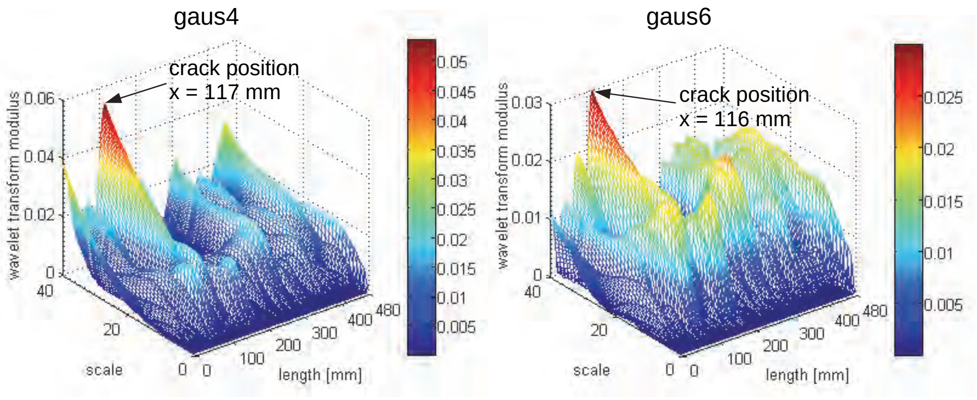

Fig. 4.38. Wavelet transform modulus of experimental second mode shape (case 2 from Table 4.3)

4.3. Plate – mode shapes

4.3.1. Experimental investigations of plate mode shapes

A steel plate with the length of L = 560 mm, width of B = 480 mm and height of H = 2 mm is considered. The experimentally determined properties of the material are: Young's modulus E = 192 G Pa, Poisson ratio ν = 0.25 and mass density ρ = 7430 kg/m^3. The plate shown in Fig. 4.39 contains a rectangular defect of length L_r = 80 mm, width B_r = 80 mm and depth of a = 0.5 mm. The distance from the defect left-down corner to the plate left-down corner in the horizontal and vertical direction are: L_1 = 200 mm and B_1 = 200 mm, respectively. The area of the flaw amounts to 2.4% of the plate area and the depth of the flaw is 25% of the plate height.

The plate was subjected to a dynamic impulse load applied by the modal hammer PCB 086C03 at the selected points. The total number of the considered measurement points was 143. The points of load application are signed in Fig. 4.40 by black dots. The vibration responses were recorded using one accelerometer attached to the plate at point no. 74 on the bottom plate surface. The data acquisition system Pulse type 3650C was used to data collecting.

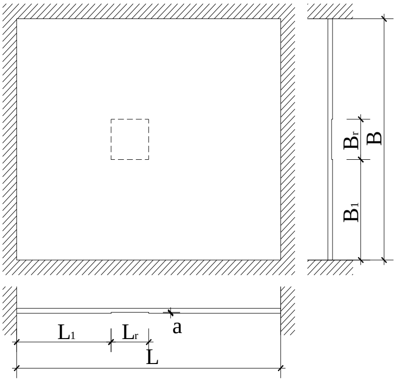

Fig. 4.39. Geometry of considered plate

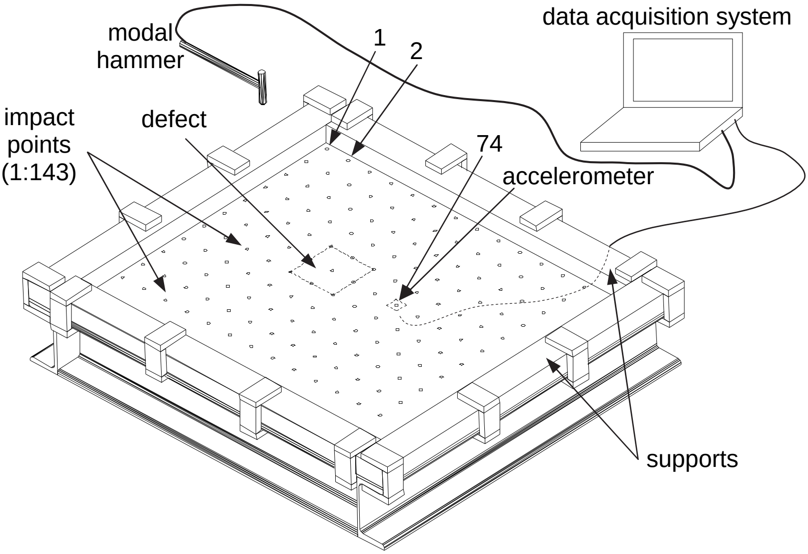

Fig. 4.40. Experimental setup

To determine the mode shapes estimation, the procedure using the complex frequency response function (FRF) was applied (see Section 3.1.2). At each point, from 1 to 143 force signals were measured. The responses were recorded at point no. 74, so 74th row of the FRF matrix was measured. All force and acceleration signals were transformed into a frequency domain by the fast Fourier transform. Fig. 4.41 shows the time signals $f_{60}(t)$ and $\ddot{x}_{74}(t)$ measured at the point no. 74 due to force applied at the point no. 60 and corresponding their frequency representations $F_{60}(\omega)$ and $\ddot{X}_{74}(\omega)$, whereas Fig. 4.42 presents the imaginary part of the frequency response function $H_{74,60}(\omega)$ for the plate obtained by impact at the point 60 and the measurement of the response at the point no. 74.

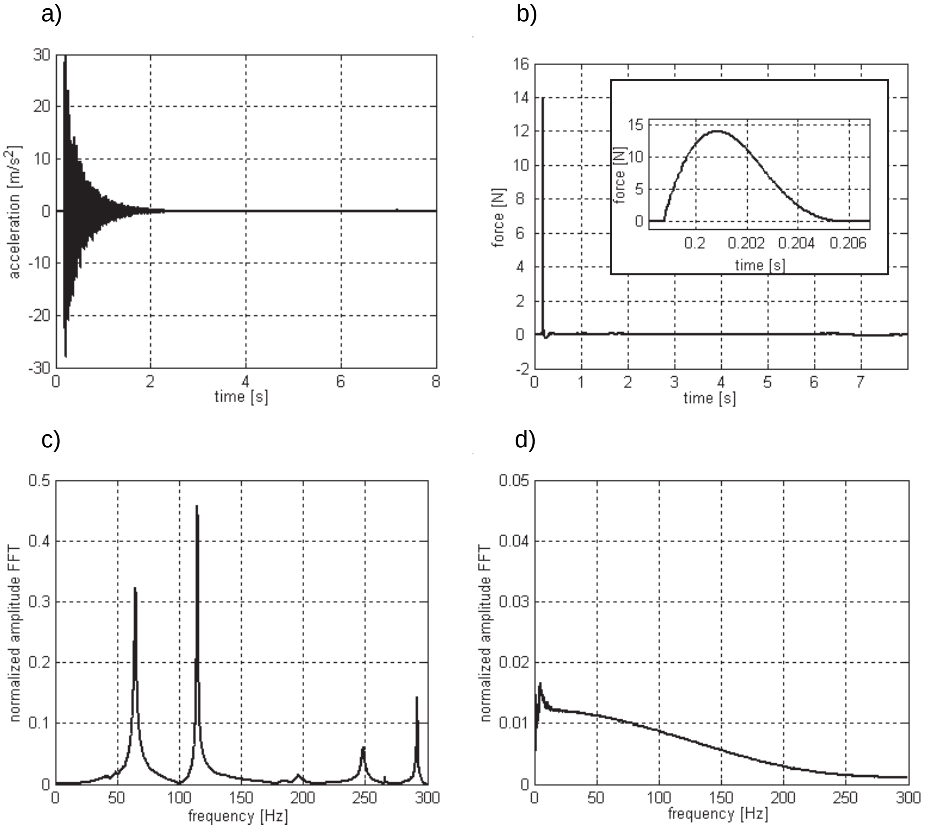

Fig. 4.41. Measured signals for the plate: a) acceleration signal; b) force signal; c) Fourier transform of acceleration; d) Fourier transform of force

Each acceleration and force measurement was repeated five times and the data were five times averaged in the frequency domain. Then the $H_2(\omega)$ estimator was used to the mode shape estimation. In Fig. 4.43 the imaginary part of the FRF estimator $H_{2(74,60)}(\omega)$ is presented. The experimentally determined fundamental mode shape is shown in Fig. 4.46b.

The coherence function, shown in Fig. 4.44, is close to one but at several points it reaches values smaller than. It means weak relationship between the input and the output due to noise in the output or due to non-linear behaviour at the resonance point. However, the coherence near the first frequency f_1 = 64.875 Hz is close to one.

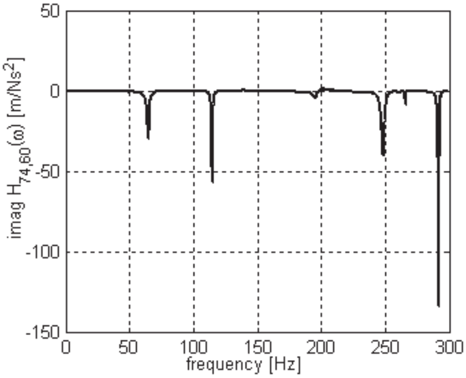

Fig. 4.42. Imaginary part of FRF for the plate

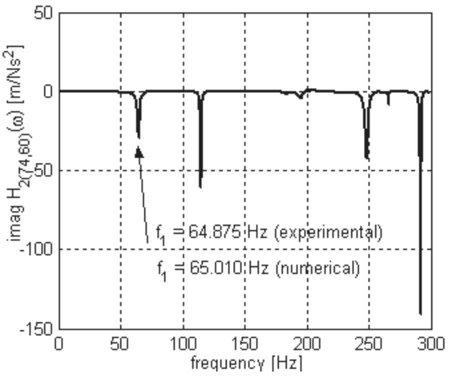

Fig. 4.43. Imaginary part of FRF estimator $H_2(\omega)$

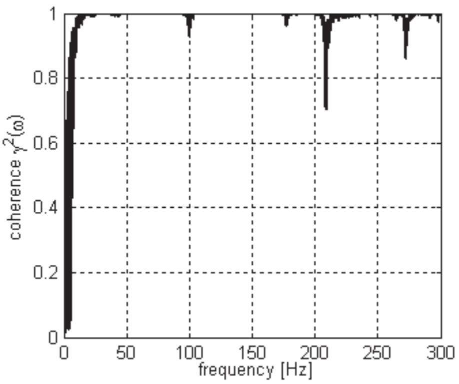

Fig. 4.44. Coherence function

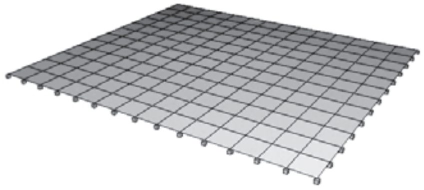

Fig. 4.45. FEM model of the plate

4.3.2. Numerical simulations

The plate mode shapes were computed by FEM program SOFiSTiK using the mesh of 40×40 mm plane elements (Fig. 4.45). The plane element in SOFiSTiK (quad) [30] is a general quadrilateral element with four nodes.

The first frequency for the plate obtained in the numerical simulations was f_1 = 65.100 Hz and it is very similar to the frequency obtained experimentally f_1 = 64.875 Hz. The first experimental and numerical mode shapes of the plate (Fig. 4.46) have to be presented separately since the obtained results are almost identical. Since the mode shape of the plate was measured and calculated with sampling distance of 40 mm a piecewise cubic spline data interpolation was used to decrease sampling distance to 1 mm. Then the mode shape was normalized to 1.

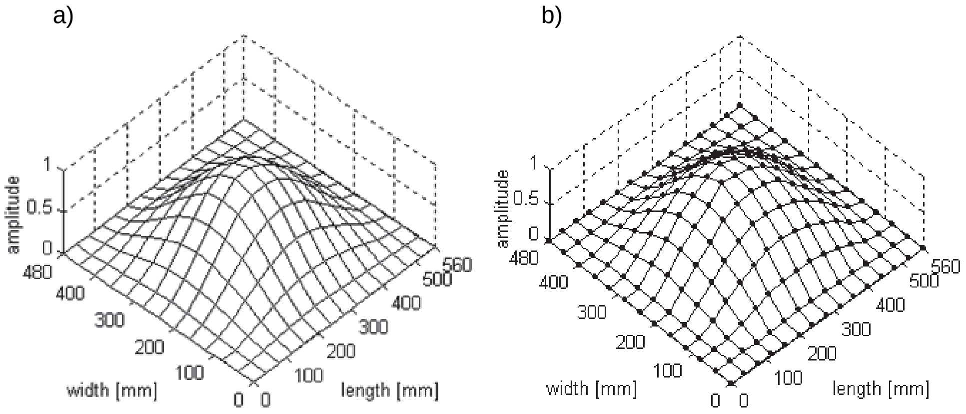

Fig. 4.46. Fundamental mode shape for the plate: a) numerical; b) experimental

4.3.3. Results of wavelet analysis

The results of the wavelet transform of the plate fundamental mode shape are the wavelet coefficients for different scales. A presence of the defect is detected by a sudden change in a spatial variation of the transformed response. The horizontal coefficients $W^1 f(u,v,s)$, the vertical coefficients $W^2 f(u,v,s)$ and the wavelet transform moduli $Mf(u,v,s)$ for the numerical and experimental data are given in Fig. 4.47 and Fig. 4.48, respectively. The results presented in these graphs are performed at the scale $s = 40$. In the case of damage detection application, the $W^1 f(u,v,s)$ wavelet component indicates the signal abnormalities along the width of the plate, i.e., along the y coordinate. This effect appeared as the detecting action is performed by the function ψ along y coordinate. The $W^2 f(u,v,s)$ component indicates the abnormalities along the length of the plate. Although the coefficient $W^1 f(u,v,s)$ presented in the first row of the Fig. 4.47 is computed for the two-dimensional approach, the coefficient lines along the y coordinate resemble the shape of the wavelet function $\psi(y)$. By analogy, the lines of the vertical coefficient along x coordinate resemble the $\psi(x)$ function. The distribution of the horizontal and vertical coefficients in x and y directions is similar, what suggests that the shape of the defect has similar dimensions in both directions. The third row of the Fig. 4.47 presents the modulus of the 2D wavelet coefficients and the visible cross, on the top view plot, combines the information stored in the $W^1 f(u,v,s)$ and $W^1 f(u,v,s)$ wavelet transform components.

The peak in the modulus $Mf(u,v,s)$ based on the numerical (Fig. 4.47) as well as $Mf(u,v,s)$ based on the experimental data (Fig. 4.48) clearly indicates the defect position and its shape. In the case of the experimental data, the presence of some noise does not mask the signal abnormalities and the position and the size of the crack can be estimated. The local maximum of $Mf(u,v,s)$ based on the experimental data is in the distance of $x = 240$ mm and $y = 243$ mm from the left-down plate corner. The real location of defect is $x = 240$ mm and $y = 240$ mm from the left-down plate corner and it is in agreement with the maximum from the numerical data. The maximum value of the experimental wavelet transform modulus $Mf(u,v,s)$ is about four times larger than the corresponding numerical modulus.

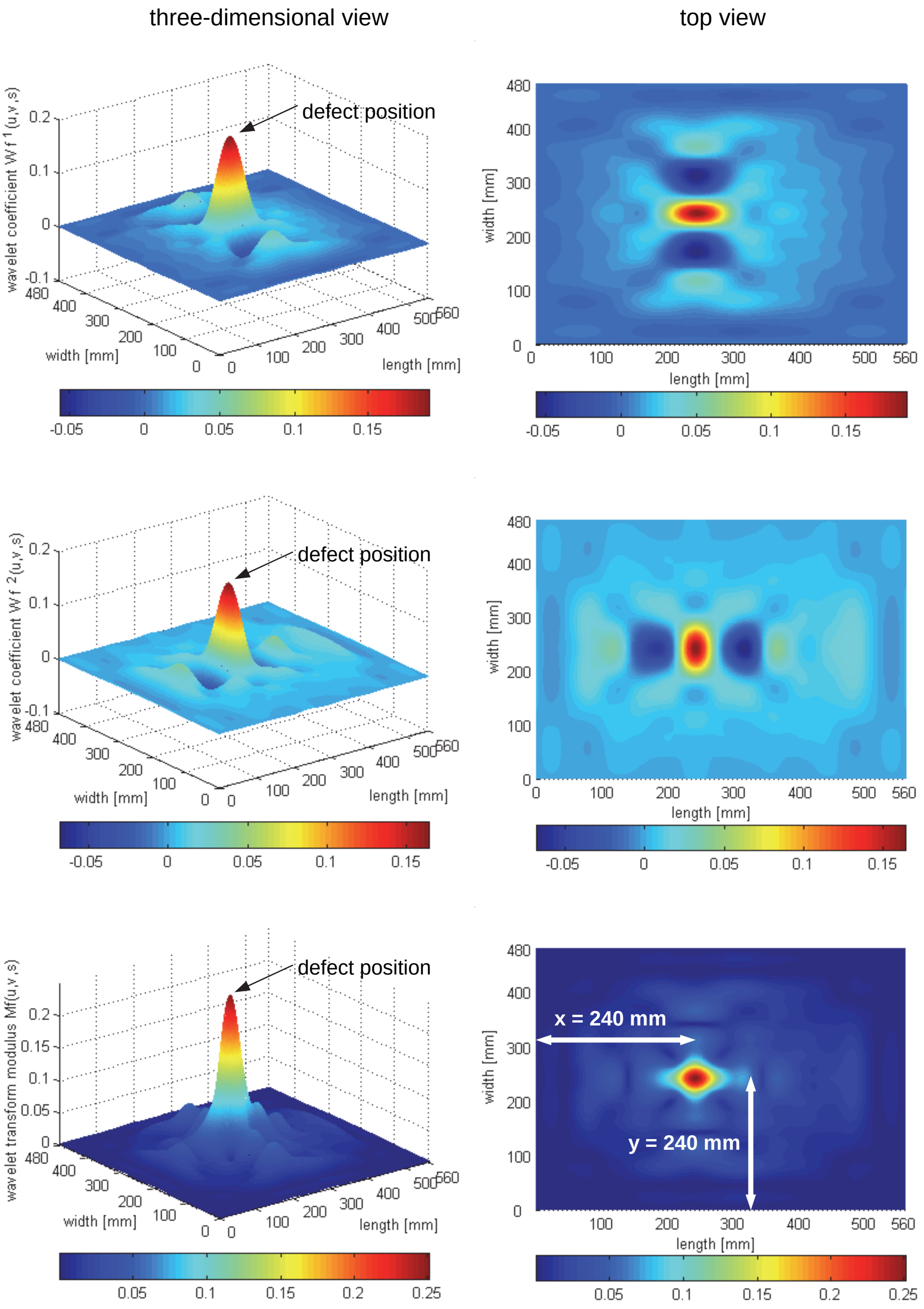

Fig. 4.47. Wavelet coefficients and wavelet transform modulus for the plate using rbio5.5 wavelet based on numerical data

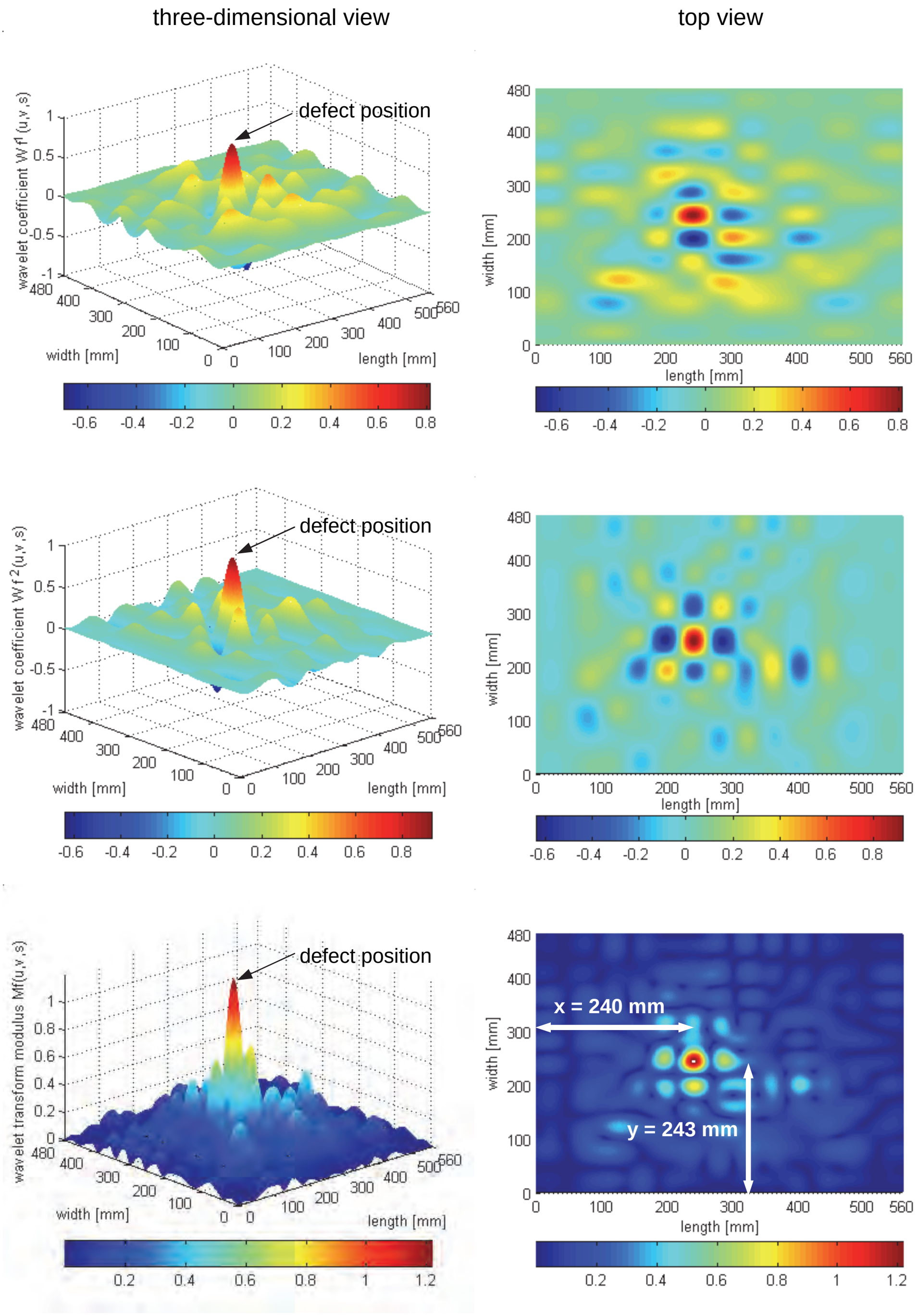

Fig. 4.48. Wavelet coefficients and wavelet transform modulus for the plate using rbio5.5 wavelet based on experimental data

Additional information about the defects can be obtained from the analysis of the angle $Af(u,v,s)$. However, in the case of the experimental data the noise corrupts the information contained in the angle plot. Since the coefficients $W^1 f(u,v,s)$ and $W^2 f(u,v,s)$ often change signs, therefore the angle of the gradient vector $\vec{\nabla}(f * \overline{\theta}_s)(x,y)$ quickly changes values (Fig. 4.50). It is impossible to directly locate the defect position from the experimental data. The angle plot obtained from the numerical data (Fig. 4.49) points the defect position by indicating the direction with sharpest signal variations.

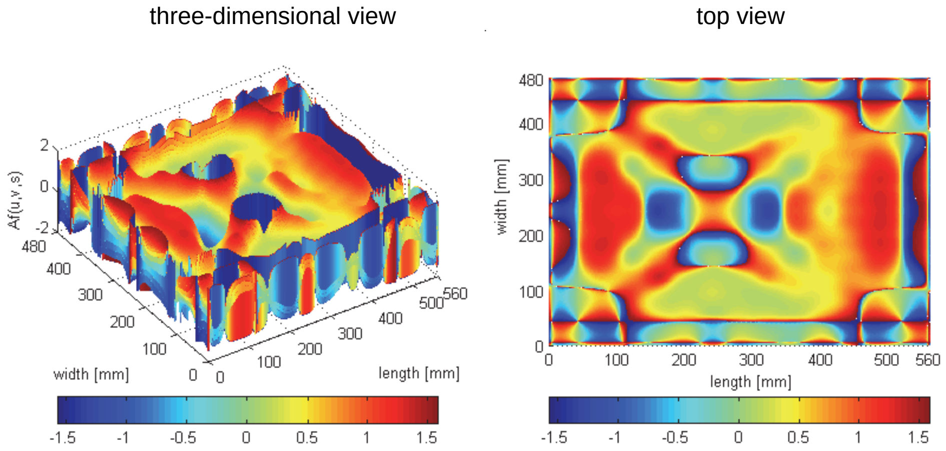
three-dimensional view

top view

Fig. 4.49. Angle of the wavelet transform vector using rbio5.5 wavelet based on numerical data

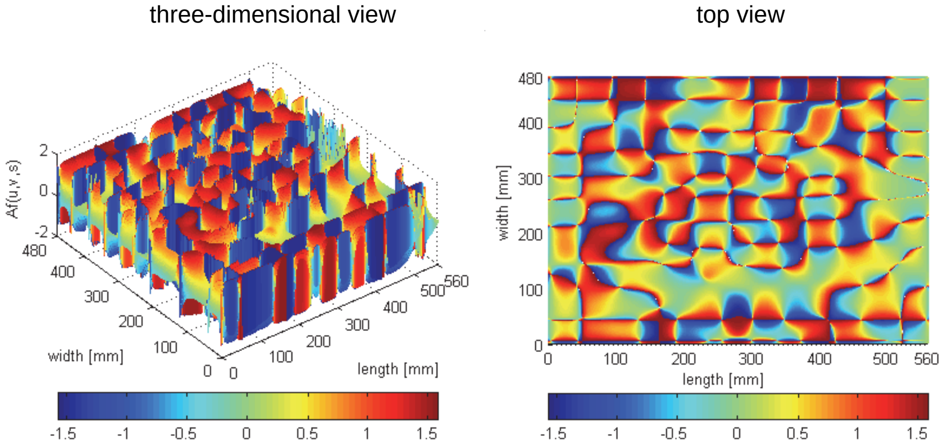
three-dimensional view

top view

Fig. 4.50. Angle of the wavelet transform vector using rbio5.5 wavelet based on experimental data

4.4. Cylindrical shell – mode shapes

4.4.1. Experimental investigations of cylindrical shell mode shapes

A steel cylindrical shell with the height of $H = 180$ mm, thickness $t_c = 3.4$ mm and diameters $D_1 = 293$ mm and $D_2 = 300$ mm is taken under consideration. The properties of material are: Young's modulus $E = 190$ G Pa, Poisson ratio $\nu = 0.25$ and mass density $\rho = 7850$ kg/m^3. The cylindrical shell is welded to a steel plate. It contains rectangular defect of length $L_r = 5$ mm, height $H_r = 60$ mm and depth of $a = 1$ mm. The defect is situated on inside surface of the cylinder. The horizontal projection and the surface development of the shell are given in Fig. 4.51. The distance from the defect left-down corner to the shell left-down corner in the horizontal and vertical directions are $L_1 = 285$ mm and $H_1 = 60$ mm, respectively. The area of the flaw amounts to 0.2% of surface area and the depth of the flaw is about 30% of the shell thickness.

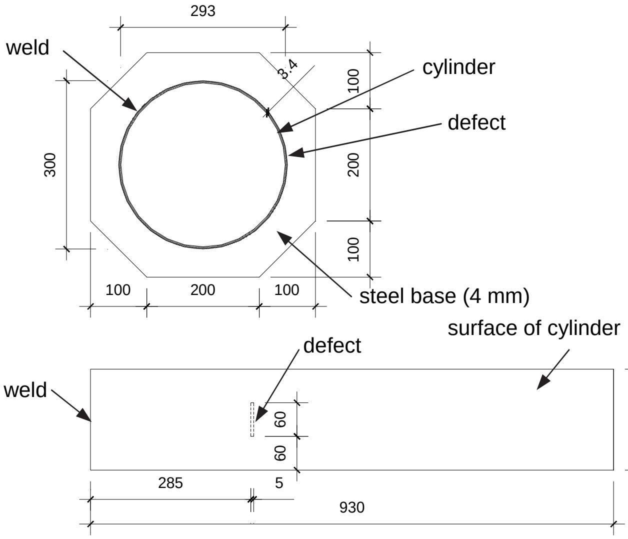

Fig. 4.51. Geometry of considered cylindrical shell

The shell was subjected to a dynamic impulse load applied by the modal hammer PCB 086C03 at the selected points spread along the central ring of the shell. The black dots, plotted on Fig. 4.52, indicate the points of the load application. The dynamic impulse loads were applied perpendicular to the shell surface. The total number of the considered measurement points was 62. The vibration responses were recorded using one accelerometer attached outside the shell at point no. 43. The data were collected by the data acquisition system Pulse type 3650C.

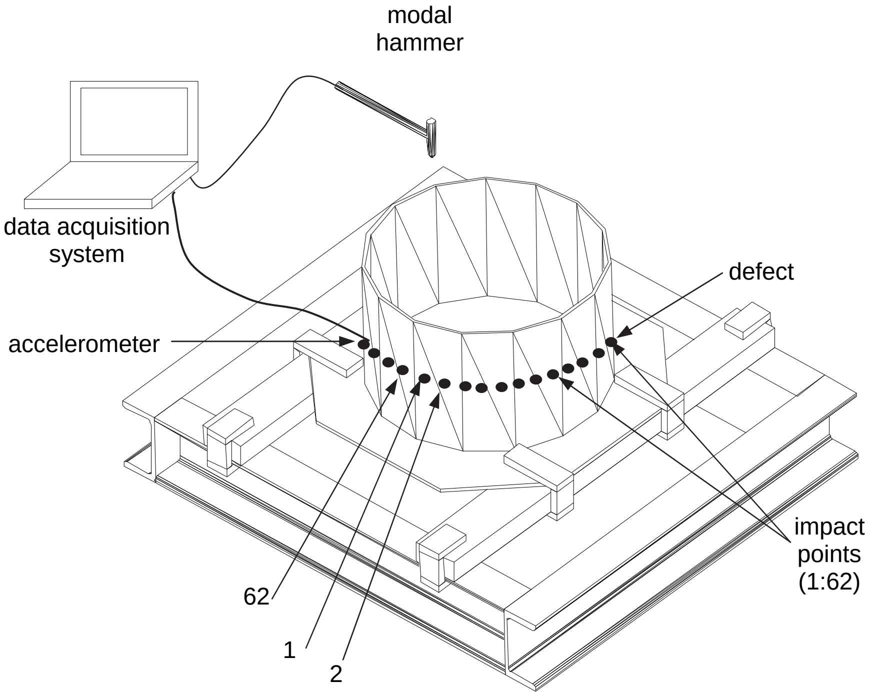

Fig. 4.52. Experimental setup

The mode shapes determination was performed by using the complex frequency response function (FRF) according to the procedure described in Section 3.2.1. At each point, from 1 to 62 the force signals were measured. The responses were recorded at the point no. 43, therefore 43th row of the FRF matrix was measured. All signals were transformed into a frequency domain by the fast Fourier transform. Fig. 4.53 illustrates the examples of the time signals $f_{11}(t)$ and $\ddot{x}_{43}(t)$ measured at the point no. 43 due to the force applied at the point no. 11 as well as their frequency representations $F_{11}(\omega)$ and $\ddot{X}_{43}(\omega)$. The imaginary part of the FRF $H_{11,43}(\omega)$ obtained from the measurement at the point 11 and the measurement of the response in the point no. 43 is shown in Fig. 4.54.

The $H_2(\omega)$ estimator was used to the mode shapes estimation. The imaginary part of the frequency response function estimator $H_{2(11,43)}(\omega)$ for the cylindrical shell is shown in Fig. 4.55. The experimentally determined mode shapes are given in Fig. 4.58

The coherence function is shown in Fig. 4.56. The coherence is close to one but at several points it reaches the values smaller than 1. It indicates that there is a weak relationship between the input and the output due to noise in the output or due to non-linear behaviour at the resonance point. However, the coherence near the first three frequencies, namely f_1 = 295.4 Hz, f_2 = 575.8 Hz and f_3 = 887.2 Hz is close to one.

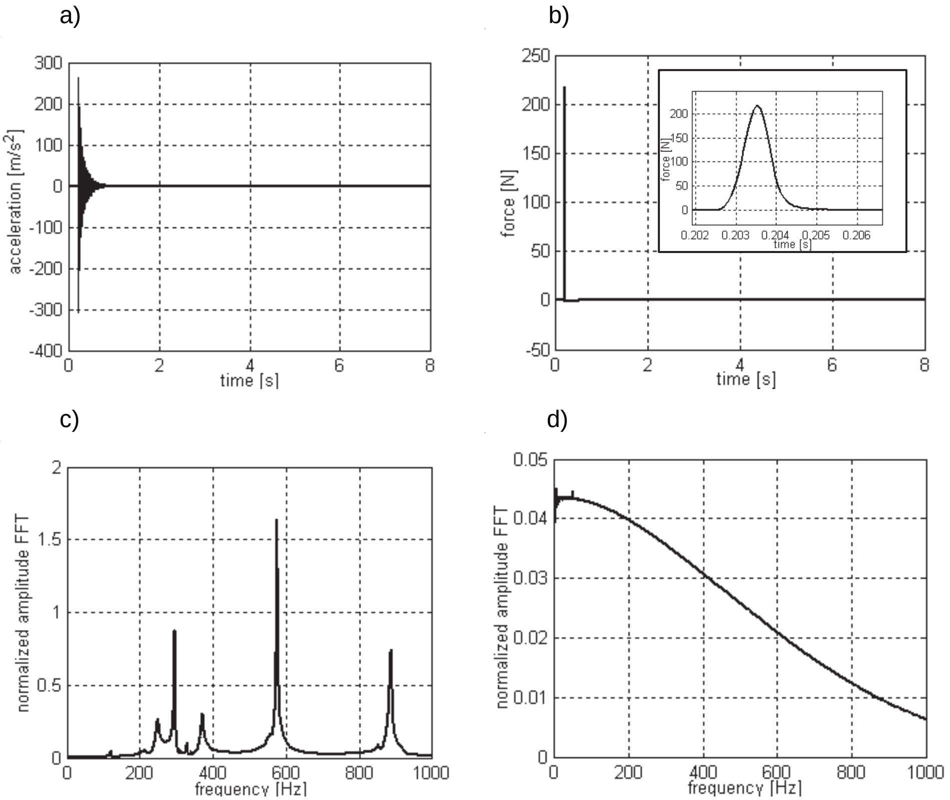

Fig. 4.53. Measured signals for the cylindrical shell: (a) acceleration signal; (b) force signal; (c) Fourier transform of acceleration; (d) Fourier transform of force

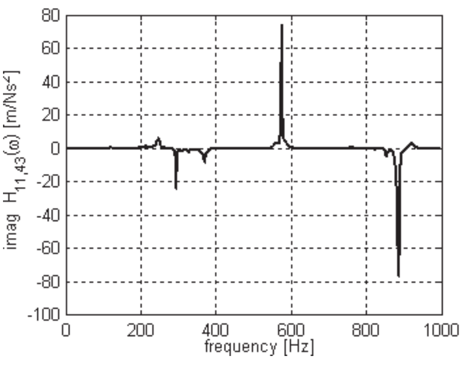

Fig. 4.54. Imaginary part of FRF for the shell

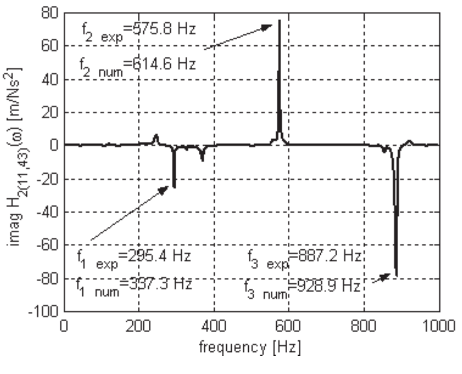

Fig. 4.55. Imaginary part of FRF estimator $H_2(\omega)$

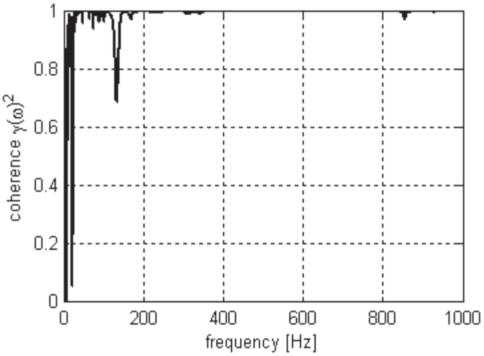

Fig. 4.56. Coherence function

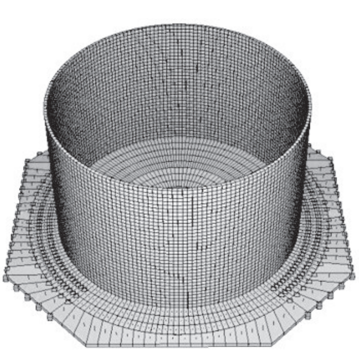

Fig. 4.57. Finite element method model of the cylinder

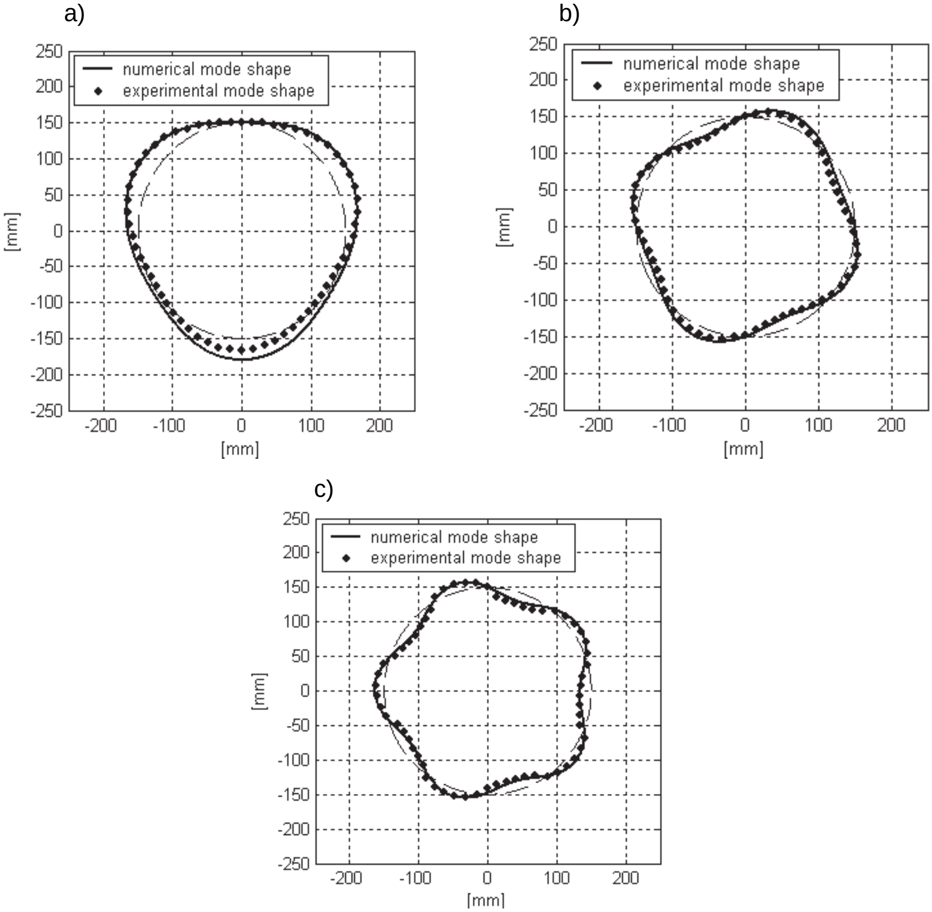

Fig. 4.58. Mode shapes of cylinder: a) first; b) second; c) third

4.4.2. Numerical simulations

The mode shapes for the damaged cylindrical shell were computed by the FEM program SOFiSTiK. The cylinder mode shapes were computed using the plane element in SOFiSTiK (quad) [30] with the size 5×5 mm. The cylinder is fixed to the plate and two edges of plate are modelled as fixed according to the geometry of the experimental model (Fig. 4.57).

The identified mode shapes are quite similar to the calculated modes. However, the complicated cylindrical structure, boundaries and material (rust, local protuberance of surface) cause that the differences between the calculated and the experimentally determined mode shapes are visible. The differences occur also between the numerical and the experimental frequencies. The first frequency for the shell was found to be: measured f_1 = 295.4 Hz and calculated f_1 = 337.3 Hz. The second measured frequency is f_2 = 575.8 Hz and calculated f_2 = 614.6 Hz. The third measured frequency is f_3 = 887.2 Hz and calculated f_3 = 928.9 Hz. The differences between measured frequencies relative to calculated frequencies range from 12.4% to 4.5%. A comparison between the numerical and experimental mode shapes is given in Fig. 4.58.

The mode shapes of the cylinder were measured with a sampling distance of 15 mm and calculated with the sampling distance of 5 mm. Therefore, a piecewise cubic spline data interpolation was used to the decrease the sampling distance to 1 mm. Then the mode shapes were normalized to 1.

4.4.3. Results of wavelet analysis

The wavelet analysis is conducted on the cylindrical shell three mode shapes assumed as a spatially distributed signal by the Gaussian wavelet family. The Gaussian wavelets with 4, 6, 8 and 10 vanishing moments are considered. Necessity of using wavelets with higher number of vanishing moments results from the mode shapes properties, i.e. the mode shapes are similar to polynomial higher order than 4. The one-dimensional CWT of the numerical and experimental mode shapes is performed for the scales $s = 1 \div 10$.

The wavelet transform moduli computed from the numerical data are shown in and Fig. 4.59, Fig. 4.60 and Fig. 4.61 for the first, second and third mode shapes, respectively. The Gaussian wavelet with 4 vanishing moments is quite appropriate for the first and the second mode shapes, but for third mode shape is insufficient (Fig. 4.61a) and the using wavelet with higher number of vanishing moments is necessary. The modulus maximum value grows with the increase of the scale and clearly points to the damage position at 288 mm from the left (assumed start point). The value of modulus maximum decreases with increase of the number of vanishing moments so using the wavelet with the number of vanishing moments higher than essential is not appropriate.

The CWT results based on the experimental third mode shape (Fig. 4.62) have additional maxima lines resulting from the measurement noise. Nevertheless, the maximum line, corresponding to the crack position, increases monotonically and for larger scales it achieves the largest value. The constant slope of the maximum line clearly indicates the damage location, which differs insignificantly for the Gaussian wavelets with 4, 6, 8 and 10 vanishing moments. The wavelet modulus computed with using the gaus4 wavelet provides maximum line at 299 mm from the start point, whereas the real centre defect location is 287.5 mm. The wavelet modulus computed with the use of the gaus6 provides maximum line at 298 mm from the weld, and the wavelet modulus computed with both the gaus8 and gaus10 gives defect position at 297 mm from the start point. The error between the recognized by wavelets the crack centre positions and actual ones amounts from 3.3% to 4%.

The wavelet transforms of the first and second experimental mode shapes regardless of vanishing moments do not allow detecting the defect position (Fig. 4.63). Damage is detected from the third mode shape, because this mode is dominated in the response induced in the experiment.

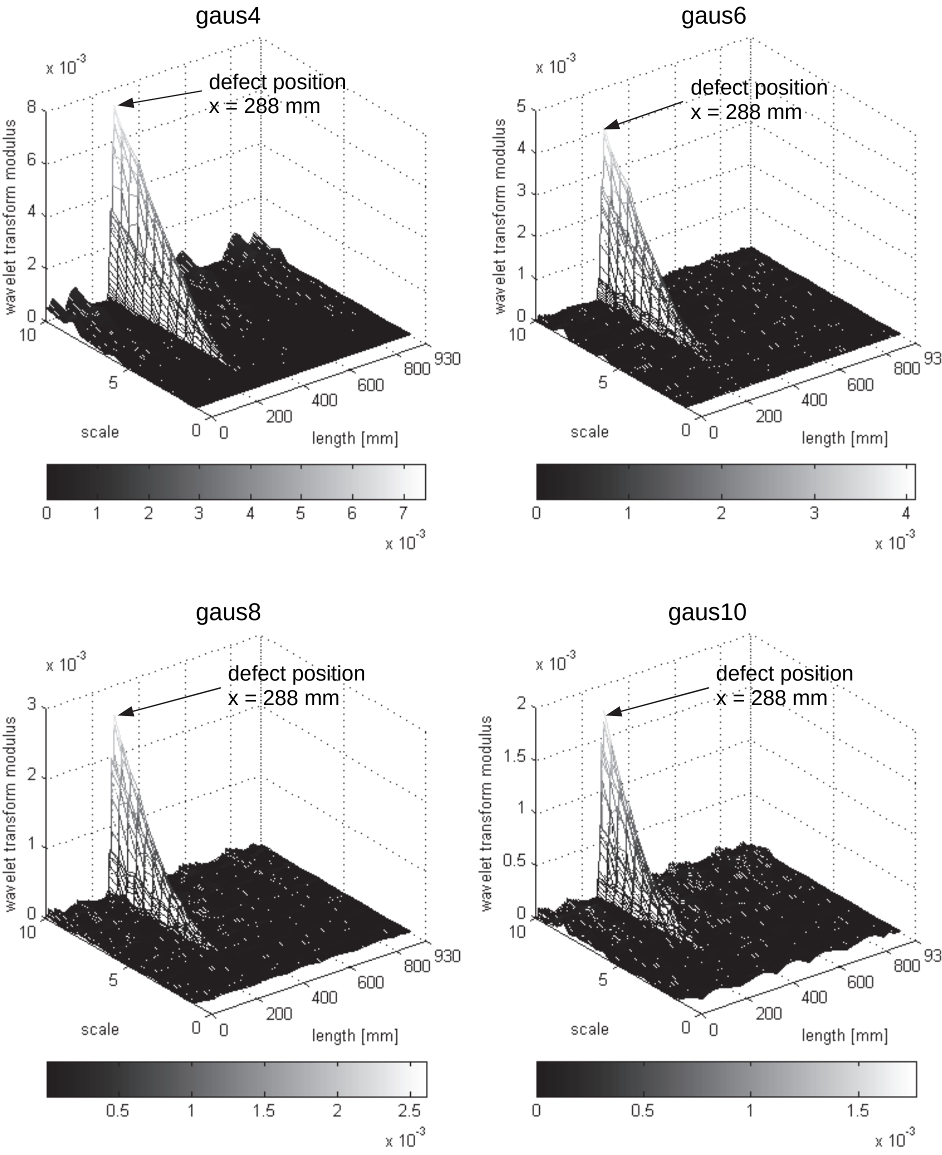

Fig. 4.59. Wavelet transform modulus of numerical first mode shape using Gaussian wavelet family

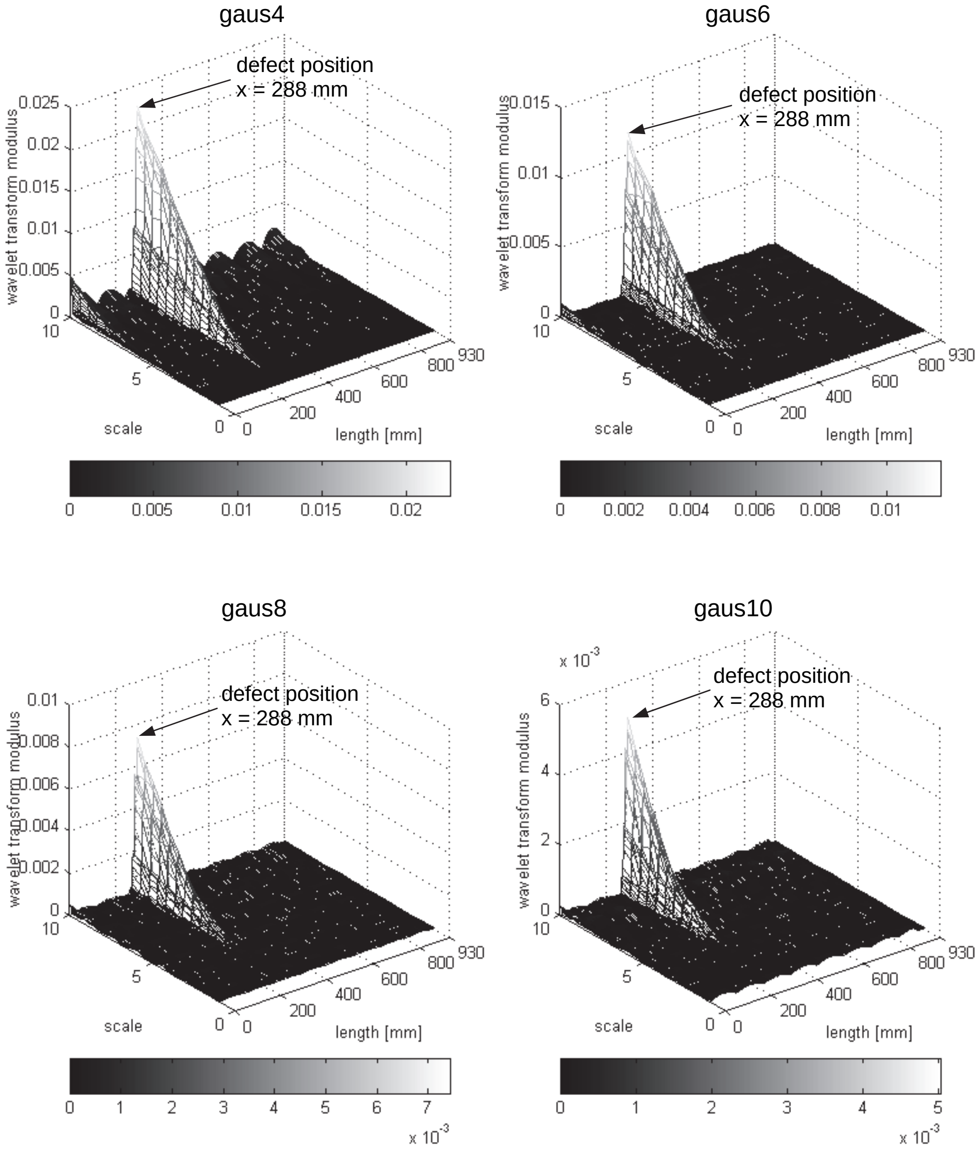

Fig. 4.60. Wavelet transform modulus of numerical second mode shape using Gaussian wavelet family

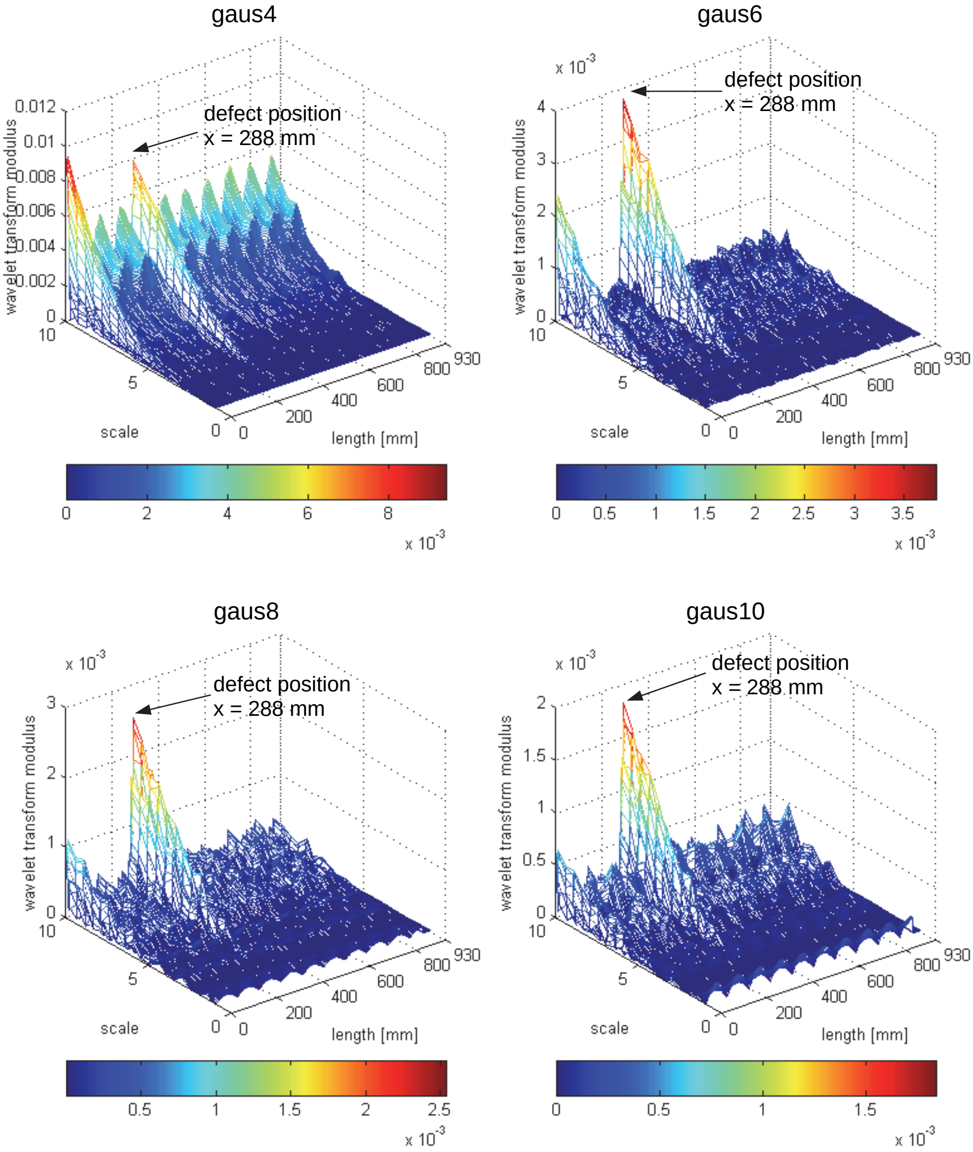

Fig. 4.61. Wavelet transform modulus of numerical third mode shape using Gaussian wavelet family

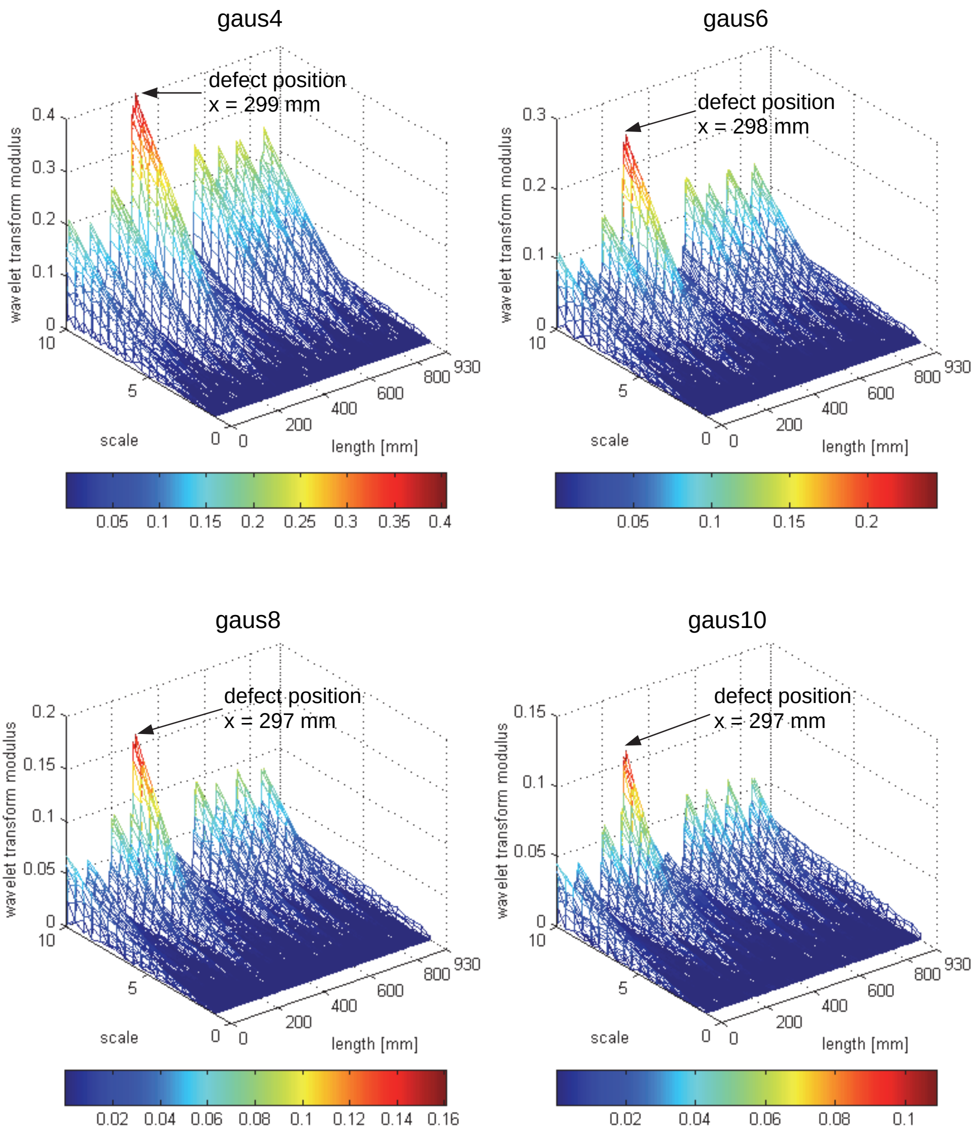

Fig. 4.62. Wavelet transform modulus of experimental third mode shape using Gaussian wavelet family

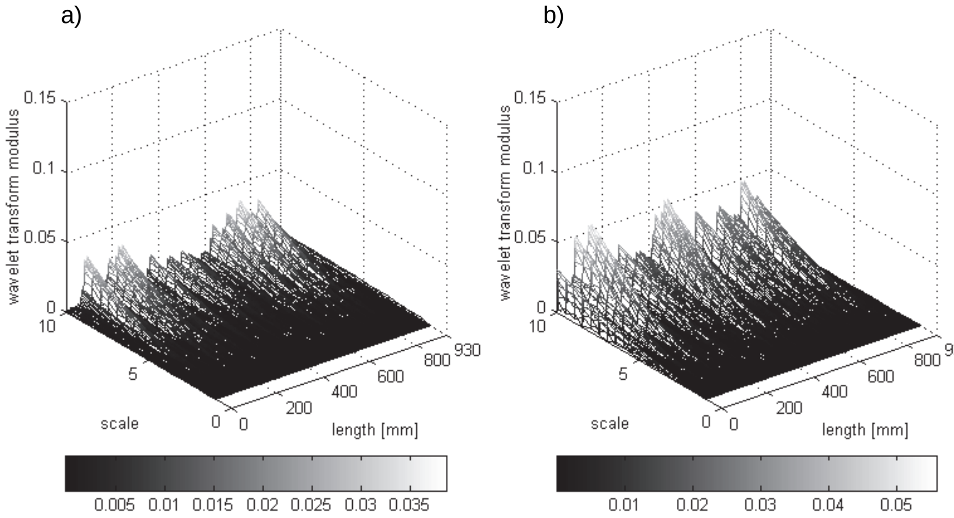

Fig. 4.63. Wavelet transform modulus of experimental mode shapes using gaus6:
a) first mode shape; b) second mode shape

4.5. Summary and conclusions

In this chapter wavelet analysis application in damage detection has been presented. Four experimental examples has been described, namely, the beam (static deflections and mode shapes), plate and cylindrical shell. The low resolution camera used for the photogrammetric determination of the beam deflection lines allowed the measurements with precision at least 0.17 mm (size of the pixel). The applied impact tests and FRF extraction by H_2 estimator proved to be a good method for determining the experimental mode shapes for the beam, plate and cylindrical structure.

In all considered problems the wavelet damage detection could effectively locate the defect on the noise free numerical data. In the case of the experimental data the effectiveness of the method is limited and for example the damage search for the beam on the mode shapes can be successful for the cracks of the relative height of 35%.

The best wavelets for the considered problems are the Gaussian with at least 4 vanishing moments and the Reverse Biorthogonal with 4 vanishing moments.

The conducted study showed that the modulus of the horizontal and vertical wavelet coefficients is a good index for the damage localization in two dimensional structures. However, use of the gradient vector angle between the horizontal and vertical coefficients is effective only on the noise free numerical data. The search of the flaw on the experimental wavelet coefficients gives very noisy 2D plot of the gradient angles due to the fact that the experimental coefficients often change sings along the width and length of the structure.

The experiments showed that the proposed method could locate the damage in the 3D cylindrical structure on the third mode shape. The considered flaw was relatively small since its area was 0.2% of the surface area and the thickness reduction was of 30%.

Chapter **5**

DAMAGE DETECTION SYSTEM BASED ON NEURAL NETWORKS

5.1. Fundamentals

Neural networks are networks of living nerve cells possessing the capability of thinking, feeling, learning and remembering [9]. The brain consists of about 10 billion interconnected neurons. The biological neuron (Fig. 5.1) has three main parts: a cell body, dendrites and an axon. The cell body contains the nucleus where the genetic material is placed. The dendrites are the branching structure receiving signals from other neurons. The axon sends a signal to other ones splitting in many branches. A connection between dendrites and the axon are structures called synapses.

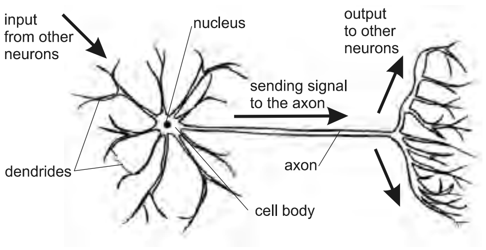

Fig. 5.1. Schematic of biological neuron

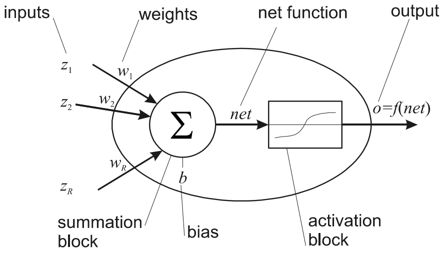

Fig. 5.2. Model of artificial neuron

An artificial neural network (ANN) is a general mathematical computing paradigm that models the operation of biological neural systems [41]. An artificial neuron can possess many inputs and many outputs. A neuron with a single input vector **z** and the output scalar *o* is shown in Fig. 5.2. This model includes also a weight vector **w**, a bias *b*, a summation block and an activation block. Inputs are transmitted through the connections that multiply their strength by weights. The net function is defined as follows [27]:

$$net = \sum_{r=1}^{R} w_r z_r + b. \tag{5.1}$$

The quantity *b* is called the bias and it is used to model a threshold [41]. A transfer (activation) function $f(net)$ produces an output *o*. In various neural networks different activation functions are used, for example hard-limit, linear, sigmoid etc. [21, 41].

5.2. Damage assessment using neural networks

The artificial neural networks have recently been a very popular subject and they have a various practical applications. The list of applications is very wide, for example aerospace (high performance aircraft autopilot, flight path simulation, aircraft control systems), defence (weapon steering, target tracking, object discrimination, facial recognition), electronics (code sequence prediction, integrated circuit chip layout, process control, chip failure analysis, machine vision), financial (real estate appraisal, loan advisor, mortgage screening, corporate bond rating, credit-line use analysis), medical (breast cancer cell analysis, electrocardiogram analysis, prosthesis design, optimization of transplant times, hospital expense reduction), speech (speech recognition, speech compression, vowel classification) and many others [21].

One of these various applications is damage identification. Damage recognition and localization were applied to different structures like the ships [129] or helicopters [12], crates of beverages [125], joint in steel structures [124], bridges [4, 122]. In the previous studies as inputs of ANN were used: the ultrasonic signals [59, 78], broad-band spectral signals [29], natural frequencies [100, 116, 126] or vibration responses [4, 44, 121]. From among many types of artificial neural networks the backpropagation neural network is the most commonly used to the analysis of the civil engineering problems [38, 52].

In this study the wavelet coefficients are used to predict damage localization by an ANN system. Damage localization can be observed from the plot of the wavelet coefficients as a peak (Fig. 5.3a). However, noise is always present in measurements and it sometimes masks defect position in the transformed response (Fig. 5.3b). A neural network can effectively deal with noisy data and it can learn to recognize the wavelet-based defect features, which could not be directly observed from a plot. The aim of the study is to design a neural network system based on the wavelet coefficients that makes the online damage localization possible.

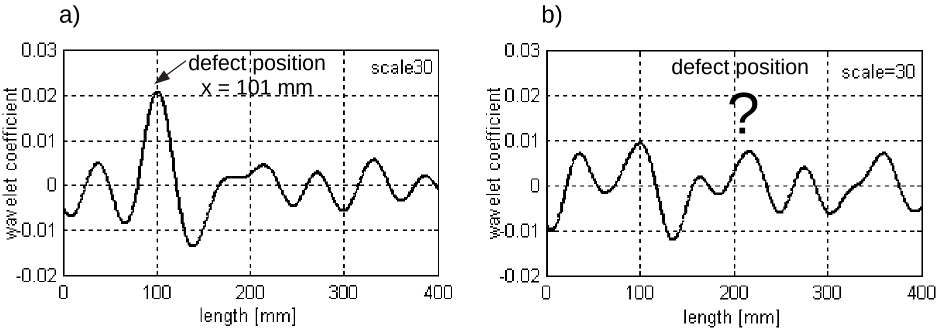

Fig. 5.3. Experimental wavelet coefficients: a) beam case 3 from Table 4.1;
b) beam case 5 from Table 4.1

5.3. Backpropagation neural networks

The neural networks have two modes of action, namely the training mode and the using (testing) mode. Feedforward supervised multilayer networks are the most commonly used with the backpropagation algorithm. These networks often have one or more hidden layers of sigmoid neurons followed by an output layer of linear neurons [21]. Each layer of networks receives inputs only from previous layer. There is no connection between neurons in the layer (Fig. 5.4).

The backpropagation algorithm is a supervised technique in the sense that there is some external teacher who knows what the correct response for given input vector should be [27]. The training requires a set of inputs and known targets. The input samples are fed through the network many cycles and they are compared with the targets until the network recognizes the relationship between the inputs and outputs. One transmission of the signals and backpropagation of the errors is called an epoch.

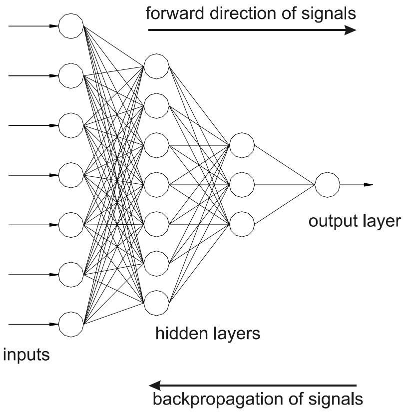

Fig. 5.4. Schematic view of the multilayer feedforward network

The basic idea of backpropagation is to propagate the error backward through the network (Fig. 5.4). The backpropagation training consists of two passes, namely forward and backward. In the forward pass the input signal propagates through the network layer by layer and a set of outputs are produced as an actual response of the network. Error signal is obtained from the difference between the actual response and the target. This error is propagated backward through the network [9]. The aim of the backpropagation algorithm is to minimize the sum of error for all the training samples.

The derivation of the backpropagation algorithm is explained in details in literature, for instance [9, 27, 41]. The neural network with input, hidden and output layers is considered. The net function for the hidden layer neurons and the net function for output layer neurons are given in the form:

$$net_m^{h(p)} = \sum_{r=1}^{R} w_{mr}^h z_r^{(p)} + b_m^h, \tag{5.2}$$

$$net_k^{o(p)} = \sum_{m=1}^{M} w_{km}^o i_m^{(p)} + b_k^o, \tag{5.3}$$

where *R* and *M* denote number of neurons in input and hidden layers, respectively. The superscript *p* refers to a p^{th} input pattern and b is a bias. The input from the m^{th} hidden layer neuron to the output layer neuron is given as a sigmoid function, which can be the logarithmic sigmoid function:

$$i_m^{(p)} = f_m^h\left(net_m^{h(p)}\right) = \frac{1}{1+e^{-net_m^{h(p)}}}, \tag{5.4}$$

or as the hyperbolic tangent sigmoid function:

$$i_m^{(p)} = f_m^h\left(net_m^{h(p)}\right) = \frac{1}{1+e^{-2net_m^{h(p)}}} - 1. \tag{5.5}$$

The output for the output layer neurons is given as an identity function:

$$o_k^{(p)} = f_k^o\left(net_k^{o(p)}\right) = n_k^{o(p)}. \tag{5.6}$$

The error minimized by training algorithm is defined as:

$$E^{(p)} = \frac{1}{2}\sum_{k=1}^{K}\left(d_k^{(p)} - o_k^{(p)}\right)^2, \tag{5.7}$$

where K denotes number of neurons in an output layer and $d_k^{(p)}$ is a known target. The global error can be expressed as a sum of errors of all patterns:

$$E = \sum_{p=1}^{P} E^{(p)}, \tag{5.8}$$

where P is a number of all patterns. Inserting Eq. (5.6) into Eq. (5.7) yields:

$$E^{(p)} = \frac{1}{2}\sum_{k=1}^{K}\left(d_k^{(p)} - f_k^o\left(net_k^{o(p)}\right)\right)^2. \tag{5.9}$$

The gradient $E^{(p)}$ with respect to the weights of the output layer is:

$$\begin{aligned}\frac{\partial E^{(p)}}{\partial w_{km}^o} &= -\left(d_k^{(p)} - o_k^{(p)}\right)\frac{\partial f_k^o\left(net_k^{o(p)}\right)}{\partial\left(net_k^{o(p)}\right)}\frac{\partial\left(net_k^{o(p)}\right)}{\partial w_{km}^o} = \\ &= -\left(d_k^{(p)} - o_k^{(p)}\right) f_k^{o\prime}\left(net_k^{o(p)}\right) i_m^{(p)},\end{aligned} \tag{5.10}$$

whereas the gradient $E^{(p)}$ with respect to the weights of the hidden layer is:

$$\frac{\partial E^{(p)}}{\partial w_{mr}^h} = -f_m^{h\prime}\left(net_m^{h(p)}\right) z_r^{(p)} \sum_{k=1}^{K}\left(d_k^{(p)} - o_k^{(p)}\right) f_k^{o\prime}\left(net_k^{o(p)}\right) w_{km}^o . \tag{5.11}$$

The weight update equations for both output and hidden layers, are given in the form:

$$w_{km}^o(t+1) = w_{km}^o(t) - \eta\frac{\partial E^{(p)}}{\partial w_{km}^o}, \tag{5.12}$$

$$w_{mr}^h(t+1) = w_{mr}^h(t) - \eta\frac{\partial E^{(p)}}{\partial w_{mr}^h}, \tag{5.13}$$

where t is iteration step and η denotes a learning rate assumed as the same on all neurons in all layers. The larger learning rate means larger iteration step. If the learning rate is too large the algorithm becomes unstable. If the learning rate is too small the algorithm takes a long time to converge [21].

There are many variations of the backpropagation algorithm, namely gradient descent with momentum algorithms, conjugated gradient algorithms, quasi-Newton algorithms, etc. In this study the scaled conjugate gradient algorithm is used. This algorithm is a variant of conjugated gradient algorithms. The basic backpropagation algorithms modify the weights in the direction of the negative of the gradient. However, this direction, in which the performance function is decreasing most rapidly, does not necessarily provide the fastest convergence. In the conjugate gradient algorithms a search is performed along the conjugate direction, which provides generally faster convergence than the direction of the negative gradient (the steepest descent direction) [21]. In most of conjugated gradient algorithms, the step size is modified at each iteration. The scaled conjugate gradient algorithm developed by Moller [73] makes it possible to avoid the time consuming line-search per learning iteration in order to a scaled the step size.

5.4. Neural networks defect detection system

5.4.1. Architecture

The used network (Fig. 5.5) consists of three layers – two hidden layers and one output layer. The hyperbolic tangent sigmoid function was selected for the hidden layers and the linear transfer function was selected for the output layer. The input of the neural network is a 401-elements vector of the wavelet coefficients. The first hidden layer has 50 neurons whereas the second one has 5 neurons. These numbers were chosen by guesswork and experience. The 1-element output indicates the position of the structural defect.

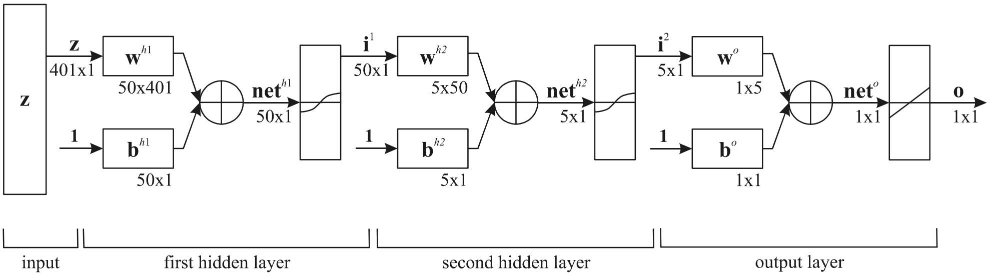

Fig. 5.5. Considered multiplayer feedforward network

5.4.2. Training

The wavelet coefficients computed for the beam deflection line (case 3 from Table 4.1) were used as the inputs of the neural network. The considered beam is presented in Fig. 5.6. The distance L_1 from the clamped end to the crack changes, with sampling distance 4 mm, from 80 mm to 320 mm, giving 61 different crack localizations. Additionally, the wavelet coefficients of the experimental deflection line (beam case no. 4 from Table 4.1) were used. The wavelet coefficients of the numerical and experimental deflection line were calculated using both gaus4 and rbio5.5 wavelets for scales 10, 20, 30 and 40. The detailed register of the input components data is presented in Table 5.1. The total number of the input patterns is 1472.

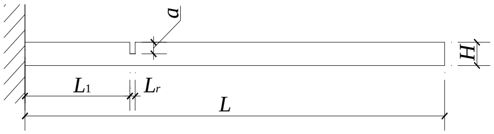

Fig. 5.6. Considered beam for neural network testing

Table 5.1

Patterns (wavelet coefficients based on beam static deflections) used for training of neural network

Input patterns (wavelet coefficients)	Wavelet	Scale	Number of patterns
numerical without noise (beam case 3 from Table 4.1)	gaus4	s = 10	61
		s = 20	61
		s = 30	61
		s = 40	61
	rbio5.5	s = 10	61
		s = 20	61
		s = 30	61
		s = 40	61
numerical with noise (beam case 3 from Table 4.1)	gaus4	s = 10	2 x 61
		s = 20	2 x 61
		s = 30	2 x 61
		s = 40	2 x 61
	rbio5.5	s = 10	2 x 61
		s = 20	2 x 61
		s = 30	2 x 61
		s = 40	2 x 61
experimental (beam case 4 from Table 4.1)	gaus4	s = 10	1
		s = 20	1
		s = 30	1
		s = 40	1
	rbio5.5	s = 10	1
		s = 20	1
		s = 30	1
		s = 40	1
total			1472

The selected wavelet coefficients computed for the numerical data (without and with noise) and for the experimental data are given in Fig. 5.7. Training of the neural network has been conducted on the wavelet coefficients which clearly indicate damage location, as well as the wavelet coefficients which mask information about the defect position.

The neural network modelling, training and using were performed using MATLAB® *Neural Network Toolbox*. Before the training process the inputs and targets were normalized to have zero means and unit standard deviation. The input vectors occurred concurrently (at the same time or in no particular time sequence) and they do not interact with each other. During training the weights and biases of the network were iteratively adjusted to minimize the network performance function, which was chosen as *mse* (mean sum of squares of the network errors):

$$mse = \frac{2E}{P} \,. \tag{5.14}$$

The batch training was used to training process, in which weights and biases are updated only after the entire training set has been applied [21].

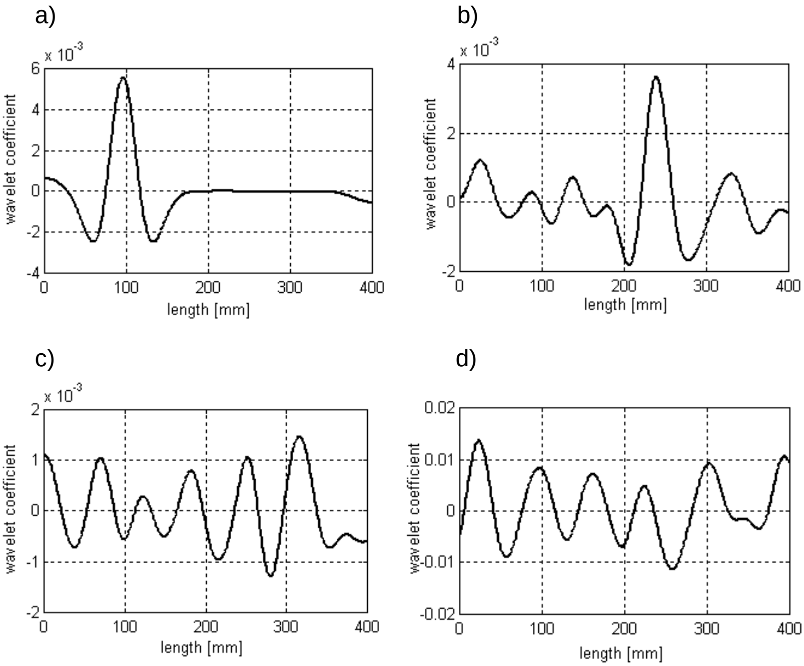

Fig. 5.7. Selected wavelet coefficients used as inputs: a) numerical; b), c) numerical with noise; d) experimental

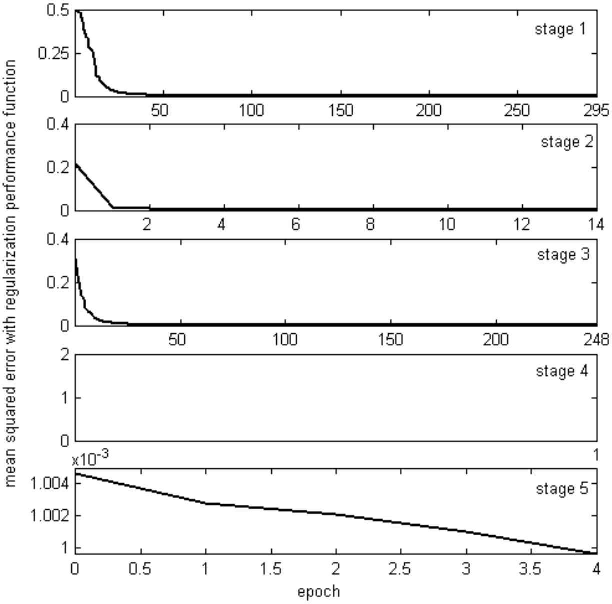

Fig. 5.8. The mean squared errors with regularization of performance function in the progress of training

To overcome the overfitting problem, the regularization was used. Overfitting means that the error on the training data has a very small value but the error is large on the new simulated data. In the regularization method the performance function, normally chosen as the mean sum of squares of the network errors, is modified by adding a term that consist of the mean of the sum of squares of the network weights and biases [21]:

$$msereg = \gamma mse = (1-\gamma)msw, \tag{5.15}$$

where γ is the performance ratio and *msw* can be written as:

$$msw = \frac{1}{n}\sum_{j=1}^{n} w_j^2 \ . \tag{5.16}$$

It is difficult to determine the optimum performance parameter, since too large parameter γ provides overfitting, whereas too small parameter provides no fit in the training data. In performed tests the ratio γ was set to 0.5.

The network was trained on both ideal and noisy data in five stages:

- Stage 1 – the numerical data without noise,
- Stage 2 – the experimental data,
- Stage 3 – all data (the numerical data without noise, experimental data, numerical data with noise),
- Stage 4 – the experimental data,
- Stage 5 – the numerical data without noise.

First the network was trained on ideal data and then on the experimental data. To obtain the network not sensitive to noise, in the third stage network was trained with both noisy and noisy-free data. Next the experimental data were again used for training. Finally, to ensure that network reacts properly on the ideal data, the numerical data without noise were used. In each stage the weights and biases were given from previous stage, except the first stage, in which weights and biases were random. The network was trained repeatedly and at each time a different set of random initial weights and biases was used.

Training was stopped either when the error of training *msereg* achieved 10^{-3} or for a maximum of 500 epochs. The progress of training can be observed in Fig. 5.8. The number of epochs amounted from 0 for stage 4 to 295 for stage 1.

The results for training mode are given in Fig. 5.9. On the horizontal axis the actual crack positions are introduced whereas on the vertical axis neural network predicted ones. The points relating to the numerical noisy-free patterns, the numerical noisy patterns and the experimental patterns are distinguished by different marks. The dotted line represents the state, when the target value is equal to the predicted value. The continuous line is the best linear fit between the data.

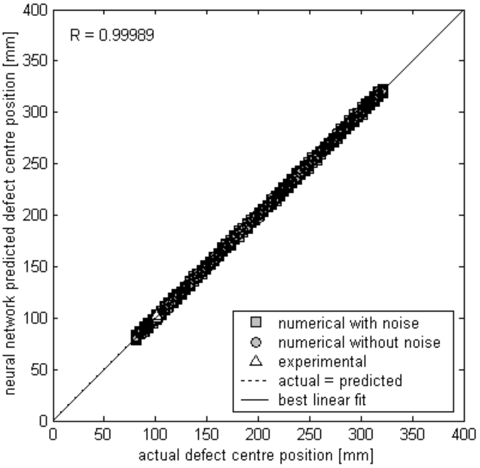

Fig. 5.9. Results of the training mode

Additionally, the correlation coefficient R was calculated, which is a normalized measure of the strength of the linear relationship between the target value and the predicted value:

$$R = \frac{\sum_{i=1}^{P}(o_i - \bar{o})(d_i - \bar{d})}{\sqrt{\sum_{i=1}^{P}(o_i - \bar{o})^2}\sqrt{\sum_{i=1}^{P}(d_i - \bar{d})^2}}, \tag{5.17}$$

where o_i and d_i are the output value and target value; $\bar{o}$ and $\bar{d}$ denote mean values. The perfect correlated data results in a correlation coefficient equal to 1, whereas when there is no correlation between target and predicted values when the correlation coefficient is equal to 0. In obtained results correlation coefficient amounts 0.99989 and is very close to 1, which indicates good compatibility between the outputs and targets.

To demonstrate the feasibility of the damage location prediction based on trained neural network, new patterns were simulated in the neural network using mode. All experimental wavelet coefficients presented in Chapter 4 (for the beam deflection lines, beam mode shapes, plate mode shapes and shell mode shapes) were tested in the neural network and results were compared with the damage location recognized by the wavelet analysis.

5.4.3. Results of testing on experimental beam deflection lines

The wavelet coefficients, computed from the experimentally determined static deflection profiles, were tested in the neural network. The wavelet coefficients were calculated using both the gaus4 and rbio5.5 wavelets for scales 10, 20, 30 and 40. The set of experimental data consisting of 20 patterns is described in detail in Table 5.3. Additionally, the numerical patterns were tested. The set of numerical data was prepared for the different crack positions. The distance L_1 from the clamped end to the crack has been changed, with sampling distance 4 mm, from 82 mm to 318 mm giving 60 different crack locations. The set of numerical data consists of 960 patterns and it is given in Table 5.2.

The results of the using mode are illustrated in Fig. 5.10. Crack localizations in the numerical data of the using mode are different from the crack localizations in the numerical data of the training mode. However, the predicted values are in good agreement with the actual values. The correlation coefficient reaches 0.99348. The results of the using mode for experimental data are given in Table 5.3. The errors between the actual and predicted values of the crack centre positions are calculated. The

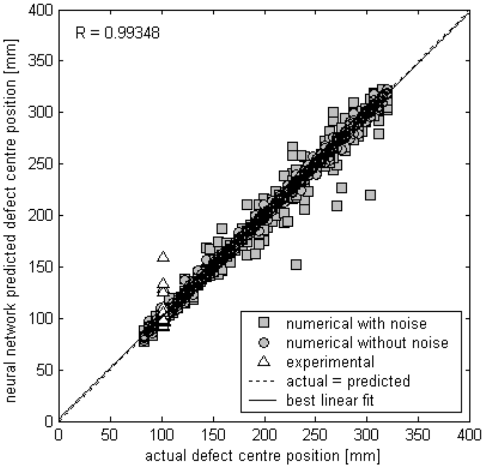

Fig. 5.10. Results of neural network for beam deflection lines

differences are from 0.05% to 55.57%. It can be concluded that the neural network can predict the crack location even if the wavelet coefficients are not legible.

Table 5.2

Numerical patterns (wavelet coefficients based on beam static deflections) tested in network

Input patterns (wavelet coefficients)	Wavelet	Scale	Number of patterns
numerical without noise (beam case 3 from Table 4.1)	gaus4	s = 10, s = 20, s = 30, s = 40	6 x 60
	rbio5.5	s = 10, s = 20, s = 30, s = 40	6 x 60
numerical with noise (beam case 3 from Table 4.1)	gaus4	s = 10, s = 20, s = 30, s = 40	6 x 60
	rbio5.5	s = 10, s = 20, s = 30, s = 40	6 x 60
total			960

Table 5.3

Neurally predicted versus recognized by wavelet analysis defect locations (input: wavelet coefficients based on beam experimental static deflections, beam cases according with Table 4.1)

Input patterns	Wavelet	Scale	Crack centre position [mm]			Error [%]	
			Actual	Recognized by CWT	Predicted by ANN	Actual vs. recognized	Actual vs. predicted
case 2	gaus4	s = 30	101	–	129.2629	–	27.9831
	rbio5.5	s = 30	101	–	92.9908	–	7.9299
case 3	gaus4	s = 30	101	101	91.1942	0	9.7087
	rbio5.5	s = 30	101	104	98.6776	2.9703	2.2994
case 5	gaus4	s = 30	102	–	125.6298	–	23.1665
	rbio5.5	s = 30	102	–	134.0778	–	31.4488
case 6	gaus4	s = 30	102	100	107.3257	1.9608	5.2213
	rbio5.5	s = 30	102	–	158.6849	–	55.5735
case 7	gaus4	s = 30	102	101	100.7752	0.9804	1.2008
	rbio5.5	s = 30	102	105	101.9534	2.9412	0.0457
case 8	gaus4	s = 30	103	106	102.6724	2.9126	0.3180
	rbio5.5	s = 30	103	–	96.4270	–	6.3816
case 9	gaus4	s = 30	103	97	105.0463	5.8252	1.9867
	rbio5.5	s = 30	103	96	97.0728	6.7961	5.7546
case 10	gaus4	s = 30	103	101	100.5001	1.9417	2.4271
	rbio5.5	s = 30	103	101	103.0685	1.9417	0.0665
case 12	gaus4	s = 30	102.5	–	110.7582	–	8.0568
	rbio5.5	s = 30	102.5	–	106.0323	–	3.4462
case 13	gaus4	s = 30	102.5	103	100.1979	0.4878	2.2459
	rbio5.5	s = 30	102.5	102	98.6917	0.4878	3.7154

5.4.4. Results of testing on experimental beam mode shapes

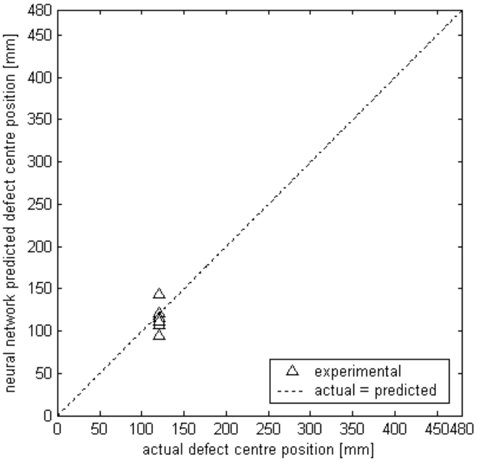

Fig. 5.11. Results of neural network for experimental beam mode shapes

In the next test the wavelet coefficients of the experimentally determined first and second mode shapes were considered. The wavelet coefficients were computed using the gaus4 as well as gaus6 wavelet for scales 40 and 60. The experimental patterns in amount of 6 are described in detail in Table 5.4.

In Fig. 5.11 the results of the using mode are presented. The neural network predicted values and actual values are similar. A comparison between neurally predicted and recognized by the wavelet analysis the defect locations are presented in Table 5.4. The calculated errors between predicted and recognized values of defect centre positions indicate differences have range from 0.45% to 21.54%.

Table 5.4

Neurally predicted versus recognized by wavelet analysis defect locations (input: wavelet coefficients based on beam experimental mode shapes, beam cases according with Table 4.3)

Input patterns	Wavelet	Scale	Crack centre position [mm]			Error [%]	
			Actual	Recognized by CWT	Predicted by ANN	Actual vs. recognized	Actual vs. predicted
case 1 mode 1	gaus4	s = 60	121	132	106.4242	9.0909	12.0461
case 1 mode 2	gaus4	s = 40	121	129	94.9328	6.6116	21.5431
case 1 mode 2	gaus6	s = 40	121	129	120.4544	6.6116	0.4509
case 2 mode 1	gaus4	s = 60	121	136	114.9464	12.3967	5.0030
case 2 mode 2	gaus4	s = 40	121	117	111.7433	3.3058	7.6502
case 2 mode 2	gaus6	s = 40	121	116	142.8683	4.1322	18.0730

5.4.5. Results of testing on experimental plate mode shapes

The two-dimensional wavelet coefficients for the plate were converted into the one-dimensional wavelet coefficients since the lines at different locations can be treated separately. Only the lines passing through the centre of the defect were tested. The wavelet coefficients along the length of the plate were extracted from the vertical two-dimensional coefficients, whereas the wavelets coefficients along the width of the plate were extracted from the horizontal two-dimensional wavelet coefficients. One-dimensional wavelets coefficients in both directions, i.e. along *x* axis and along *y* axis, computed from the experimentally determined first mode shape were tested in neural network. The set of the experimental data consists of 8 patterns, i.e. 4 patterns along the length of the plate and 4 patterns along the width of the plate. A description of experimental patterns is given in Table 5.5 and Table 5.6. The wavelet coefficients were calculated using the rbio5.5 wavelet for scales 16, 20, 30 and 40.

The results of the neural network using mode indicate a good agreement of the neural network predicted values with the actual ones. The neural network predicted values of the defect location along the *x* axis (the length of the plate) are presented in Fig. 5.12, whereas the neural network predicted values of the defect location along the *y* axis (the width of the plate) are presented in Fig. 5.13. A comparison between the neurally predicted and recognized by wavelets the defect locations are presented in Table 5.5 and Table 5.6 for the *x* and *y* direction, respectively. The errors between predicted and recognized values of crack centre positions are calculated. Differences have range from 1.09% to 7.81%.

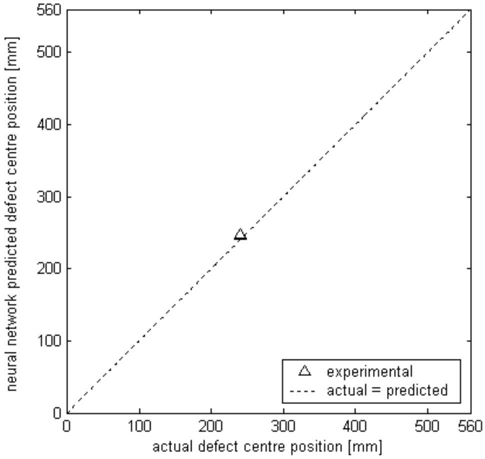

Fig. 5.12. Results of neural network for experimental plate mode shapes (along *x* axis)

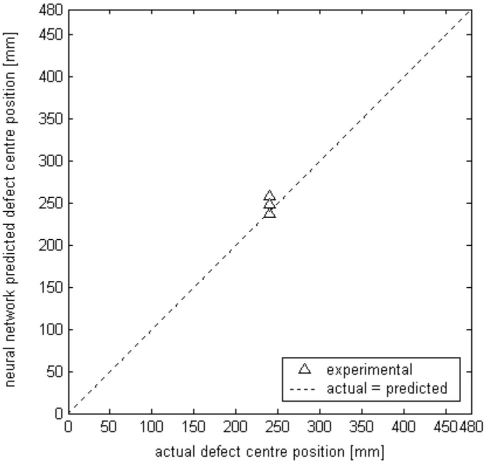

Fig. 5.13. Results of neural network for experimental plate mode shapes (along *y* axis)

Table 5.5

Neurally predicted versus recognized by wavelet analysis defect locations (input: wavelet coefficients based on plate experimental mode shapes, along *x* axis)

Input patterns	Wavelet	Scale	Crack centre position [mm]			Error [%]	
			Actual	Recognized by CWT	Predicted by ANN	Actual vs. recognized	Actual vs. predicted
mode 1	rbio5.5	s = 40	240	240	245.6954	0	2.3731
mode 1	rbio5.5	s = 30	240	240	247.4461	0	3.1026
mode 1	rbio5.5	s = 20	240	240	246.4185	0	2.6744
mode 1	rbio5.5	s = 16	240	240	246.9593	0	2.8997

Table 5.6

Neurally predicted versus recognized by wavelet analysis defect locations (input: wavelet coefficients based on plate experimental mode shapes, along *x* axis)

Input patterns	Wavelet	Scale	Crack centre position [mm]			Error [%]	
			Actual	Recognized by CWT	Predicted by ANN	Actual vs. recognized	Actual vs. predicted
mode 1	rbio5.5	s = 40	240	243	258.7375	1.25	7.8073
mode 1	rbio5.5	s = 30	240	243	247.7103	1.25	3.2126
mode 1	rbio5.5	s = 20	240	243	237.3833	1.25	1.0903
mode 1	rbio5.5	s = 16	240	243	237.3808	1.25	1.0913

5.4.6. Results of testing on experimental shell mode shapes

The last test was performed for the wavelet coefficients of the experimentally determined first, second and third shell mode shapes. The set of experimental data, consisting of 12 patterns, is described in Table 5.7. The wavelet coefficients were calculated for scales 40 and 60 using both the gaus4 and gaus6 wavelets.

The results of the using mode are presented in Fig. 5.14, whereas the values of the neural network predicted values and actual ones are given in Table 5.7. The differences between predicted and actual defect centre positions have range from 0.42% to 10.72%. The neural network was able to predict defect location even if the wavelet coefficients were not legible.

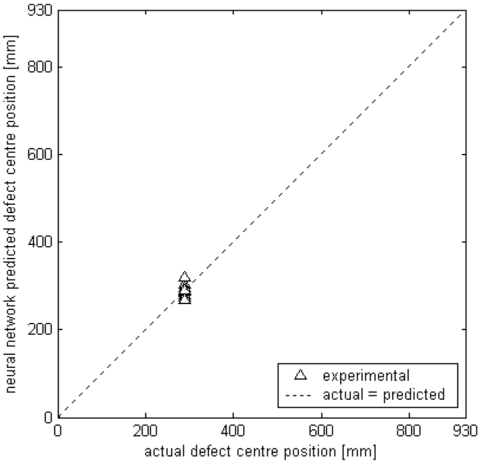

Fig. 5.14. Results of neural network for experimental shell mode shapes

Table 5.7

Neurally predicted versus recognized by wavelet analysis defect locations (input: wavelet coefficients based on shell experimental mode shapes)

Input patterns	Wavelet	Scale	Crack centre position [mm]			Error [%]	
			Actual	Recognized by CWT	Predicted by ANN	Actual vs. recognized	Actual vs. predicted
mode 1	gaus4	s = 10	287.5	–	294.1025	–	2.2965
mode 1	gaus6	s = 10	287.5	–	267.5937	–	6.9239
mode 1	gaus8	s = 10	287.5	–	266.9376	–	7.1521
mode 1	gaus10	s = 10	287.5	–	290.9465	–	1.1988
mode 2	gaus4	s = 10	287.5	–	285.8929	–	0.5590
mode 2	gaus6	s = 10	287.5	–	304.0174	–	5.7452
mode 2	gaus8	s = 10	287.5	–	318.3104	–	10.7167
mode 2	gaus10	s = 10	287.5	–	274.8085	–	4.4144
mode 3	gaus4	s = 10	287.5	299	296.0042	4.0000	2.9580
mode 3	gaus6	s = 10	287.5	298	288.7069	3.6522	0.4198
mode 3	gaus8	s = 10	287.5	297	277.9715	3.3043	3.3143
mode 3	gaus10	s = 10	287.5	297	294.6001	3.3043	2.4696

5.5. Summary and conclusions

In this chapter application of the artificial neural network to support the wavelet damage detection has been presented. The simple, backpropagation neural network was trained on the static deflection lines of the cantilever beam. Although, the network has been taught on the static data, it can effectively localize the damage of the same type in the more complex structures, like plate or shell.

The artificial neural network solutions belong to the class of so-called soft computing and the ANN can predict defect only with a certain probability. Hence, the application of the ANN provides sometimes worse identification of defect positions than identification of defect localizations by CWT. Nevertheless, the ANN predictions are relatively good in the cases when it is impossible to locate the defect by analysis of the wavelet transforms of the acceleration records.

Chapter 6

FINAL REMARKS

6.1. General remarks

The presented work is devoted to the wavelet-based techniques in detection and localization of damage. The one-dimensional wavelet analysis has been extended for application in two-dimensional structures. The study on the wavelet analysis applied in damage detection leads to the following conclusions and suggestions:

1. The continuous wavelet transforms (CWT) are more suitable for damage detection than the discrete wavelet transforms (DWT). The CWTs provide good resolution necessary for damage localization.
2. The border distortion problem must be addressed. At least the first and second derivative of the extrapolation, outside the geometric boundary conditions, must be continuous.
3. The symmetric wavelets provide better transforms for damage localization. Gaussian wavelet and Reverse Biorthogonal wavelet are found to be the most appropriate for the considered experimental and numerical examples.
4. The number of vanishing moments of the applied wavelet must be at least two. However, it has been shown that better resolution of the transformed response is obtained with wavelets having four and more vanishing moments.
5. The considered wavelet transforms act as differential operators providing the information on signal derivatives. The order of the derivative is equal to the number of the vanishing moments.
6. The two-dimensional wavelet transform has been adopted and applied for the 2D structure responses. The new indices for 2D damage detection, namely the modulus and the angle of the gradient vector of the vertical and horizontal wavelet transform components, have been introduced.

The experimental study on the beam, plate and shell structures has been conducted by the proposed photogrammetic method and the dynamic impulse tests. The conducted work allows to draw the following remarks:

1. The photogrammetric method for the evaluation of the deflection line is found to be simple and non-contact technique that provides quick measurements in large number of spatially distributed points.
2. The accuracy of the photogrammetric method strongly depends on the availably of the picture resolution, i.e., on the quality of the camera.
3. The application of the proposed method for 2D or 3D structures like plates and shells is limited.
4. The mode shapes extraction by the modal hammer impact and acceleration measurements is found to be a well suited method for the considered structures.
5. The mode shapes reconstruction should be conducted through the frequency response function estimator $H_2(\omega)$ that helps to solve the signal noise contamination problem.

6. The use of the impact mode shapes estimation for wavelet damage detection requires application of the impact force in a large number of spatially distributed points.

The analysis of the wavelet response transforms is conducted by a well known pick-picking method. The position of the largest value of the wavelet coefficient indicates damage location. The analysis of the wavelet transforms based on the numerically determined structural responses leads to the conclusion that the method is a perfect tool for damage detection. However, the application of the experimental data allows detection of only relatively large cracks. The successful detection of the beam crack location was obtained for the crack of depth 35% of the beam height. In the plate structure, the damage detection was possible for defect of the area of 2.4% of the total area and depth of 25%. In the considered shell the detection was possible for the flaw amounted to about 0.2% of the surface area and the depth of 30%. Nevertheless, the extracted mode shapes proved to be sensitive to damage and can be considered as input for damage detection technique.

The improvement of the damage localization from the wavelet coefficients can be obtained by application of the artificial neural network (ANN) system. The simple backpropagation ANN systems applied for the considered experimental structures showed that the location of the damage is possible even in the cases were the pick-picking method was not applicable.

Advantage of the proposed wavelet damage detection technique is the effective identification of defect position without knowledge of neither characteristics of structure nor its mathematical model. The method can be successfully used even in the case few isolated defects. However, the wavelet method has some disadvantages. The wavelet transform detects the signal singularities but does not indicate the source of the singularities. The flaw, the additional mass, the concentrated force, the discontinuity of the cross-section, the step change in stiffness result in the same peak in the wavelet transform modulus. Additional problem is connected with the defects situated near the supports due to border distortions contamination. The wavelet transform cannot be used to defect detection in the frame corners or in the places of discontinuity of the cross-section or connections of the two elements.

Further study should be conducted towards improvement of the ANN system or design neuro-fuzzy systems that can greatly enhance the precision of the wavelet damage detection method. However, the main challenge is to derive the system for the real structure that can handle all the complication included in the dynamics of the existing complex engineering objects. The problems related to high quality measurements, management of large number of data, extraction of the most important information and precise description of the structure integrity have to be solved.

6.2. Original elements of the study

In the authors' opinion, the following items can be considered as original elements of the presented work:

1. Application of the two-dimensional wavelet analysis to damage localization (until now, only the one-dimensional wavelet analysis has been applied) and proposition of the use of the modulus and angle of the wavelet transform as indicators of damage localization.

2. Development of the photogrammetric technique for quick and simple static deflection lines determination as the combination the digital images and signal processing.
3. Novel experimental verification of use of the wavelet transform on the beam, plate and shell structures. Experimental verification on the plate and shell structures has not been presented in the literature yet.
4. Verification in the numerical simulations of the all types of the wavelet functions and indication of the symmetrical wavelet with minimum 4 vanishing moments as the best wavelet to damage localization.
5. Suggestion of the Gaussian wavelet and Reverse Biorthogonal wavelet as the best candidates to damage detection technique in the performed experimental works.

ACKNOWLEDGEMENTS

The authors are thankful to Prof. P. Kłosowski and Prof. Z. Zembaty for very thorough reviews of the manuscript and the numerous suggestions that have substantially improved our work.

The support of colleagues form the Department of Civil and Environmental Engineering, Gdansk University of Technology, is greatly acknowledged. Especially, we are grateful to our colleagues from DIM (Diagnostic, Identification and Monitoring) group for mutual meetings, cooperation on dynamic studies, many precious discussions and fruitful exchange of ideas. We are also indebted to Mr. W. Motek and Mr. B. Kawulak (former master students of Department of Structural Mechanics, Gdansk University of Technology) for their help in conducting the experimental dynamic tests on cylindrical shell.

The authors are grateful to the support of the Polish Ministry of Science and Higher Education via Grant no. N506 065 31/3149 entitled: ‘‘Multilevel damage detection system in engineering structures’’.

M. Rucka would also thank the Foundation for Polish Science for being granted the Scholarschip for Young Scientists in the year 2007.

REFERENCES

[1] Abdelghani M., Goursat M., Biolchini T.: On-line modal monitoring of aircraft structures under unknown excitation. *Mechanical Systems and Signal Processing* 13(6), 1999, 839–532.

[2] Abdo M. A.-B., Hori M.: A numerical study of structural damage detection using changes in the rotation of mode shapes. *Journal of Sound and Vibration* 251(2), 2002, 227–239.

[3] Aktan A. E., Catbas F. N., Pervizpour M., Kulcu E., Grimmelsman K., Barrish R., Qin X.: Real-time bridge health monitoring for management. *The Second Workshop on Advanced Technologies in Urban Earthquake Disaster Mitigation*, Kyoto University, Japan 2000.

[4] Barai S. V., Pandey P. C.: Time-delay neural networks in damage detection of railway bridges. *Advanced in Engineering Software*; 28(1), 1997, 1–10.

[5] Basu B., Gupta V. K.: Stochastic seismic response of single-degree-of-freedom systems through wavelets. *Engineering Structures* 22(12), 2000, 1714–1722.

[6] Białasiewicz J. T.: *Falki i aproksymacje*. Warszawa: Wydawnictwa Naukowo-Techniczne 2000.

[7] Bień J., Rawa P.: Laserowe pomiary statycznych i dynamicznych przemieszczeń dużych konstrukcji mostowych. *Inżynieria i Budownictwo* 3–4, 2002, 161–165.

[8] Boggess A., Narcowich F. J.: *A First Course in Wavelets with Fourier Analysis*. Beijing: Publishing House of Electronics Industry 2002.

[9] Bow S.-T.: *Pattern Recognition and Image Preprocessing*. New York: Marcel Dekker Inc. 2002.

[10] Brownjohn J. M. W., Dumanoglu A. A., Severn R. T., Blakeborough A. B.: Ambient vibration survey of the Bosporus Suspension Bridge. *Earthquake Engineering and Structural Dynamics* 18(2), 1989, 263–283.

[11] Brownjohn J. M. W., Dumanoglu A. A., Severn R. T., Taylor C. A.: Ambient vibration measurements of the Humber Suspension Bridge and comparison with calculated characteristics. *Proceedings Institution of Civil Engineers* Part 2, 83, 1987, 561–600.

[12] Cabell R. H., Fuller C. R., O'Brien W. F.: Neural network modeling of oscillatory loads and fatigue damage estimation of helicopter components. *Journal of Sounds and Vibration* 209(2), 1998, 329–342.

[13] Cawley P., Adams R. D.: The location of defects in structures from measurements natural frequencies. *Journal of Strain Analysis* 14(2), 1979, 49–57.

[14] Chan Y. T.: *Wavelet basics*. Boston, Dordrecht, London: Kluwer Academic Publishers 1995

[15] Chang C.-C., Chen L.-W.: Vibration damage detection of a Timoshenko beam by spatial wavelet based approach. *Applied Acoustics* 64(12), 2003, 1217–1240.

[16] Chang C.-C., Chen L.-W.: Damage detection of a rectangular plate by spatial wavelet based approach. *Applied Acoustic* 65(12), 2004, 819–832.

[17] Chmielewski T., Zembaty Z.: *Podstawy dynamiki budowli*. Warszawa: Arkady 1998.

[18] Chopra A. K.: *Dynamics of structures*. Upper Saddle River, New Jersey: Prentice Hall 2001.

[19] Clough R. W., Penzien J.: *Dynamics of structures*. McGraw-Hill Inc. 1993.

[20] Daubechies I.: *Ten lectures on wavelet*. Philadelphia: Society for Industrial and Applied Mathematics 1992.

[21] Demuth H., Beale M.: *Neural networks toolbox*. The MathWorks Inc. 2002.

[22] Dimarogonas A. D.: Vibration of cracked structures: a state of the art review. *Engineering Fracture Mechanics* 55(5), 1996, 831–857.

[23] Doebling S. W., Farrar C. R., Prime M. B.: A summary review of vibration-based damage identification methods. *Shock and Vibration Digest* 30(2), 1998, 91–105.

[24] Douka E., Loutridis S., Trochidis A.: Crack identification in beams using wavelet analysis. *International Journal of Solid and Structures* 40(13–14), 2003, 3557–3569.

[25] Douka E., Loutridis S., Trochidis A.: Crack identification in plates using wavelet analysis. *Journal of Sound and Vibration* 270(1–2), 2004, 279–295.

[26] Farrar C. R., Doebling S. W.: *Damage detection II: Field Applications to Large Structures, in Modal Analysis and Testing.* Dordrecht, Netherlands: J. M. M. Silva and N. M. M. Maia, edts., Nato Science Series, Kluwer Academic Publishers. 1999.

[27] Freeman J. A.: *Simulating neural networks with Mathematica.* Addison-Wesley Publishing Company Inc. 1994.

[28] Fritzen C. P. Vibration-based structural health monitoring – concepts and applications. *Key Engineering Materials* 293–294, 2005, 3–18.

[29] Garg A. K., Roy Mahapatra D., Suresh S., Gopalakrishnan S., Omkar S. N.: Estimation of composite damage model parameters using spectral finite element and neural network. *Composites Science and Technology* 64(12), 2004, 2477–2493.

[30] *GENF. Generation of Finite Elements and Beam Structures,* SOFiSTiK AG, Oberschleissheim 2001.

[31] Gentile A., Messina A.: On the continuous wavelet transforms applied to discrete vibrational data for detecting open cracks in damaged beams. *International Journal of Solid and Structures* 40(2), 2003, 295–315.

[32] Ghoshal A., Sundaresan M. J., Schulz M. J., Pai P. F.: Structural health monitoring techniques for wind turbine blades. *Journal of Wind Engineering and Industrial Aerodynamics* 85(3), 2000, 309–324.

[33] Glabisz W.: *Pakietowa analiza falkowa w zagadnieniach mechaniki.* Wrocław: Oficyna Wydawnicza Politechniki Wrocławskiej 2004.

[34] Grondel S., Assaad J., Delebarre C., Moulin E.: Health monitoring of a composite wingbox structure. *Ultrasonics* 42(1-9), 2004, 819–824.

[35] Gros X. E.: An eddy current approach to the detection of damage caused by low-energy impacts on carbon fibre reinforced materials. *Materials & Design* 16(3), 1995, 167–173.

[36] Gurley K., Kareem A.: Application of wavelet transforms in earthquake, wind and ocean engineering. *Engineering Structures* 21(2), 1999, 149–167.

[37] Higuchi S., Makihara Z., Nonaka Y., Ooka N.: Development of flow sizing technique by radiographic testing-application of the “GUCHI” technique. *Key Engineering Materials* 270–273, 2004, 1316–1323.

[38] Hoła J., Schabowicz K. New technique of nondestructive assessment of concrete strength using artificial intelligence. *NDT&E International* 38(4), 2005, 251–259.

[39] Hong J.-C., Kim Y. Y., Lee H. C., Lee Y. W.: Damage detection using Lipschitz exponent estimated by the wavelet transform: applications to vibration modes of a beam. *International Journal of Solid and Structures* 39(7), 2002, 1803–1846.

[40] Hou Z., Noori M., Amand R. S.: Wavelet-based approach for structural damage detection. *Journal of Engineering Mechanics* 126(7), 2000, 677–683.

[41] Hu Y. H., Hwang J.-N.: *Handbook of neural networks signal processing.* CRC Press LLC 2002.

[42] *Image Processing Toolbox.* The MathWorks Inc. 2000.

[43] Kaiser G.: *A Friendly Guide to Wavelets.* Boston, Basel, Berlin: Birkhauser 1994.

[44] Kao C. Y., Hung S.-L.: Detection of structural damage via free vibration responses generated by approximating artificial neural networks. *Computer & Structures* 81(28–29), 2003, 2631–2644.

[45] Khiem N. T., Lien T. V.: Multi-crack detection for beam by the natural frequencies. *Journal of Sound and Vibration* 273(1–2), 2004, 175–184.

[46] Kim J. T., Stabbs N.: Improved damage identification method based on modal information. *Journal of Sound and Vibration* 252(2), 2002, 223–238.

[47] Kim H., Melhem H.: Damage detection of structures by wavelet analysis. *Engineering Structures* 26(3), 2004, 347–362.

[48] Kim J.-T., Ryu Y.-S., Cho H.-M., Stubbs N.: Damage identification in beam-type structures: frequency-based method vs mode-shape-based method. *Engineering Structures* 25(1), 2003, 57–67.

[49] Kim. H. O., Kim R. Y.: Characterization of biorthogonal wavelets which are associated with biorthogonal multiresolution analysis. *Applied and Computational Harmonic Analysis* 11(2), 2001, 263–272.

[50] Krawczuk M., Palacz M., Ostachowicz W.: Wave propagation in plate structures for crack detection. *Finite Elements in Analysis and Design* 40(9–10), 2004, 991–1004.

[51] Kucharski T.: *Systemy pomiarów drgań mechanicznych*. Warszawa: Wydawnictwa Naukowo-Techniczne 2002.

[52] Kuźniar K., Waszczyszyn Z.: Neural analysis of vibration problems of real flat buildings and data pre-processing. *Engineering Structures* 24(10), 2002, 1327–1335.

[53] Lardies J., Gouttebroze S.: Identificatin of modal parameters using the wavelet transform. *International Journal of Mechanical Sciences* 44(11), 2002, 2263–2283.

[54] Lee J., Seo D.-W., Shoji T.: Numerical consideration of magnetic camera for quantitative non-destructive evaluation. *Key Engineering Materials* 270–273, 2004, 630–635.

[55] Lee Y.-S., Chung M.-J.: A study on crack detection using frequency test data. *Computer & Structures* 77(3), 2000, 327–342.

[56] Li H.-N., Li D.-S., Song G.-B.: Recent application of fiber optic sensors to health monitoring in civil engineering. *Engineering Structures* 26(11), 2004, 1647-1657.

[57] Li Z. X., Chan T. H. T., Ko J. M.: Fatigue analysis and life prediction of bridges with structural health monitoring data – Part I: methodology and strategy. *International Journal of Fatigue* 23(1), 2001, 45–53.

[58] Li Z. X., Chan T. H. T., Ko J. M.: Fatigue analysis and life prediction of bridges with structural health monitoring data – Part II: application. *International Journal of Fatigue* 23(1), 2001, 55–64.

[59] Liu S.W., Huang J.H., Lee C. C.: Detection of cracks using neural networks and computational mechanics. *Computer methods in applied mechanics and engineering* 191(25-26), 2002, 2831–2845.

[60] Long R., Chen D.: Biorthogonal wavelet bases on R^d. *Applied and Computational Harmonic Analysis* 2(3), 1995, 230–242.

[61] Loutridis S., Douka E., Trochidis A.: Crack identification in double-cracked beams using wavelet analysis. *Journal of Sound and Vibration* 277(4–5), 2004, 1025–1039.

[62] Maia N. M. M, Silva J. M. M. 1997. *Theoretical and experimental modal analysis*. Baldock, Hertfordshire: Research Studies Press Ltd. 1997.

[63] Mallat S.: *A wavelet tour of signal processing*, Academic Press 1998.

[64] Mallat S., Hwang W. L.: Singularity detection and processing with wavelets. *IEEE Transaction on Information Theory* 38(2), 1992, 617–643.

[65] Mallat S., Zhong S.: Characterization of signals from multiscale edges. *IEEE Transaction on Pattern Analysis and Machine Intelligence* 14(7), 1992, 710–732.

[66] Mallat S.: A theory for multiresolution signal decomposition: the wavelet representation. *IEEE Transaction on Pattern Analysis and Machine Intelligence* 11(7), 1989, 674–693.

[67] McConnell K. G.: *Vibration Testing: Theory and Practice*. New York: John Wiley & Sons, Inc. 1995.

[68] Melhem H., Kim H.: Damage detection in concrete by Fourier and wavelet analyses, *Journal of Engineering Mechanics* 129(5), 2003, 571–577.

[69] Messina A.: Detecting damage in beams through digital differentiator filters and continuous wavelet transforms. *Journal of Sound and Vibration* 272(1–2), 2004, 385–412.

[70] Meyer Y.: *Wavelets. Algorithms and Applications*. Philadelphia: Society for Industrial and Applied Mathematics 1993.

[71] Mickens T., Schulz M., Sundaresan M., Ghoshal A., Naser A.S., Reichmeider R.: Structural health monitoring of an aircraft joint. *Mechanical Systems and Signal Processing* 17(2), 2003, 285–303.

[72] Misiti M., Misiti Y., Oppenheim G., Poggi J.-M.: *Wavelet toolbox*. The MathWorks Inc 2000.

[73] Moller M. F.: A scaled conjugated gradient algorithm for fast supervised learning. *Neural Networks* 6(4), 1993, 525–533.

[74] Nassif H. H., Gindy M., Davis J.: Comparison of laser Doppler vibrometer with contact sensors for monitoring bridge deflection and vibration. *NDT&E International* 38(3), 2005, 213–218.

[75] Nichols J. M.: Structural health monitoring of offshore structures using ambient vibrations. *Applied Ocean Research* 25(3), 2003, 101–114.

[76] Niedostatkiewicz M., Rucka M., Wilde K.: Application of time-frequency methods for analysis of dynamic silo flow. *The 8th Conference Shell Structures Theory and Applications*, Gdansk - Jurata, Poland: 2005, 393–397.

[77] Ohtsu M.: Acoustic emission for structural integrity of concrete from fresh to damaged. *Key Engineering Materials* 270–273, 2004, 543–548.

[78] Okafor A. C., Dutta A.: Optimal ultrasonic pulse repetition rate for damage detection in plates using neural networks. *NDT&E International* 34(7), 2001, 469–481.

[79] Omenzetter P., Brownjohn J. M. W., Moyo P.: Identification of unusual events in multichannel bridge monitoring data. *Mechanical Systems and Signal Processing* 18(2), 2004, 409–430.

[80] Ovanesova A. V., Suárez L. E.: Application of wavelet transform to damage detection in frame structures. *Engineering Structures* 26(1), 2004, 39–49.

[81] Pai P. F., Young L. G.: Damage detection of beams using operational deflection shapes. *International Journal of Solid and Structures* 38(18), 2001, 3161–3192.

[82] Palacz M., Krawczuk M.: Analysis of longitudinal wave propagation in cracked rod by the spectral element method. *Computer & Structures* 80(24), 2002, 1809–1816.

[83] Pandey A. K., Biwas M., Samman M. M.: Damage detection from changes in curvature mode shapes. *Journal of Sound and Vibration* 145(2), 1991, 321–332.

[84] Patil D. P., Maiti S. K.: Detection of multiple cracks using frequency measurements. *Engineering Fracture Mechanics* 70(12), 2003, 1553–1572.

[85] Patjawit A., Kanok-Nukulchai W.: Health monitoring of highway bridges based on a Global Flexibility Index. *Engineering Structures* 27(9), 2005, 1385–1391.

[86] Peng Z. K., Chu F. L.: Application of the wavelet transform in machine condition monitoring and fault diagnostics: a review with bibliography. *Mechanical Systems and Signal Processing* 18(2), 2004, 199–221.

[87] Quek S.-T., Wang Q., Zhang L., Ang K.-K.: Sensitivity analysis of crack detection in beams by wavelet technique. *International Journal of Mechanical Sciences* 43(12), 2001, 2899–2910.

[88] Ranjith P, Baby P. C, Joseph P.: ECG analysis using wavelet transform: application to myocardial ischemia detection. *ITMB-RBM* 24(1), 2003, 44–47.

[89] Ren W.-X., Roeck G. D.: Structural damage identification using modal data. I: Simulation verification. *Journal of Structural Engineering* 128(1), 2002, 87–95.

[90] Ren W.-X., Roeck G. D.: Structural damage identification using modal data. II: Test verification. *Journal of Structural Engineering* 128(1), 2002, 96-104.

[91] Rogers L. M.: Crack detection using acoustic emission methods - fundamentals and applications. *Key Engineering Materials* 293-294, 2005, 33–48.

[92] Rose J. L.: Ultrasonic guided waves in structural health monitoring. *Key Engineering Materials* 270-273, 2004, 14–21.

[93] Rucka M., Wilde K.: Numerical simulation of damage detection in rectangular plate by two-dimensional wavelet transform. *International Workshop on simulations in urban engineering*, Gdańsk, Poland 2004, 205–208.

[94] Rucka M., Wilde K.: On using digital photos in a structure rehabilitation. *International Workshop on rehabilitation of existing urban building stock*, Gdańsk, Poland 2004, 109–112.

[95] Rucka M., Wilde K.: Damage location in beam and plate structures by wavelet analysis of experimentally determined mode shapes. *Key Engineering Materials* 293–294, 2005, 313–320.

[96] Rucka M., Wilde K.: Lokalizacja uszkodzeń konstrukcji belkowych za pomocą badań dynamicznych i analizy falkowej. *Inżynieria i Budownictwo* 6, 2005, 333–335.

[97] Rucka M., Wilde K.: Application of continuous wavelet transform in vibration based damage detection method for beam and plates. *Journal of Sound and Vibration* 297, 2006, 536–550.

[98] Rucka M., Wilde K.: Crack identification using wavelets on experimental static deflection profiles. *Engineering Structures* 28(2), 2006, 279–288.

[99] Rytter A.: Vibration based inspection of civil engineering structures. PhD dissertation, Department of Building Technology and Structural Engineering, Aalborg University, Aalborg, Dennmark 1993.

[100] Sahin M., Shenoi R. A.: Quantification and localization of damage in beam-like structures by using artificial neural networks with experimental validation. *Engineering Structures* 25(14), 2003, 1785–1802.

[101] Salawu O. S.: Detection of structural damage through changes in frequency: a review. *Engineering Structures*. 19(9), 1997, 718–723.

[102] Schmeelk J.: Wavelet transform of two-dimensional images. *Mathematical and Computer Modelling* 36(7-8), 2002, 939–948.

[103] Shinoda K., Morotomi R., Mukai K., Yoshiara T., Shirai M., Miyamoto H.: Application of digital radiography to aerospace-craft. *Key Engineering Materials* 270–273, 2004, 1361–1365.

[104] Sivannarayana N., Reddy D. C.: Biorthogonal wavelet transforms for ECG parameters estimation. *Medical Engineering & Physics* 21(3), 1999, 167–174.

[105] Slavič J., Simonovski I., Boltežar M.: Damping identification using a continuous wavelet transform: application to real data*. Journal of Sound and Vibration* 262(2), 2003, 291-307.

[106] Staszewski W. J.: Ultrasonic/guided waves for Structural Health Monitoring. *Key Engineering Materials* 293–294, 2005, 49–62.

[107] Strang G, Nguyen T.: *Wavelets and Filter Banks.* Wellesley: Wellesley-Cambridge Press 1996.

[108] Struzik R. S.: Wavelet methods in (financial) time-series processing. *Physica A* 296(1–2), 2001, 307–319.

[109] Struzik R. S., Siebies A. P. J. M.: Wavelet transform based multifractal formalism in outlier detection and localization for financial time series. *Physica A* 309(3–4), 2002, 388–402.

[110] Sumitro S., Matsui Y., Kono M., Okamoto T., Fujii K.: Long span bridge health monitoring system in Japan. *Health Monitoring and Management Systems, Proceedings of SPIE* 4337, 2001, 517–524.

[111] Sun Z., Chang C. C., Asce M. : Structural damage assessment based on wavelet packet transform. *Journal of Engineering Mechanics* 128(10), 2002, 1354–1361.

[112] Thursby G., Sorazu B., Betz D., Staszewski W. Culshaw B.: The use of fibre optic sensors for damage detection and location in structural materials. *Applied Mechanics and Materials* 1–2, 2004, 191–196.

[113] Trifunac M. D., Ivanović S. S., Todorovska M. I.: Wave propagation in a seven-story reinforced concrete building: III. Damage detection via changes in wavenumbers. *Soil Dynamics and Earthquake Engineering* 23(1), 2003, 65–75.

[114] Wang W. J., McFadden P. D.: Application of wavelets to gearbox vibration signals for fault detection. *Journal of Sound and Vibration* 192(5), 1996, 927–939.

[115] Wang Q., Deng X. Damage detection with spatial wavelets. *International Journal of Solid and Structures* 36(23), 1999, 3443–3468.

[116] Waszczyszyn Z., Ziemiański L.: Neural networks in mechanics of structures and materials – new results and prospects of application. *Computer & Structures* 79(22–25), 2001, 2261–2276.

[117] Wieser A., Brunner F. K.: Analysis of bridge deformation using continuous GPS measurements. *INGEO2002, 2nd Conference of Engineering Surveying.* Bratislava, 2002, 45–52.

[118] Wilde K., Rucka M.: Damage detection in rectangular plates by continuous two-dimensional wavelet transform. *Eurodyn Conference.* Paris, France, 2005, 1935–1940.

[119] Wojtaszczyk P.: *Teoria falek.* Warszawa: Wydawnictwo Naukowe PWN 2000.

[120] Xiaochun S., Xinjun W., Yihua K.: The method and apparatus of magnetic nondestructive testing for boiler waterwall tube. *Key Engineering Materials* 270–273, 2004, 642–646.

[121] Yam L. H., Yan Y. J., Jiang J. S.: Vibration-based damage detection for composite structures using wavelet transform and neural identification. *Composite Structures* 60(4), 2003, 403–412.

[122] Yeung W. T., Smith J. W.: Damage detection in bridges using neural networks for pattern recognition of vibration signatures. *Engineering Structures* 27(5), 2005, 685–698.

[123] Yuen M. M. F.: A numerical study of the eigenparameters of damaged cantilever. *Journal of Sound and Vibration* 103(3), 1985, 301–310.

[124] Yun C.-B., Yi J.-H., Bahng E. Y.: Joints damage of framed structures using a neural networks technique. *Engineering Structures* 23(5), 2001, 425–435.

[125] Zacharias J., Hartmann C., Delgado A.: Damage detection on crates of beverages by artificial neural networks trained with finite-element data. *Computer methods in applied mechanics and engineering* 193(6–8), 2004, 561–574.

[126] Zapico J. L., González M. P., Worden K.: Damage assessment using neural networks. *Mechanical Systems and Signal Processing* 17(1), 2003, 119–125.

[127] Zembaty Z., Kowalski M.: Modal analysis of reinforced concrete frame in various states of damage. *Key Engineering Materials* 293–294, 2005, 735–742.

[128] Zhang G., Hu H., Ta D.: Ultrasonic detection of the metallurgical defects in the steel and its evaluation by neural networks based on the wavelet transform noise suppression. *Key Engineering Materials* 270–273, 2004, 160–167.

[129] Zubaydi A., Haddara M. R., Swamidas A. S. J.: Damage identification in a ship's structure using neural networks. *Ocean Engineering* 29(10), 2002, 1187–1200.

APPLICATION OF WAVELET ANALYSIS IN DAMAGE DETECTION AND LOCALIZATION

In recent years, structural damage detection and health monitoring have been subjects of intensive investigation due to their practical importance. For important engineering structures the early detection of damage is essential since propagation of defects might lead to a catastrophic failure. A relatively recent area of research in damage identification is based on the wavelet analysis. This technique can be performed on mode shapes or static deflections of structure elements. An important feature of the wavelet transform is the ability to characterize the local irregularity introduced by damage into the displacement shape and to react to subtle changes of the structure response.

The aim of the research is to verify the applicability of the wavelet transform in damage localization in engineering structures.

The efficiency of the applied wavelets is verified by experimentally and analytically determined data. Beam, plate and shell structures are tested experimentally and compared with numerical solutions. The measurement of the beam displacements in a large number of spatially distributed points is obtained by the photogrammetric measurement technique, whereas the measurements of the beam, plate and shell mode shapes are obtained by the impulse dynamic testing.

The locations of defects indicated by a peak in the spatial variation of the transformed response are successfully determined. The application of artificial neural networks enables prediction of the crack locations even if the analyzed data are noisy and illegible.

The main advantage of the proposed damage detection technique is the effective identification of the defect position without knowledge of neither characteristics of structure nor its mathematical model.

ZASTOSOWANIE ANALIZY FALKOWEJ DO WYKRYWANIA I LOKALIZACJI USZKODZEŃ

Wykrywanie i lokalizacja uszkodzeń w konstrukcjach inżynierskich są przedmiotem intensywnych badań z powodu ich praktycznego znaczenia. Niezwykle istotne jest wczesne wykrycie uszkodzeń w konstrukcjach inżynierskich o szczególnym znaczeniu, ponieważ ich propagacja może doprowadzić do katastrofy budowlanej. Stosunkowo nową dziedziną badań w wykrywaniu zniszczeń jest zastosowanie analizy falkowej. Metoda ta bazuje na postaciach drgań lub na statycznych liniach ugięć. Ważną cechą transformaty falkowej jest zdolność wykrywania nieregularności zawartych w statycznej bądź dynamicznej odpowiedzi konstrukcji spowodowanych uszkodzeniem.

Celem pracy jest weryfikacja możliwości zastosowania analizy falkowej do zagadnień wykrywania i lokalizacji zniszczeń w konstrukcjach inżynierskich.

Efektywność analizy falkowej została sprawdzona na numerycznie i eksperymentalnie wyznaczonych statycznych i dynamicznych odpowiedziach konstrukcji. Przedmiotem badań były modele konstrukcji belkowej, płytowej i powłokowej. Pomiary statycznej linii ugięcia wykonano zaproponowaną metodą optyczną, natomiast postacie drgań pomierzono metodą impulsowego wzbudzania.

Lokalizację defektu wskazuje lokalne maksimum w przestrzennym rozkładzie transformaty odpowiedzi konstrukcji. Poprawę efektywności lokalizacji zniszczeń uzyskano poprzez użycie sztucznej sieci neuronowej. Zastosowana sieć neuronowa poprawnie rozpoznaje miejsce położenia defektów, nawet w przypadkach, gdy określenie położenia uszkodzenia nie było możliwe z obliczonych współczynników falkowych.

Główną zaletą proponowanej metody jest efektywna lokalizacja położenia zniszczenia bez konieczności znajomości charakterystyk konstrukcji czy też jej matematycznego modelu. Niezbędna jest tylko odpowiedź konstrukcji pomierzona w wielu punktach.

WYDAWNICTWO POLITECHNIKI GDAŃSKIEJ

Wydanie I. Ark. wyd. 8,2, ark. druku 7,5, 58/472

Druk: Przedsiębiorstwo Prywatne *WIB* Piotr Winczewski
ul. Sobieskiego 14, 80-216 Gdańsk, tel. 058 341 99 89